The Development of a Hardware-in-the-Loop Platform for the Attitude Determination and Control Testing of a Small Satellite

by

Muhammad Junaid

Thesis presented in partial fulfilment of the requirements for the degree
Master of Engineering
at Stellenbosch University

Faculty of Engineering
Department of Electrical and Electronic Engineering

Supervisor: Prof. W.H. Steyn

December 2015

Stellenbosch University https://scholar.sun.ac.za

DECLARATION

By submitting this thesis electronically, I declare that the entirety of the work contained therein is my own, original work, that I am the sole author thereof (save to the extent explicitly otherwise stated), that reproduction and publication thereof by Stellenbosch University will not infringe any third party rights and that I have not previously in its entirety or in part submitted it for obtaining any qualification.

December 2015

Copyright © 2015 Stellenbosch University

All rights reserved

Stellenbosch University https://scholar.sun.ac.za

Abstract

The launch costs for satellites are extraordinarily high. This emphasizes the importance of thorough unit and subsystem level testing to minimize the risk of failure after launch. The project was aimed at developing a hardware-in-the-loop (HIL) platform capable of testing the attitude determination and control system (ADCS) of small satellites. An Earth observation nanosatellite carrying an imaging payload was considered for testing purposes. The ADCS hardware suite was selected based on the mission requirements for the satellite, after which the necessary electronics for interfacing with the chosen sensors and actuators were designed and developed. The in-orbit performance of the designed ADCS was evaluated using a simulation platform based on realistic ADCS models. Simulation results confirmed that the designed ADCS algorithms met the in-orbit performance requirements using the selected hardware suite.

The HIL platform integrates a fine sun sensor (FSS), a magnetometer, three reaction wheels (RW), three magnetorquers, an inertial measurement unit (IMU), an on-board data handler (OBDH), and a wireless communication module. The test setup consists of an air-bearing table placed inside a Helmholtz cage and a sun simulator. The air-bearing table allows full freedom of rotation in yaw and limited rotation in pitch and roll. The magnetometer was calibrated in the Helmholtz cage using the recursive least squares (RLS) method, as used for in-orbit magnetometer calibration. The magnetic field vector generated by the Helmholtz cage allowed testing of the B-dot and the stable spin magnetic controllers on the HIL platform. The B-dot controller damped the initial body rates to values less than 0.5°/s. A Rate Kalman Filter (RKF) was implemented to estimate the body angular rates from magnetometer measurements. The TRIAD method was used for attitude determination based on the magnetometer and the FSS output vectors. A quaternion feedback RW controller was tested on the HIL platform for yaw pointing. The pointing error observed was within $\pm 0.2°$. In the final stage of HIL testing, the RW controller was combined with the magnetic controllers. The RW controller maintained the reference pointing in yaw and the magnetic controllers maintained the reference angular momentum of the wheel on the air-bearing table.

Stellenbosch University https://scholar.sun.ac.za

Uittreksel

Satelliet lanseringskostes is merkwaardig hoog. Daarom is deeglike eenheids- en substelselvlak toetse noodsaaklik om die risiko van na-lanseringsmislukkings te verminder. In hierdie projek is ‘n hardeware-in-die-lus (HIL) platform vir die toets van ‘n klein satelliet se oriëntasiebepaling- en beheerstelsel (OBBS) ontwikkel. ‘n Aardwaarnemingsnanosatelliet, wat ‘n kamera as loonvrag dra, is vir toetsdoeleindes oorweeg. Die keuse van OBBS hardeware komponente is op die satelliet missie se vereistes gebasseer. Daarna is die elektronika wat nodig is om met die sensore en aktueerders te koppel ontwerp en ontwikkel. Die OBBS se in-wentelbaan vermoëns is d.m.v. simulasies, wat op realistiese OBBS komponentmodelle gebasseer is, geëvalueer. Dié simulasies het bevestig dat die OBBS algoritmes se in-wentelbaan vermoëns die vereistes te verwagte van so ‘n stelsel bevredig.

Die HIL platform bestaan uit ‘n fyn sonsensor (FSS), ‘n magnetometer, drie reaksiewiele (RW), drie magneetstange, ‘n inersieële metingseenheid, ‘n aanboord datahanteerder (ABDH) en ‘n draadlose kommunikasie module. Die toetsomgewing bestaan uit ‘n sonsimuleerder en ‘n luglaer binne in ‘n Helmholtz hok. Volle rotasie om die gier-as word deur die luglaer toegelaat, maar duik- en rol rotasies word beperk. Die magnetometer is d.m.v. ‘n rekursiewe kleinstekwadraat metode, wat ook vir in-wentelbaan kalibrasies gebruik word, in die Helmholtz hok gekalibreer. B-dot en stabiele spin magnetiese beheer kon m.b.v. die Helmholtz hok se opgewekte magneetveld getoets word. Die B-dot beheerder kon die oorspronklike liggaamhoeksnelhede tot minder as 0.5°/s demp. ‘n Hoektempo Kalman Filter (RKF) is geïmplementeer om die liggaam se hoeksnelhede vanaf die magnetometer lesings af te skat. Die TRIAD metode, wat op die magnetometer en FSS uittree vektore gebasseer is, is vir oriëntasiebepaling gebruik. Gier-as rigtinvermoë is in die HIL omgewing getoets met ‘n Quaternioon RW terugvoerbeheerder. Die maksimum rotasiehoekfout het nie 0.2° oorskry nie. In die finale HIL fase is die RW beheerder met die magnetiese beheerders gekombineer. Die RW beheerder het die gier-as oriëntasie onderhou, terwyl die magnetiese beheerders momentumontlading van die wiel uitgevoer het.

Stellenbosch University https://scholar.sun.ac.za

Acknowledgements

First and foremost, I express my gratitude to The Almighty for HIS help and mercy, which made possible for me to accomplish this work. I would like to extend my sincere gratitude to the following persons:

- My supervisor, Professor W.H. Steyn, for his guidance, knowledge sharing and the research opportunities he provided.
- My colleagues in the Electronic Systems Laboratory (ESL), in particular Willem Jordaan, Gerhard H. Janse van Vuuren, Mike-Alec Kearney, Christoffel J. Groenewald, Jako Gerber, Mohammed bin Othman , Nico Rossouw, Nico Calitz and Douw Steyn for their helpful inputs, useful discussions and advices
- All the people involved in manufacturing the project hardware, particularly Mr. Johan Arendse and Mr. Wessel Croukamp for their friendly and skilful assistance
- My parents , for the affection, inspiration and encouragement, I received from them
- My wife, for her love, care, support and faith in me.

Lastly, the financial assistance from Pakistan Space and Upper Atmosphere Research Commission (SUPARCO) is hereby greatly acknowledged. In this regard, I would specifically acknowledge Dr. Muhammad Yasir, for his encouragement and guidance to persuade me for this program.

Stellenbosch University https://scholar.sun.ac.za

Table of Contents

ABSTRACT II

UITTREKSEL III

ACKNOWLEDGEMENTS IV

TABLE OF CONTENTS V

LIST OF FIGURES XI

LIST OF TABLES XV

LIST OF ABBREVIATIONS XVI

1. INTRODUCTION 1

1.1 BACKGROUND 1

1.2 PROBLEM STATEMENT 2

1.2.1 Research Objectives 2

1.2.2 The ADCS Mission Requirements 3

1.3 LITERATURE REVIEW 3

1.3.1 The CubeSat Standard 3

1.3.2 Nanosatellite Industry Trends 4

1.3.3 Nanosatellite Missions 5

1.3.3.1 Generic Nanosatellite Bus 5

1.3.3.2 Flock 1 Imaging Constellation 6

1.3.3.3 PRISM 7

1.3.3.4 QbX Satellites 8

1.3.4 Nanosatellite Test Platforms 9

1.4 THESIS OUTLINE 11

2. THEORETICAL BACKGROUND 12

2.1 ATTITUDE DESCRIPTION 12

2.1.1 Coordinate Frames 12

2.1.1.1 Spacecraft-Centred Coordinates 12

Stellenbosch University https://scholar.sun.ac.za

2.1.1.2 Earth- Centered Coordinates 14
2.1.2 Attitude Representation 14
2.1.2.1 Direction Cosine Matrix 15
2.1.2.2 Euler Angles 15
2.1.2.3 Quaternions 17
2.2 SATELLITE EQUATIONS OF MOTION 18
2.2.1 Dynamics Equations 18
2.2.2 Kinematics Equations 19
2.3 DISTURBANCE TORQUES 20
2.3.1 Gravity Gradient Torque 20
2.3.2 Aerodynamic Torque 21
2.3.3 Magnetic Disturbance Torque 21
2.3.4 Reaction Wheel Imbalance 22
2.4 SUMMARY 23
3. THE ADCS HARDWARE 24
3.1 THE SENSORS 24
3.1.1 Magnetometer 26
3.1.2 FSS and Horizon Sensor Module 26
3.1.3 Star Tracker 27
3.1.4 Rate Sensor 29
3.2 THE ON-BOARD COMPUTER 29
3.3 THE ACTUATORS 30
3.3.1 Actuator Sizing 30
3.3.1.1 RW Sizing 31
3.3.1.2 Magnetorquer Sizing 32
3.4 MAGNETORQUER DESIGN 33
3.4.1 Magnetic Control Electronics Design 34
3.4.1.1 Design Requirements 35

Stellenbosch University https://scholar.sun.ac.za

3.4.1.2 Component Selection 35
3.4.1.3 Circuit Design 35
3.4.1.4 Magnetic Control Board Software 37
3.5 REACTION WHEEL CONTROLLER DESIGN 39
3.5.1 Electronics Design 40
3.5.2 Encoder Noise Suppression 44
3.5.3 RW Speed Controller Design 45
3.5.3.1 Design Requirements 45
3.5.3.2 System Modelling 45
3.5.3.3 State Space System Representations 46
The continuous to discrete domain conversion was done using Matlab c2d command with a sampling time of 0.1 seconds 47
3.5.3.4 State Feedback Integral Control 47
3.5.3.5 Controller Gains for the Desired Closed Loop Performance 49
3.5.4 RW Performance Test Results 49
3.6 SUMMARY 51
4. THE ADCS ALGORITHMS 52
4.1 ATTITUDE DETERMINATION 52
4.1.1 TRIAD Estimator 53
4.1.1.1 TRIAD Implementation 53
4.1.2 Rate Kalman Filter 54
4.1.2.1 RKF System Model 55
4.1.2.2 RKF Measurement Model 55
4.1.2.3 RKF Implementation 57
4.1.3 Extended Kalman Filter 58
4.1.3.1 System Perturbation Model 59
4.1.3.2 Measurement Perturbation Model 60
4.1.3.3 Innovation Computation 61

Stellenbosch University https://scholar.sun.ac.za

4.1.3.4 The EKF Implementation 62
4.2 ATTITUDE CONTROL 64
4.2.1 Magnetic Control 64
4.2.1.1 B-dot Controller 64
4.2.1.2 Y-spin Controller 65
4.2.1.3 Cross Product Controller 65
4.2.2 Wheel Control 67
4.2.2.1 Quaternion Feedback Controller 68
4.3 SUMMARY 69
5. SIMULATIONS FOR IN-ORBIT ADCS PERFORMANCE 70
5.1 SIMULATIONS MODELS 70
5.1.1 Plant 70
5.1.2 Sensors and Estimators 71
5.1.3 Controllers 74
5.2 RATE ESTIMATORS 76
5.2.1 The RKF Performance 76
5.2.2 The EKF Performance 77
5.3 ADCS MODES DEFINITIONS 78
5.3.1 Idle Mode 78
5.3.2 Safe Mode 78
5.3.3 Imaging Mode 79
5.3.4 Nominal Mode 79
5.3.4.1 Momentum Management 79
5.4 SIMULATION PERFORMANCE 79
5.4.1 The B-dot and the Y-Spin Controller Performance 81
5.4.2 The Y-wheel RW Controller with Magnetic Nutation Damping 82
5.4.3 Wheel Pointing during Imaging Mode 84
5.4.4 Sun Tracking during the Nominal Mode 85

Stellenbosch University https://scholar.sun.ac.za

5.4.5 Momentum Unloading Simulations 87
5.5 SUMMARY 88
6. THE ADCS TESTING IN AN HIL ENVIRONMENT 89
6.1 HIL TEST ENVIRONMENT 89
6.1.1 Air-Bearing Table 89
6.1.2 Helmholtz Cage System 91
6.1.3 Sun Simulator 92
6.1.4 Test Computer 92
6.2 HIL HARDWARE CONFIGURATION 93
6.2.1 Sensors Placement 93
6.2.2 Actuators Placement 95
6.2.3 Data Communication 95
6.2.4 Power Interface 97
6.3 MAGNETOMETER CALIBRATION 97
6.4 HIL TEST SCENARIOS 100
6.4.1 HIL Testing of the Magnetic Controllers 100
6.4.2 HIL Testing of the RW Controllers 104
6.4.3 HIL Testing of the Momentum Unloading Controller 107
6.5 SUMMARY 109
7. RESEARCH CONCLUSIONS 110
7.1 CONCLUSIVE RESEARCH SUMMARY 110
7.2 RECOMMENDATIONS 114
7.2.1 ADCS Hardware 114
7.2.2 Redundancy for Reliability 115
7.2.3 Test Facility 115
BIBLIOGRAPHY 116
APPENDIX A. THE EXTENDED KALMAN FILTER DERIVATIONS 123
I- STATE PERTURBATION MATRIX 123

Stellenbosch University https://scholar.sun.ac.za

APPENDIX B. THE MAGNETOMETER CALIBRATIONS 126

I- SCHEME-I 126

II- SCHEME-2 127

APPENDIX C. DATASHEETS 130

I- MAGNETOMETER 130

II- CUBESENSE 133

III- CUBESTAR 135

IV- CUBECOMPUTER 137

V- MICROCONTROLLER 139

VI- BLDC MOTOR DRIVER 141

VII- H-BRIDGE DRIVER FOR MAGNETORQUERS 143

Stellenbosch University https://scholar.sun.ac.za

List of Figures

Figure 1-1: Global nanosatellite launch history (successful launches) [2] 4
Figure 1-2: Exploded view of the BRITE satellite [7] 5
Figure 1-3: Flock 1 [Planet Labs] 6
Figure 1-4: Dove 2 [Planet Labs] 7
Figure 1-5: Overview of PRISM satellite [16] 8
Figure 1-6: Two QbX-1 and QbX-2 [NRL] 8
Figure 1-7: HIL test facility at SDL [22] 10
Figure 1-8: MIT Space Systems Laboratory's Helmholtz Cage [23, 24] 10
Figure 1-9: The Helmholtz Cage at Delft University of Technology [21] 10
Figure 2-1: Inertial Reference Coordinates frame definition 13
Figure 2-2: The Orbit Reference frame definition 13
Figure 2-3: ECI frame axis definitions 14
Figure 2-4: Euler 2-1-3 rotation sequence 16
Figure 2-5: RW static and dynamic imblance 22
Figure 3-1: RM3000 magnetometer components and the evaluation board 26
Figure 3-2: CubeSense integrated FSS and horizon sensor [37] 27
Figure 3-3: CubeStar nano star tracker [38] 27
Figure 3-4: Star tracker placement illustration 28
Figure 3-5: STIM300 inertial measurement unit [39] 29
Figure 3-6: CubeComputer an on-board computer module [40] 30
Figure 3-7: Control logic for single magnetorquer 36
Figure 3-8: Magnetic control board layout 37
Figure 3-9 : Magnetic control software flow chart 39
Figure 3-10: Large reaction wheel from the ESL [42] 40

Stellenbosch University https://scholar.sun.ac.za

Figure 3-11: Reaction wheel drive electronics board layout 42

Figure 3-12: LV8827 BLDC driver architecture [43].....42

Figure 3-13 : Integrated RW electronics board.....44

Figure 3-14: Performances of the noise suppression algorithms 44

Figure 3-15: Plant model for RW system 46

Figure 3-16 : Response to 300 RPM step command.....50

Figure 3-17: Response to 1000 RPM step command.....50

Figure 3-18: Response to a ramp input of slope 10 rpm/second.....50

Figure 3-19: Response to a ramp input of slope 20 rpm/second.....50

Figure 5-1: The ADCS simulation environment as a simple control loop 71

Figure 5-2: The satellite model in Simulink 71

Figure 5-3: The orbit and the environmental block 72

Figure 5-4: The estimation block.....72

Figure 5-5: The Magnetic control Simulink block 75

Figure 5-6:The RW control Simulink block 75

Figure 5-7: The RKF rate estimates during the tumbling state.....77

Figure 5-8: The EKF rate estimates during the tumbling state 78

Figure 5-9: Orbit referenced body rates during the detumbling mode 81

Figure 5-10: Signed on-times of the magnetorquers during the detumbling mode 81

Figure 5-11: The RKF estimation errors during the detumbling mode 82

Figure 5-12: The Y-wheel control with cross-product nutation damping 83

Figure 5-13: The TRIAD attitude estimates 83

Figure 5-14: The EKF performance in controlled state 84

Figure 5-15: 3-axis pointing manoeuvre during the Imaging mode 85

Figure 5-16: Sun Tracking with RW during the Nominal mode 86

Figure 5-17: The Y-component of the FSS measurement vector during sun tracking 86

Stellenbosch University https://scholar.sun.ac.za

Figure 5-18: Mode transition from the Nominal mode to the Imaging mode 87

Figure 5-19: The RW angular momentums during the pointing modes 87

Figure 5-20: Signed on-times of the magnetorquers for momentum unloading operation.....88

Figure 6-1: Air-bearing socket.....90

Figure 6-2:Pressurized Nitrogen supply 90

Figure 6-3: Top view of air-bearing table.....90

Figure 6-4: Bottom view of air-bearing table 90

Figure 6-5: Pendulum motion of air-bearing system 91

Figure 6-6:Helmholtz Cage System [26] 92

Figure 6-7: Ultra bright LED lamp used in Sun Simulator.....92

Figure 6-8: ADCS hardware configuration in HIL-Demonstrator 94

Figure 6-9:Data communication among HIL-Demonstrator units.....96

Figure 6-10: Magnetometer calibration setup.....98

Figure 6-11: RM3000 and the reference magnetometer 98

Figure 6-12:Modelled and the calibrated magnetic fields 99

Figure 6-13: Calibration errors for the RLS method 99

Figure 6-14: Test results for B-dot and Z-spin controllers 102

Figure 6-15: Signed on-times of the magnetorquers for B-dot and Z-spin controllers 102

Figure 6-16: RKF performance during Z-spin.....103

Figure 6-17: HIL test enviroment for RW pointing controllers testing.....104

Figure 6-18: Respose to 30° yaw step 105

Figure 6-19 : Z-axis RW speed during yaw manoeuvre test 106

Figure 6-20: Three axis body rates during yaw manoeuvre test.....106

Figure 6-21: Offset yaw pointing during test-3 108

Figure 6-22: Z-axis RW angular speed during test-3.....108

Figure 6-23: Signed on-times of the magnetorquers of magnetorquers during test-3 108

Stellenbosch University https://scholar.sun.ac.za

Figure A-7-1: RM3000 bias values.....126

Figure A-7-2: After bias compensation 126

Stellenbosch University https://scholar.sun.ac.za

List of Tables

Table 2-1: The worst case disturbance torques 23

Table 3-1: ADCS sensors [32, 34] 25

Table 3-2: Magnetorquer rod design parameters 34

Table 3-3: Magnetorquer coil design parameters 34

Table 3-4 : Logic combinations for magnetic moment control 36

Table 3-5: Power consumption of large CubeWheel module for 8 V 51

Table 5-1: The sensors' parameters used for the simulations 73

Table 5-2: The estimation block modes details 74

Table 5-3: The magnetic control modes 75

Table 5-4: The RW control modes 76

Table 5-5: The ADCS events for the simulations 79

Table 5-6: The magnetorquers on-times for the detumbling controllers 82

Stellenbosch University https://scholar.sun.ac.za

List of Abbreviations

ACS	Attitude Control System
ADCS	Attitude Determination and Control System
BLDC	Brushless Direct Current
BRC	Body Reference Coordinates
CAN	Controller Area Network
CoM	Centre of Mass
CoP	Centre of Pressure
CSS	Coarse Sun Sensor
DCM	Direction Cosine Matrix
EKF	Extended Kalman Filter
EO	Earth Observation
ES	Earth Sensor
ESL	Electronic System Laboratory
FOV	Field of View
FSS	Fine Sun Sensor
GNB	Generic Satellite Bus
HIL	Hardware-in-the-Loop
I^2C	Inter Integrated Circuits
IGRF	International Geomagnetic Reference Field
IMU	Inertial Measuring Unit
IO	Input Output
IRC	Inertial Reference Coordinates
ISR	Interrupt Service Routine

Stellenbosch University https://scholar.sun.ac.za

KF	Kalman Filter
LEO	Low Earth Orbit
LTAN	Local Time of Ascending Node
MCU	Microcontroller Unit
MEMS	Micro Electromechanical Systems
MOI	Moment of Inertia
OBC	On Board Computer
OBDH	On-board data handling system
ORC	Orbit Reference Coordinates
PCB	Printed Circuit Board
POI	Products of Inertia
P-POD	Poly Picosatellite Orbital Deployer
PWM	Pulse Width Modulation
RKF	Rate Kalman Filter
RMS	Root-Mean-Square
RW	Reaction Wheel
SEL	Single Event Latch-up
SEU	Single Event Upset
SGP4	Simplified General Perturbation 4
SPI	Serial peripheral interface
SSO	Sun Synchronous Orbit
SU	Stellenbosch University
TLE	Two-Line Elements
UART	Universal Asynchronous Receiver Transmitter

Stellenbosch University https://scholar.sun.ac.za

1. Introduction

1.1 Background

The capabilities of nanosatellites in spaceborne missions have undergone a tremendous increase in the past decade. Lower manufacturing budgets, ease of adaptability, reduced development times and cost-effective launch configurations have made the nanosatellites a popular platform for academic research, technology evaluation and concept validation. In recent years, nanosatellite missions have not only demonstrated high resolution earth imaging and scientific experimentations, but have also performed astronomical observations.

CubeSat form factor is a prevalent bus structure for nanosatellite missions and a variety of subsystems and units for CubeSats are available off-the-shelf. The Electronic Systems Laboratory (ESL) at Stellenbosch University (SU) possesses research heritage in satellite systems with the development of SUNSAT and the Sumbandila Satellite. Moreover, it has also developed a complete hardware suite for Attitude Determination and Control System (ADCS) for CubeSat standard satellites.

The ADCS is an important subsystem of a satellite platform, which plays a fundamental role in different payload and bus operations of a mission. For instance, it is responsible for keeping the satellite solar panels pointing towards the sun in order to generate electrical power for mission operations. Moreover, it points the satellite payload in the direction required by the mission. Furthermore, it is also responsible to point communication antennae towards the ground station for telemetry, telecommand and payload data communications.

The launch cost of a satellite is extraordinarily high and the remedies for post-launch anomalies are quite limited. This emphasizes the importance of thorough unit and subsystem level testing to minimize the risk of failure after launch. The pre-flight, in-orbit performance of an ADCS is determined by performing comprehensive simulations with realistic system models and the functionality of the system is verified through Hardware-in-the-Loop (HIL) testing.

Stellenbosch University https://scholar.sun.ac.za

1.2 Problem Statement

To develop an ADCS for an earth observation (EO) nanosatellite based on the ADCS hardware developed at the ESL, to determine its in-orbit performance in a simulation environment and to test part of it for functionality in an HIL environment.

1.2.1 Research Objectives

The objectives of this research include the design and development of an ADCS for a nanosatellite. A simulation platform has to be developed to determine the performance of the ADCS in its mission orbit. Secondly, a significant part of the project involves the development of 'ADCS Sensors and Actuators Interface Electronics' compliant to the CubeSat standards. Finally, the functionality of the ADCS algorithms has to be tested with an integrated subset of the ADCS hardware in an HIL environment. The task breakdown and scope of the research is presented here:

1. Design and development of the Magnetic Control Board and the Reaction Wheel (RW) Control Electronics compatible with the CubeSat platform, which include:

    - Survey of power efficient and highly integrated components packages
    - Schematics and PCB design of the modules
    - Design and implementation of RW speed controller
    - Microcontrollers firmware and interface programs for the boards
    - Unit level testing to validate functionality and performance

2. Development of a simulation environment for the ADCS of the mission satellite that contains:

    - Satellite dynamics and kinematics model
    - Sensors and actuators models
    - Attitude determination algorithms implementations
    - Magnetic and RW control implementations

3. HIL testing of an integrated subset of the ADCS hardware to validate the functionality of:

    - The ADCS hardware and the low level software
    - Data communication among the ADCS units
    - Magnetic Controllers and RW Controller
    - RW Momentum Management Controller

Stellenbosch University https://scholar.sun.ac.za

1.2.2 The ADCS Mission Requirements

The nanosatellite considered for the ADCS design and testing is a 12-U CubeSat with following specifications:

- Orbit : 500 km altitude , near circular , sun synchronous
- Satellite Mass: 20 kg
- Dimensions: 0.3m x 0.2m x 0.2m
- Moment of Inertia (MOI): $I_{XX} = 0.33\ kgm^2, I_{YY} = 0.36\ kgm^2, I_{ZZ} = 0.13\ kgm^2$
- Product of Inertia (POI) :$Ixy = 2.3 \times 10^{-3}, Ixz = 3.4 \times 10^{-4}, Iyz = -2.5 \times 10^{-4}$

The in-orbit performance requirements for the ADCS design include:

- ADCS Slew Requirements: 30 deg pitch and roll rotations in 30 seconds
- Pointing Accuracy Requirements: < 0.05° RMS
- Attitude Stability Requirements during imaging: < 0.005°/s RMS

1.3 Literature Review

In this section, CubeSat standards are described briefly and the recent trends in satellite industry are discussed. Moreover, some of the previous nanosatellite missions and their ADCS configurations are also investigated. Lastly, several test facilities for nanosatellite ADCS testing at different laboratories are explored.

1.3.1 The CubeSat Standard

The CubeSat program was started in 1999 as a collaborative effort between Prof. Jordi Puig-Suari at California Polytechnic State University (Cal Poly) and Prof. Bob Twiggs at Space Systems Development Laboratory (SSDL) of Stanford University. The mission objectives for the program were to provide a standard for picosatellites design and to reduce mission cost and development time. Furthermore, the CubeSat program was aimed to provide small payloads an access to space [1] .

The standard single unit (1-U) CubeSat is a 10 cm × 10 cm × 10 cm cube with a mass smaller than 1.33 kg. Cal Poly has devised standards for the CubeSat mechanical and electrical design and has set specific requirements for the operational and testing procedures. This standard also sets the dimensions and mass limits for the larger CubeSat form factors. CubeSats are usually launched as a secondary payload in a piggy back configuration and Cal Poly has also developed a deployment system for the CubeSats named as Poly Picosatellite

Stellenbosch University https://scholar.sun.ac.za

Orbital Deployer (P-POD). The purpose of the P-POD is to ensure the safety of the launch vehicle, the primary payload and the other CubeSats. Moreover, it provides a standard interface to the launch vehicle and thus simplifies the integration requirements. One P-POD can accommodate three single unit CubeSats or one 3-U CubeSat [1]. The P-POD design standards for larger CubeSat form factors are also established by Cal Poly.

1.3.2 Nanosatellite Industry Trends

"The nanosatellite industry has grown considerably with the adoption of the CubeSat standard" [2]. The QB50 program is an international collaborative CubeSat mission that plans to launch 50 CubeSats built by university teams across the globe. The project aims for multi-point in-situ measurements in the lower thermosphere and re-entry research [3]. Similarly, the US National Reconnaissance Office (NRO) has initiated a research program based on the inexpensive satellite platforms (CubeSats) under the name of Colony I & II that plans a launch of 50 triple-unit CubeSats [4].

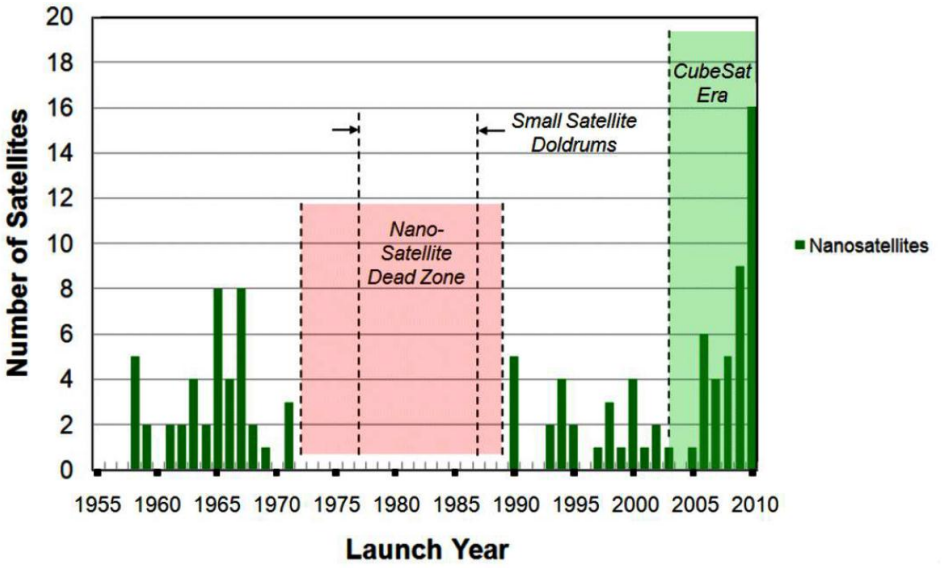

Figure 1-1: Global nanosatellite launch history (successful launches) [2]

Individual units as well as integrated solutions for different subsystems of CubeSat are available off-the-shelf, which has reduced development times for missions. An assessment study by SpaceWorks Commercial® reveals that the global market demand for nano/microsatellites would be 100-142 launches per year in 2020 [2]

Stellenbosch University https://scholar.sun.ac.za

1.3.3 **Nanosatellite Missions**

This section presents a brief overview of some previous nanosatellite missions of interest with regard to their ADCS. These missions include BRITE, CanX-4 & 5 which were based on the Generic Satellite Bus (GNB). Moreover, the ADCS of the 'Flock' imaging constellation, the Japanese imaging nanosatellite 'PRISM' and the QbX satellites are also discussed here.

1.3.3.1 Generic Nanosatellite Bus

The Space Flight Laboratory, at the University of Toronto, conceived a multi-mission bus concept for nanosatellites, named Generic Satellite Bus. The original design of GNB was aimed for BRITE and CanX-4 & 5 missions [5]. However, it had also been utilized for AISSat-1 and AISSat-2 missions. The GNB has a cubic form factor of 20 cm × 20 cm × 20 cm with a mass around 6 kg. Almost 30% of the GNB volume and mass is allocated to mission specific payloads [6]. The ADCS of the GNB contains 3-axis magnetometers, 6 sun sensors (fine & coarse), 3 orthogonal reaction wheels and 3 magnetorquers with an optional interface for 3 rate sensors and a Global Positioning System (GPS) receiver [5].

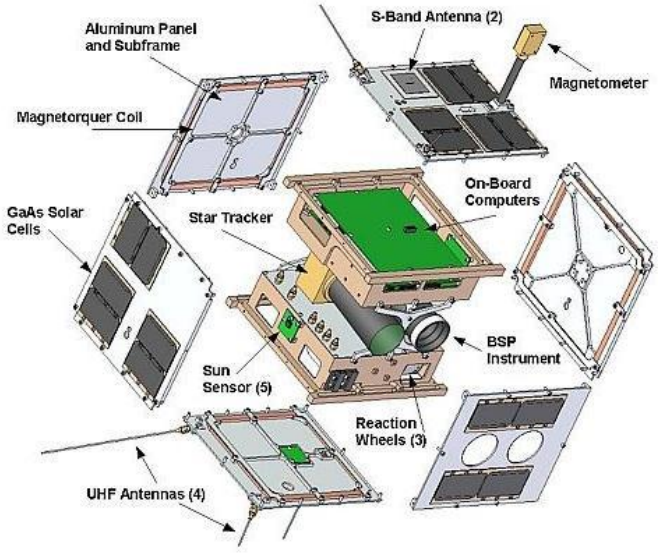

Figure 1-2: Exploded view of the BRITE satellite [7]

BRITE was the first mission based on the GNB design, which was a six satellite constellation to conduct long term stellar observations. In addition to the GNB ADCS, the BRITE satellite platform also carried a nanosatellite star tracker [5]. The Attitude Control System (ACS) modes included detumble mode, coarse pointing mode, fine pointing mode and a Safe-Hold

Stellenbosch University https://scholar.sun.ac.za

mode. The pointing accuracy requirement for the scientific payload instrument was 1° and pointing stability of 1 arc minute was required perpendicular to the star tracker bore sight [8]. Currently, six BRITE nanosatellites including two from Austria, two from Canada and two from Poland are in orbit [9].

The CanX-4 and CanX-5 were GNB based identical satellites designed to perform precise formation flying in Low Earth Orbit (LEO). The mission objectives included sub-centimeter relative position determination, sub-meter relative position control, development and the validation of fuel-efficient formation flying algorithms [5]. With a launch mass of 15 kg each, the satellites were launched as secondary payloads in June, 2014. The satellites demonstrated sub-meter formation control and centimeter-level navigation control for more than 10 orbits for different cases of separation distances, ranging from 1 km to 50 m [10].

1.3.3.2 Flock 1 Imaging Constellation

Flock 1 is the largest constellation of earth imaging satellites that contains numerous triple unit CubeSat nanosatellites, called Doves [11]. Design and developed by Planet Labs, the satellite design utilized commercial off-the-shelf components including the imager. Each unit in the constellation had an approximate mass of 5 kg and had physical dimensions of 10 cm x 10 cm x 34 cm. The first fleet of the Flock 1 constellation was launched as piggy back payload on an Antares-120 vehicle in early 2014 and contained 28 Dove units. The mission orbit was near circular with an altitude of 400 km and a 52° inclination. The image resolution was claimed to be 3-5 meters per pixel [12].

Figure 1-3: Flock 1 [Planet Labs]

Prior to the launch of the Flock 1 fleet, a technology evaluation nanosatellite, Dove 1, was launched in April 2013 as a piggyback payload on the maiden flight of the Antares-110 launch vehicle in a near circular orbit of 280 km [13]. The satellite had an imaging

Stellenbosch University https://scholar.sun.ac.za

payload and a short lifetime of 6 days due to its low orbital altitude. The ADCS of DOVE 1 contained magnetometers, gyros, photo diodes, air-core magnetorquer coils and Reaction Wheels. The B-dot controller was used for attitude stabilization while the reaction wheels were used for fine attitude control. The satellite ADCS switched to nadir pointing mode twice per orbit [14].

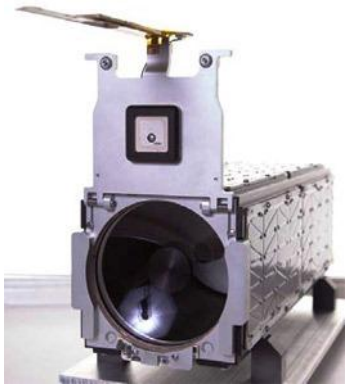

Figure 1-4: Dove 2 [Planet Labs]

The Dove 2 was launched in April 2013 and had a lifespan of approximately 180 days. The ADCS of Dove 2 was based on magnetic control that used a magnetometer, gyro and photo diodes for attitude determination [14]. The Dove 1 and the Dove 2 missions were successful in attitude stabilization, image acquisition and data downloading [13].

1.3.3.3 PRISM

The Pico-satellite for Remote-sensing and Innovative Space Missions (PRISM) was launched on January 23, 2009 in a 596-651 km sun synchronous orbit (SSO). Designed and developed by the University of Tokyo, the satellite mission aimed to acquire images with a ground resolution of 30 meters. The satellite had an extensible boom to extend the focal length of the imager in order to acquire the images [15]. The satellite dimensions in launch configuration were 19.2 cm x 19.2 cm x 40 cm which after the boom deployment became 19.2 cm x 19.2 cm x 60 cm [16].

The extensible boom also provided gravity gradient stabilization to lessen the burden on the ADCS [17]. The satellite bus used 3-axis magnetometers, 3-axis gyro, sun sensors (2 axes x 5 faces = 10 Pcs) as attitude sensors while 3-axis magnetorquers and a single reaction wheel as actuators. Controller Area Networks (CAN) was used as a system communications bus. After calibrating the sensors, the body rates of the satellite were stabilized to 4.5 x 10^{-3} rad/s

Stellenbosch University https://scholar.sun.ac.za

using the cross-product magnetic controller and after the attitude stabilization, 30 m ground resolution images were successfully acquired [16].

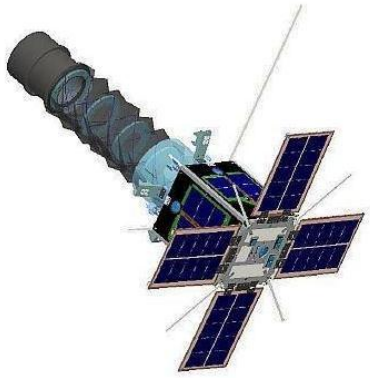

Figure 1-5: Overview of PRISM satellite [16]

1.3.3.4 QbX Satellites

The Naval Research Laboratory (NRL) launched two 3-unit CubeSats in December, 2010 for technology evaluation and experimentation purposes. These satellites were launched in a low altitude orbit of 300 km, and hence had short lifetimes of less than 40 days. The QbX satellites were based on the MISC 2 CubeSat bus by Pumpkin®, with the mass of each satellite approximately 4.5 kg [18].

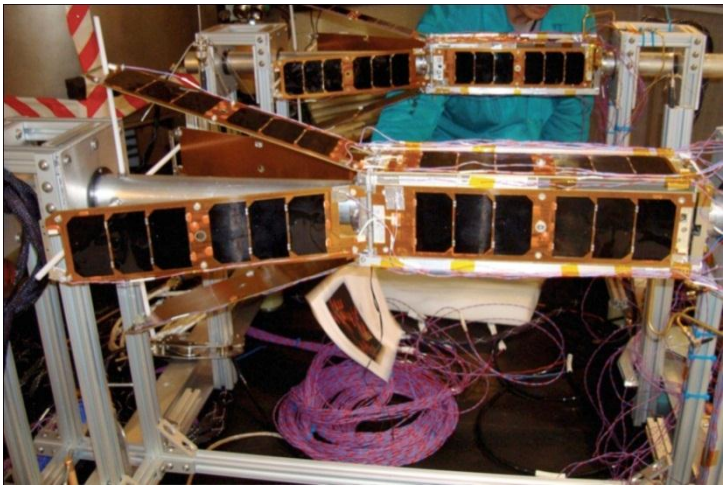

Figure 1-6: Two QbX-1 and QbX-2 [NRL]

The attitude control system of the QbX satellites included 3 magnetorquers and 3 reaction wheels. A tri-axis magnetometer was the only attitude sensor on-board, thus the ADCS lacked full attitude determination capability. The pointing controller used a modified B-dot controller and passive stabilization techniques to align the spacecraft body with the orbit

Stellenbosch University https://scholar.sun.ac.za

frame without using attitude knowledge. The payload pointing accuracy during experimentations was less than 5° [19].

1.3.4 **Nanosatellite Test Platforms**

Numerous research papers and online documents, describing the HIL facilities at different laboratories, were investigated in this section. As stated by Juana L. Schwartz, Mason A. Peck and Christopher D. Hall, in paper [20], air-bearings have been used to verify the ADCS software and hardware for nearly 45 years. This paper provides an overview of air-bearing based spacecraft simulators with several examples of planar and rotational air bearing systems. The planar systems "give a payload freedom to translate and spin" while the rotational air-bearing systems "simulate 3-axis satellite attitude dynamics". The rotational air-bearings in the "Tabletop" configuration provide freedom in only the yaw axis while the "Dumbbell" style configuration has freedom in both the yaw and the roll axes [20].

Helmholtz Cage is also part of several nanosatellites test facilities to generate a magnetic field vector for magnetometer and magnetorquer operation [21, 22, 23, 24]. The Helmholtz cage system comprises of a set of three orthogonally placed Helmholtz coil pairs to generate a three dimensional magnetic field vector. The Helmholtz coil can be described as a pair of coils, both similar in dimensions, having equal number of turns and carrying the same amounts of current to generate a homogenous magnetic field between the two coils [25]. The profile of magnetic field generated by the coils depends on the separating distance between the coils and the shape of the coils. The square shaped coils are simpler to design and easier to manufacture. Moreover, these generate larger homogenous magnetic field in comparison to the circular shaped coils of a similar size [26].

Paper [21] discusses the application of Helmholtz cage, designed and built by students at the Delft University of Technology, to test the passive magnetic attitude control system of the Delfi-C^3 nano satellite. Similarly, the integrated test facility for nanosat assessment and verification at Space Dynamics Laboratory (SDL), as described by [22], contains a three axis Helmholtz Cage with closed-loop field control in order to test magnetometer/torquer. Inside this cage, the magnetic field control can be controlled to about 10 nano-Tesla accuracy. A spherical air bearing made with non-ferrous magnetic material is used in three-Axis ADCS simulator for the HIL testing [22].

Stellenbosch University https://scholar.sun.ac.za

Meghan K Quadrino, in his Master's thesis, at the Space Systems Laboratory of Massachusetts Institute of Technology (MIT), tested several ADCS algorithms on "a one-degree-of-freedom rotation test set-up inside of a Helmholtz Cage magnetic field simulator". The B-dot detumble controller was one of the controllers that was tested in the presence of a constant magnetic field vector inside the cage. Rate measurements during the tests were taken from an inertial measurement unit (IMU) [24]. Paper [23] presents the design, construction and initial testing of the Helmholtz Cage around a spherical bearing used for the CubeSat ADCS lab testing at MIT.

Figure 1-7: HIL test facility at SDL [22]

Figure 1-8: MIT Space Systems Laboratory's Helmholtz Cage [23, 24]

Figure 1-9: The Helmholtz Cage at Delft University of Technology [21]

Stellenbosch University https://scholar.sun.ac.za

The CubeSat three-axis simulator (CubeTAS) testbed, described by Chesi [26], has a hollow hemispherical structure containing 3 RW units, 3 magnetorquers coils, a sun sensor, IMU and an OBC. The structure and its contents float over an air bearing cup to demonstrate 3 degree of freedom (dof) motion for large angles in a quasi-frictionless environment. The test setup also has 3 Helmholtz coils to verify the attitude determination techniques, which are based on the magnetic field measurements. Results of a sample experiment for a quaternion feedback controller on CubeTAS are also presented in the paper [26].

1.4 Thesis Outline

Chapter 2 presents the theoretical background of the ADCS concepts. Satellite dynamics, kinematics and the coordinate frames for attitude description are explained. Moreover, an analysis of disturbance torques on the satellite body in its orbit is also presented.

Chapter 3 entails the hardware selection for the ADCS design. It also illustrates the design of the sensors and actuators interface electronics, along with details of the low level software of the magnetic and wheel control boards.

Chapter 4 discusses the attitude determination algorithms along with their derivations and implementations. In the later section, numerous magnetic and wheel controllers for satellite attitude control are illustrated.

Chapter 5 describes the components of the MATLAB Simulink simulation platform to evaluate the ADCS performance of the nanosatellite in its orbit. Moreover, it discusses the ADCS mission modes, mode transitions and the ADCS performance in each mode.

Chapter 6 focuses on the HIL testing for the nanosatellite ADCS. It provides details of the HIL test environment, the HIL test platform, the ADCS test configurations and the HIL test results for various test schemes.

Chapter 7 concludes the thesis with a summary of the research work, recommendations and possible improvements.

Stellenbosch University https://scholar.sun.ac.za

2. Theoretical Background

This chapter presents the fundamental concepts that are essential to understand the process of ADCS design for a satellite mission. These include definitions of the coordinate reference frames in which the attitude of a satellite is described, the ways to represent the attitude and the satellite attitude dynamics. The later part of this chapter illustrates the disturbance torques acting on a satellite body in orbit and presents the calculations of worst case disturbance torques for the mission satellite.

2.1 Attitude Description

Satellite attitude is defined as the orientation of a satellite body relative to a reference frame. There are numerous ways to describe the attitude of a satellite. The coordinate frames which are used in satellite attitude representation and some methods to express the attitude are explained in this section.

2.1.1 Coordinate Frames

"The most important coordinate frame systems", used for the ADCS design are all centered at the spacecraft [27]. However, in obtaining reference vectors for an earth orbiting satellite ADCS and for orbit propagation, Earth-Centered Coordinates systems are used.

2.1.1.1 Spacecraft-Centred Coordinates

The spacecraft-centred coordinate frames that were used in the ADCS design of this project are Inertial Reference Coordinates (IRC) frame, Body Reference Coordinates (BRC) frame and Orbit Reference Coordinates (ORC) frame.

2.1.1.1.1 Inertial Reference Coordinates

The IRC frame is the reference frame for dynamic equations of motion of the satellite. As the name suggests, the inertial reference frame remains nearly fixed in inertial space. The X-axis and the Z-axis of the IRC are in the orbital plane, while the Y-axis points in the orbit anti-normal direction. The Z-axis is defined to be in the direction opposite to the perigee vector or

Stellenbosch University https://scholar.sun.ac.za

in other words, pointing towards the centre of the earth at the perigee point (the closest point to the earth in an elliptical orbit). The X-axis completes the right hand set in the Cartesian plane.

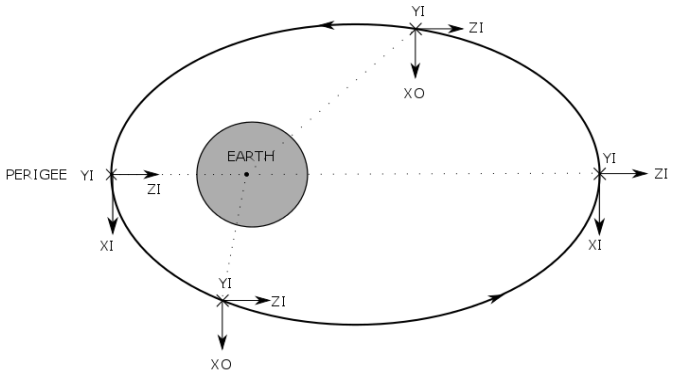

Figure 2-1: Inertial Reference Coordinates frame definition

2.1.1.1.2 Orbit Reference Frame

The ORC frame is the reference frame to describe the attitude of a satellite. This frame rotates with the orbital motion and is fixed to the orbital position in inertial space. The X- and the Z-axis of the ORC frame are in the orbital plane while the Y-axis points in the orbit anti-normal direction. The Z-axis in the ORC points towards the centre of the earth (nadir) and the X-axis completes the orthogonal set in the Cartesian plane. For the case of a circular orbit, the X-axis of the ORC points in the velocity direction of orbital motion.

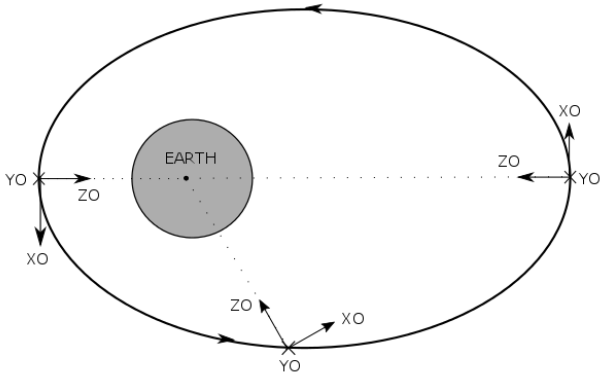

Figure 2-2: The Orbit Reference frame definition

2.1.1.1.3 Body Reference Frame

The BRC frame is the reference frame, to specify the mounting orientations of sensors and actuators in a satellite. It also serves as reference frame for sensors measurements and

Stellenbosch University https://scholar.sun.ac.za

actuator outputs. The BRC frame is fixed to the satellite body and the axes of the frame are chosen to coincide with the ORC frame, when the satellite is in a nominal nadir pointing orientation.

2.1.1.2 Earth- Centered Coordinates

The position vectors to the objects, seen by the spacecraft, are obtained in the Earth-Centered Inertial Coordinates (ECI) frame. Moreover, the equations of orbital motion are also described in the ECI frame. The X- and Y-axis of the ECI frame are in equatorial plane while the Z- axis of the ECI frame is along the earth's rotation axis. The X-axis points to the vernal equinox direction and the Y-axis completes the right hand set of unit vectors triad.

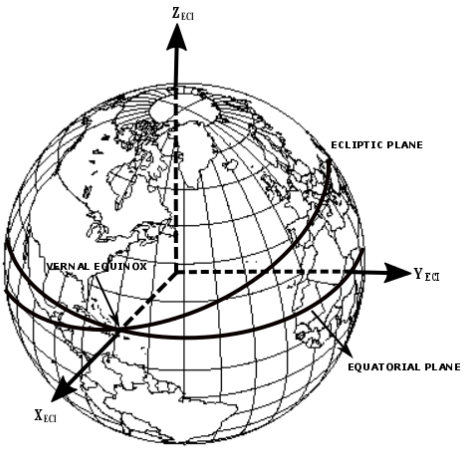

Figure 2-3: ECI frame axis definitions

The output of the International Geomagnetic Reference Field (IGRF) model and GPS position sensor are given in Earth Centered Earth Fixed (ECEF) frame. The ECEF frame is defined such that its Z-axis is along the rotation axis of the earth, same as in the ECI frame. The X-axis in the ECEF frame is in the direction of (0° latitude, 0° longitude) point on the surface of the earth. Therefore, the ECEF frame rotates with the earth in inertial space and all the points on the earth remain fixed in the ECEF frame.

2.1.2 **Attitude Representation**

Attitude is defined as the orientation of one reference frame with reference to another reference frame. For the case of a satellite, it is the orientation of satellite BRC frame with

Stellenbosch University https://scholar.sun.ac.za

reference to the ORC frame. The attitude can be expressed through several representations. Some commonly used attitude representations for satellite attitude are Rotation Matrices or Direction Cosine Matrix (DCM), the Euler angles and the Quaternions parameters.

2.1.2.1 Direction Cosine Matrix

A vector described in one reference frame can be transformed to another reference frame by multiplying it with the DCM. Also known as the Rotation Matrix, the DCM is a 3 ×3 orthonormal matrix whose elements are projections of the components of one reference frame on the other reference frame. The 9 elements of the DCM have the complete description of the attitude.

The notation $\mathbf{C}^{A/B}$, is used to denote the direction cosine matrix $\mathbf{C}$, that describes the orientation of frame-A with respect to frame-B. Similarly, $\mathbf{C}^{B/A}$ is used for the DCM to describe the orientation of frame-B relative to frame-A [28].

If a vector has its components a_1, a_2, a_3 in frame-A then the same vector can be represented in frame-B by the components b_1, b_2, b_3 , where

$$\begin{bmatrix} b_1 \\ b_2 \\ b_3 \end{bmatrix} = \begin{bmatrix} C_{11} & C_{12} & C_{13} \\ C_{21} & C_{22} & C_{23} \\ C_{31} & C_{32} & C_{33} \end{bmatrix} \begin{bmatrix} a_1 \\ a_2 \\ a_3 \end{bmatrix} = \mathbf{C}^{B/A} \begin{bmatrix} a_1 \\ a_2 \\ a_3 \end{bmatrix}$$

The attitude description in the DCM format requires calculation of 9 elements therefore has more calculation overhead as compared to the other representations.

2.1.2.2 Euler Angles

The attitude of a satellite can also be described by three Euler rotations about the rotated body fixed reference frame. The first rotation can be about any arbitrary body-fixed axis, the second rotation can be around any of the either two axis in the rotated frame that was not used for the first rotation. Finally the third rotation can be around any of the two axes in the rotated frame that was not used in the second rotation. The sequence of the rotations is also significant in describing the Euler attitude. The rotations about X-axis, Y-axis and Z-axis are mentioned as roll (ϕ), pitch (θ) and yaw (ψ) respectively.

Stellenbosch University https://scholar.sun.ac.za

Each Euler rotation can be expressed as a rotation matrix and the product of the three Euler rotation matrices gives the DCM. Euler 2-1-3 rotations were used to express the attitude in this project. Figure-3, illustrates the Euler 2-1-3 rotation sequence.

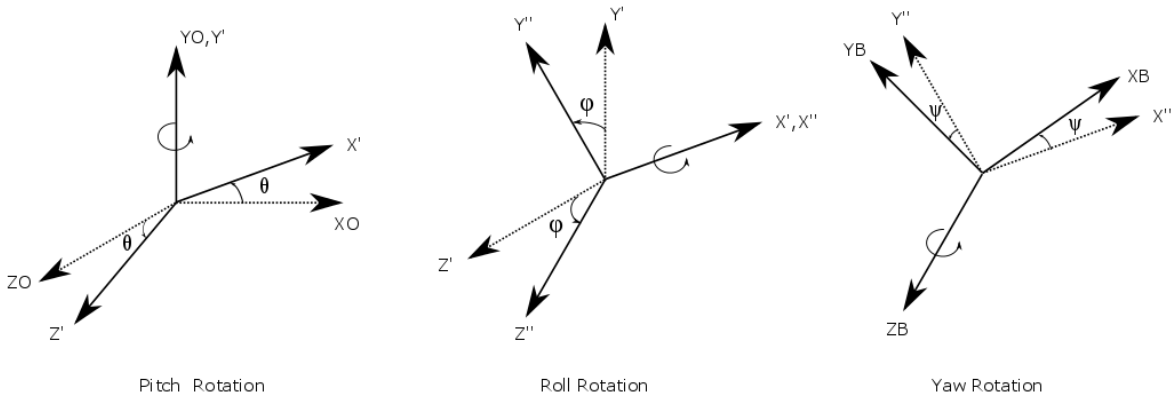

Figure 2-4: Euler 2-1-3 rotation sequence

If $\mathbf{C}(\theta)$, $\mathbf{C}(\phi)$ and $\mathbf{C}(\psi)$ are the rotation matrices for the pitch, roll and yaw rotation respectively then the direction cosine matrix $\mathbf{C}$ for the Euler 2-1-3 sequence can be calculated as,

$$\mathbf{C} = \mathbf{C}(\psi)\mathbf{C}(\phi)\mathbf{C}(\theta)$$

$$= \begin{bmatrix} \cos\psi & \sin\psi & 0 \\ -\sin\psi & \cos\psi & 0 \\ 0 & 0 & 1 \end{bmatrix} \begin{bmatrix} 1 & 0 & 0 \\ 0 & \cos\phi & \sin\phi \\ 0 & -\sin\phi & \cos\phi \end{bmatrix} \begin{bmatrix} \cos\theta & 0 & -\sin\theta \\ 0 & 1 & 0 \\ \sin\theta & 0 & \cos\theta \end{bmatrix}$$

$$= \begin{bmatrix} \cos\theta\cos\psi + \sin\theta\sin\phi\sin\psi & \cos\phi\sin\psi & -\sin\theta\cos\psi + \cos\theta\sin\phi\sin\psi \\ -\cos\theta\sin\psi + \sin\theta\sin\phi\sin\psi & \cos\phi\cos\psi & \sin\theta\cos\psi + \cos\theta\sin\phi\sin\psi \\ \sin\theta\cos\phi & -\sin\phi & \cos\theta\cos\phi \end{bmatrix} \quad (2.1)$$

If the elements of the $\mathbf{C}$ matrix are represented by C_{ij} then the Euler angles can be expressed in terms of DCM elements,

$$\phi = -\operatorname{asin}(C_{32}) \quad (2.2)$$

$$\theta = \operatorname{atan2}\left(\frac{C_{31}}{C_{33}}\right) \quad (2.3)$$

Stellenbosch University https://scholar.sun.ac.za

$$\psi = \text{atan2}\left(\frac{C_{12}}{C_{22}}\right) \tag{2.4}$$

Attitude representation in Euler angles provides clear physical interpretations for human visualizations. However, it suffers from singularities at certain angles. Moreover, the calculations involve trigonometric functions and numerical integration is inconvenient due to the presence of non-linear terms [29].

2.1.2.3 Quaternions

Euler symmetric parameters (quaternions) describe the attitude of a satellite by a single rotation about a unit vector, named as the Euler axis. Quaternions offer advantages such as non-singularity, conversion to DCM without involving trigonometric functions and convenient numerical integration. Therefore, they are widely used in attitude determination and control algorithms. The quaternions attitude is represented by four elements with three vector elements and one scalar component. As the rotation is performed around the Euler axis, the components of the unit vector describing the Euler axis are the same in the BRC and ORC.

If the Euler axis is defined by unit vector, $\mathbf{e} = [e_1 \quad e_2 \quad e_3]^T$ and θ is the Euler rotation angle then the attitude quaternion is defined as,

$$\mathbf{q} = \begin{bmatrix} q_1 \\ q_2 \\ q_3 \\ q_4 \end{bmatrix} = \begin{bmatrix} e_1 \sin\left(\frac{\theta}{2}\right) \\ e_2 \sin\left(\frac{\theta}{2}\right) \\ e_3 \sin\left(\frac{\theta}{2}\right) \\ \cos\left(\frac{\theta}{2}\right) \end{bmatrix} \tag{2.5}$$

The elements of $\mathbf{q}$ are interdependent and are constrained by the condition,

$$q_1^2 + q_2^2 + q_3^2 + q_4^2 = 1 \tag{2.6}$$

Stellenbosch University https://scholar.sun.ac.za

The DCM can be expressed in terms of quaternions,

$$\mathbf{C} = \begin{bmatrix} q_1^2 - q_2^2 - q_3^2 + q_4^2 & 2(q_1q_2 + q_3q_4) & 2(q_1q_3 - q_2q_4) \\ 2(q_1q_2 - q_3q_4) & -q_1^2 + q_2^2 - q_3^2 + q_4^2 & 2(q_2q_3 + q_1q_4) \\ 2(q_1q_3 + q_2q_4) & 2(q_2q_3 - q_1q_4) & -q_1^2 - q_2^2 + q_3^2 + q_4^2 \end{bmatrix} \tag{2.7}$$

Conversely, the quaternion parameters can be calculated from the DCM elements using Equations (2.8) to (2.11),

$$q_4 = \pm\frac{1}{2}\sqrt{1 + C_{11} + C_{22} + C_{33}} \tag{2.8}$$

$$q_1 = \frac{1}{4q_4}(C_{23} - C_{32}) \tag{2.9}$$

$$q_2 = \frac{1}{4q_4}(C_{31} - C_{13}) \tag{2.10}$$

$$q_3 = \frac{1}{4q_4}(C_{12} - C_{21}) \tag{2.11}$$

Any one of the four quaternion components can be calculated first by changing the signs of C_{11}, C_{22}, C_{33} appropriately in Equation (2.8) and can be used to calculate the rest of the quaternion components. However, taking the largest component of the quaternion to calculate the remaining three components can minimize the numerical inaccuracy [30, 27].

2.2 Satellite Equations of Motion

The rotational motion of a satellite is modelled by two sets of equation referred as: the dynamic equation of motion and the kinematic equation of motion [31].

2.2.1 Dynamics Equations

The Euler dynamics equation of motion states that the time rate of change of angular momentum of the satellite body in inertial space is equal to the sum of all torques being applied on the satellite body. The applied torques can either be internal (e.g. RW torques) or external (e.g. environmental disturbances) and are categorized as control torques ($\mathbf{N}_C$) and disturbance torques ($\mathbf{N}_D$).

Stellenbosch University https://scholar.sun.ac.za

$$\mathbf{I}\dot{\boldsymbol{\omega}}_{\mathrm{B}}^{\mathrm{I}} = \mathbf{N}_{\mathrm{C}} + \mathbf{N}_{\mathrm{D}} \tag{2.12}$$

where, $\mathbf{I}$ is the inertia tensor matrix of the satellite and $\boldsymbol{\omega}_{\mathrm{B}}^{\mathrm{I}}$ represents the body rates of the satellite with respect to inertial reference frame. The control torques are the torques from satellite actuators that typically include magnetic torques ($\mathbf{N}_{\mathrm{m}}$) and wheel torques ($\mathbf{N}_{\mathrm{w}}$).

$$\mathbf{N}_{\mathrm{C}} = -\mathbf{N}_{\mathrm{RW}} + \mathbf{N}_{\mathrm{m}} \tag{2.13}$$

For an LEO satellite, the external disturbance torques include gravity gradient torques ($\mathbf{N}_{\mathrm{GG}}$) , aerodynamic torques ($\mathbf{N}_{\mathrm{aero}}$) and magnetic dipole disturbance torques ($\mathbf{N}_{\mathrm{Mag}}$). While, internal disturbance torques include disturbances from reaction wheel ($\mathbf{N}_{\mathrm{RW}}$) and the torques from gyroscopic coupling ($\mathbf{N}_{\mathrm{Gyro}}$).

$$\mathbf{N}_{\mathrm{D}} \cong \mathbf{N}_{\mathrm{GG}} + \mathbf{N}_{\mathrm{aero}} + \mathbf{N}_{\mathrm{m}} + \mathbf{N}_{\mathrm{RW}} - \mathbf{N}_{\mathrm{Gyro}} \tag{2.14}$$

and

$$\mathbf{N}_{\mathrm{Gyro}} = \boldsymbol{\omega}_{\mathrm{B}}^{\mathrm{I}} \times \left(\mathbf{I}\boldsymbol{\omega}_{\mathrm{B}}^{\mathrm{I}} + \mathbf{h}_{\mathrm{w}}\right) \tag{2.15}$$

where, $\mathbf{h}_{\mathrm{w}}$ represents the angular momentum of the wheels.

2.2.2 Kinematics Equations

Satellite attitude kinematics refers to the change in attitude without taking into account the torque that brings about this change. Quaternions are used in kinematics description as they are suitable for numerical integration of equation of motions. The kinematic equation of motion in quaternions representation is described as following,

$$\dot{\mathbf{q}} = \frac{1}{2}\boldsymbol{\Omega}\mathbf{q} \tag{2.16}$$

where, $\boldsymbol{\Omega}$ matrix contains the components of the orbit referenced angular velocities of the satellite ($\boldsymbol{\omega}_B^O$) and given as follows,

$$\boldsymbol{\Omega} = \begin{bmatrix} 0 & \omega_{oz} & -\omega_{oy} & \omega_{ox} \\ -\omega_{oz} & 0 & \omega_{ox} & \omega_{oy} \\ \omega_{oy} & -\omega_{ox} & 0 & \omega_{oz} \\ -\omega_{ox} & -\omega_{oy} & -\omega_{oz} & 0 \end{bmatrix} \tag{2.17}$$

Stellenbosch University https://scholar.sun.ac.za

The angular rates from dynamics equation of motion are in the IRC ($\boldsymbol{\omega}_B^I$) that can be transformed to the ORC ($\boldsymbol{\omega}_B^O$) to be used in Equation (2.17) using following relation,

$$\boldsymbol{\omega}_B^O = \boldsymbol{\omega}_B^I - \boldsymbol{\omega}_O^I \tag{2.18}$$

If $\omega_0(t)$ is the angular rate of the ORC frame with reference to the IRC ($\boldsymbol{\omega}_O^I$) and '$\mathbf{A}^{B/O}$' is the DCM from the ORC to the BRC, then $\boldsymbol{\omega}_B^O$ can be calculated as,

$$\boldsymbol{\omega}_B^O = \boldsymbol{\omega}_B^I - \mathbf{A}^{B/O}\begin{bmatrix} 0 \\ -\omega_0(t) \\ 0 \end{bmatrix} \tag{2.19}$$

Thus having information of the applied torques, the inertial referenced body rates can be obtained from Equation (2.12). These inertial body rates are then transformed to orbit reference body rates using Equation (2.19). The orbit reference body rates are then used in Equation (2.16) to obtain the quaternion rates $\dot{\mathbf{q}}$, which are numerically integrated to propagate the attitude.

2.3 Disturbance Torques

The satellites experience various disturbance torques in its orbit. These disturbance torques may vary with orbital altitude and satellite body geometry. A summary of disturbance torques, analysed in this project, is presented in this section

2.3.1 Gravity Gradient Torque

The gravity gradient (GG) torques acts on an axially non-symmetric satellite body, when the satellite has a non-zero attitude in roll or pitch. Due to the offset in roll or pitch, one end of satellite body is closer to the earth as compared to the other end and the closer part experience more gravitational pull as compared to the farther part that results a torque [30]. The GG torques is expressed in vector form as,

$$\mathbf{N}_{\mathrm{GG}} = \frac{3GM}{R^3}\left[I_{zz} - \frac{I_{xx} + I_{yy}}{2}\right](\mathbf{z}_0 . \mathbf{z}_\mathrm{b})(\mathbf{z}_0 \times \mathbf{z}_\mathrm{b}) \tag{2.20}$$

where,

GM = Earth gravitational constant

R = distance of the satellite from the centre of the Earth

Stellenbosch University https://scholar.sun.ac.za

$\mathbf{z}_0$ = nadir pointing unit vector in the BRC

$\mathbf{z}_b$ = Z-axis unit vector of satellite body

2.3.2 Aerodynamic Torque

The aerodynamic torque is significant in low altitude orbits due to the higher atmospheric density. An LEO satellite experiences aerodynamic forces in orbit acting in anti-velocity direction and if the centre of pressure (CoP) is displaced from the centre of mass (CoM) of the satellite body, these forces result into a torque. The aerodynamic torque is expressed in vector form as [31],

$$\mathbf{N}_{\text{aero}} = \rho_a V^2 A_p (\mathbf{c}_p \times \mathbf{V}_{\text{unit}}) \tag{2.21}$$

where,

ρ_a = atmospheric density

V = magnitude of satellite orbital velocity

$\mathbf{V}_{\text{unit}}$ = satellite velocity unit vector

A_p = total projected area of satellite body in velocity direction

$\boldsymbol{c}_p$ = vector between CoM and CoP of the satellite

2.3.3 Magnetic Disturbance Torque

The satellite in its orbit also experiences disturbance torque due to the residual magnetic dipole moment inside the body. This residual magnetic field tries to align itself with the local magnetic field, like a compass needle, causing a torque. Although, the model of local earth magnetic field is complex, however for the magnetic torques calculations, use of a simple dipole model is sufficient [32]. The maximum magnetic torque can be evaluated as follows,

$$\mathbf{N}_{\text{dm}} = \mathbf{M}_r \times \mathbf{B} \tag{2.22}$$

where, $\mathbf{M}_r$ is the residual dipole moment of the satellite and $\mathbf{B}$ is the maximum magnetic field in the orbit.

Stellenbosch University https://scholar.sun.ac.za

2.3.4 **Reaction Wheel Imbalance**

Non-uniform mass distribution of the RW disk behaves like mass lumps at the end of the disk causing two types of imbalances: static and dynamic. Static imbalance causes a radially outward force. This force is sinusoidal and related to the wheel angular velocity. The static imbalance force for a RW mounted along the X-axis and spinning at angular speed ω , is calculated as follows,

$$\mathbf{F}_{xyz} = U_s\omega^2 \begin{bmatrix} 0 \\ \sin(\omega t) \\ \cos(\omega t) \end{bmatrix} \tag{2.23}$$

where, U_s is the coefficient of static imbalance, usually specified by the wheel manufacturer. The disturbance torque resulting from static imbalance force is a function of mounting location of the wheel in the satellite. If $\mathbf{r}_{RWx}$ be the position vector of the X-axis RW from the CoM of the satellite, then the static imbalance disturbance torques ($\mathbf{N}_{xs}$) can be expressed as,

$$\mathbf{N}_{xs} = \mathbf{r}_{RWx} \times \mathbf{F}_{xyz} \tag{2.24}$$

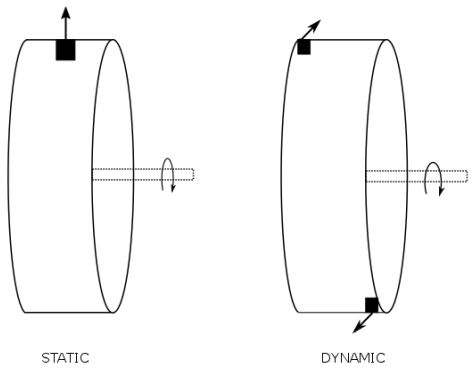

Figure 2-5: RW static and dynamic imblance

The mass lumps (due to wheel imbalance) also results into misalignment of the principal moment of inertia and the spin axis, causing the dynamic imbalance. The effect of dynamic imbalance is the precession motion of wheel and the resulting disturbance torques ($\mathbf{N}_{xd}$) can be calculated as,

Stellenbosch University https://scholar.sun.ac.za

$$\mathbf{N}_{xd} = U_d \omega^2 \begin{bmatrix} 0 \\ \sin(\omega t) \\ \cos(\omega t) \end{bmatrix} \tag{2.25}$$

where, U_d is the coefficient of dynamic imbalance, usually specified by the wheel manufacturer [33]. The calculations of significant disturbance torques for the mission satellite, in worst case scenario are presented in Table 2-1.

Table 2-1: The worst case disturbance torques

Disturbance	**Worst Case Assumptions**	**Torque**(μNm)
N_{GG}	$\mathrm{R} = 6878.1\ \mathrm{km}, \theta = 45°$	0.42
N_{AERO}	$\rho_a = 2 \times 10^{-12}\ \mathrm{kg/m^3}, \mathrm{C_d} = 2.5, A_p = 0.118\mathrm{m^2}, C_p = 0.05\ \mathrm{m}$	0.86
N_{dm}	$M_r = 0.1\mathrm{Am^2}, B_{\max} = 45\mu\mathrm{T}$ [30]	4.5
Worst Case cumulative disturbance torque N_d		5.78

The orbital period T_o for the mission orbit of altitude 500 km is 5677.2 s [32]. The maximum angular momentum build-up h_d due to the worst case cumulative disturbance torque from Table 2-1 over one orbital period can be calculated as,

$$h_d = N_d\, T_o \tag{2.26}$$

$$= 32.8\ \mathrm{mNms}$$

2.4 Summary

The satellite attitude is defined as the orientation of body reference frame relative to orbit reference frame. Attitude can be described as DCM, Euler angles or Quaternions etc. The DCM representation contains six redundant parameters. Euler angles provide good human interpretations but have singularities at certain angles. The quaternion parameters are more convenient way for attitude representation. Attitude motion of a satellite is modelled with dynamic and kinematic equations of motion. The models of control and disturbance torques are also part of satellite dynamics model. The external and internal disturbance toques with their mathematical representations and worst case calculations were discussed in this chapter.

Stellenbosch University https://scholar.sun.ac.za

3. The ADCS Hardware

The ADCS hardware of a satellite comprises of an OBC for processing the ADCS algorithms, sensors for attitude determination and actuators to implement the attitude control commands. The OBC and the ADCS sensor modules used in this project were developed at the ESL previously. For this project, the driver and the control circuitry for the actuators were designed and developed. In this regard, two printed circuit boards (PCB) were designed and manufactured. One PCB was for the magnetic control and the other PCB for the RW control. This chapter describes the selection of sensors and the actuators for the satellite ADCS based on the mission requirements. In the later section of this chapter, the hardware design details of the magnetic and the RW control boards are illustrated.

3.1 The Sensors

An attitude sensor measures a reference vector in its sensor frame of reference which is transformed to the BRC frame by multiplying it with the mounting matrix of the sensor in the satellite body. These measured reference vectors, expressed in the BRC frame, are compared with their modelled reference vectors in the ORC frame for attitude determination. The reference vectors normally include the unit sun vector which is provided by the sun sensors, the earth magnetic field vector measured by the magnetometer and the nadir vector that is given by the earth horizon sensor. Similarly, the star sensor measures stars coordinates in the BRC frame and compares it with known star pointing vectors in the star catalogue to provide the attitude information [27].

The attitude sensors are selected on the basis of the attitude knowledge requirements for a specific satellite mission and the attitude knowledge requirements are derived from the pointing accuracy requirements for the mission. The choice of sensors also depends on the mission orbit of a satellite. For instance, a magnetometer is part of most of the ADCS hardware suites for the LEO satellites. However, it is not suitable to be used in high altitude orbit satellites because of the weaker geomagnetic field strength. Similarly, the Infrared earth sensors can only be utilized at altitudes higher than a minimum threshold value. Table 3-1

Stellenbosch University https://scholar.sun.ac.za

summarizes the characteristics of the sensors normally used for satellite attitude determination.

Table 3-1: ADCS sensors [32, 34]

ADCS Sensors	**Characteristics**
Sun Sensors	Reliable and simple, require unobstructed view. Accuracy: 1 arc min to 2°
Earth Sensors (ES)	Mounted on the earth deck, always available for IR based ES, orbit dependent, requires unobstructed view. Accuracy: 0.1° to 1° for LEO
Magnetometers	Simple, reliable and light weight. The uncertainties and variability in the earth magnetic field dominate the accuracy. Usable at the orbital altitude below 6000 km. Accuracy: 0.5° to 3°
Star Sensors	The most accurate reference source, complex, normally heavy, power hungry, requires unobstructed view of the stars. The sun and the moon should not be in the field of view (FOV) during measurements. Accuracy: 2 arc-sec to 0.03°
Inertial Rate Sensors	No external reference, orbit independent, subject to drift.

The ADCS sensors selected for the mission satellite include a magnetometer that is required primarily to get the magnetic field measurements for using in the rate damping and the other magnetic controllers. The solar cells based Coarse Sun Sensors (CSS) were mounted on the 6 facets of the satellite body to be used for sun finding and coarse sun tracking modes. In order to fulfil the pointing requirements as mentioned in Section 1.2.2, during the target pointing manoeuvres for image acquisition, a star tracker had to be included in the mission ADCS hardware. Due to its narrow FOV and high power consumption, the star tracker was only utilized during the imaging mode. A Fine Sun Sensor (FSS) and a Horizon Sensor (HS) were chosen to be used during the nominal sun pointing and the nadir pointing modes (mode definitions shall be explained in Section 5.3) , where pointing accuracy requirements were not as stringent as for the imaging.

Stellenbosch University https://scholar.sun.ac.za

3.1.1 **Magnetometer**

A magnetometer is the most important ADCS sensor as its data readout is available throughout the orbit and it is the only sensor required for the B-dot rate damping magnetic controller. Moreover, the magnetometer read-outs are also used for the angular rate estimates in the detumbling phase of the satellite mission.

The RM3000, three axis magneto-inductive magnetometer, from PNI® Sensor Corporation was selected for the project. The QbX CubeSat mission also carried a magnetometer based on the PNI® magneto-inductive technology, therefore the technology has a space heritage as well. RM3000 has a linear measurement range of ± 200 μT which is far wider than the required range of ± 60 μT in the mission orbit. The specified system noise for RM3000 is 30 nT. The measurement output of the magnetometer is a 32 bit integer value for each axis, which is provided on serial peripheral interface (SPI) protocol. The current consumption of RM3000 for all three axes is less than 200 μA [35].

Figure 3-1: RM3000 magnetometer components and the evaluation board

The Magnetic Control Board samples the magnetometer and transmits the measurement data to the OBC. RM3000 was also calibrated for the sensitivity and the offset parameters inside the Helmholtz Cage. The details of the calibration method and the calibration results are discussed in Section 6.3.

3.1.2 **FSS and Horizon Sensor Module**

CubeSense: an integrated fine sun sensor and horizon sensor module was developed at ESL and has flight heritage on the QB50 precursor satellite. The module has dual low power CMOS camera modules with 640×480 pixels and 190° FOV fisheye lenses. One camera gives the sun vector direction in its full hemisphere FOV, while the other camera provides the nadir vector direction on the basis of the earth disc illumination from reflected sunlight [36].

Stellenbosch University https://scholar.sun.ac.za

The nadir/horizon sensor has a 3σ accuracy of less than 0.3°, having full earth in its FOV and the 3σ accuracy of the sun sensor is also less than 0.3°, provided that the sun is in ±40° of the sensor's bore sight [37]. The nadir camera was chosen to be placed on the +Z facet of the satellite that points towards the centre of the earth while the satellite is in zero attitude condition. The FSS camera bore sight was chosen to be aligned with the –Y axis of the BRC frame as the sun is towards the –Y facet of the satellite in the nominal zero attitude condition.

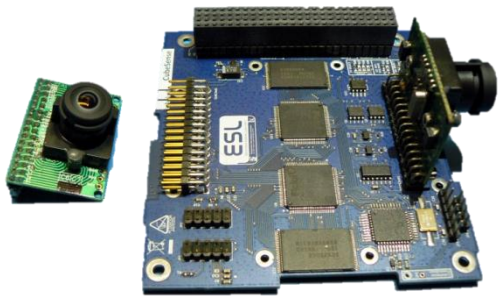

Figure 3-2: CubeSense integrated FSS and horizon sensor [37]

3.1.3 Star Tracker

The specifications of the CubeStar, a nano star tracker module developed at the ESL, were used in the mission ADCS simulations. CubeStar is compatible with the CubeSat standards and is capable of operating in full autonomous mode. It can be configured to output the modelled and the measured star vectors or to provide the attitude estimates, directly in the form of the inertial quaternions, at a sample rate of 1 Hz. The cross bore 1σ accuracy of the CubeStar is 0.01° and for the roll, the accuracy is 0.03°. The FOV of the CubeStar is 52°×27°. The module weighs only 56 g (without Baffle) and its maximum power consumption is 0.5 W [38].

Figure 3-3: CubeStar nano star tracker [38]

Stellenbosch University https://scholar.sun.ac.za

The star tracker requires placement in the satellite body such that the earth and the sun should not be in its FOV during the estimations. A placement configuration for the star camera is illustrated in Figure 3-4. In this configuration, the star camera is mounted on +Y facet of the satellite, which is the opposite facet of the solar panels. In the BRC frame, the star camera is placed in the YZ plane such that it has an angle of 45° with the +Y and the –Z-axis as shown in the figure.

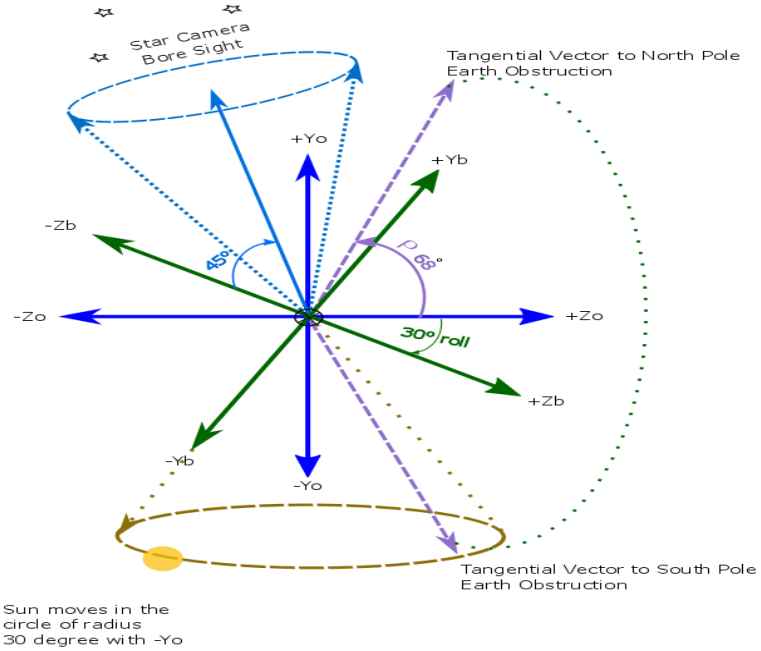

Figure 3-4: Star tracker placement illustration

The sun and the earth obstructions were investigated in the case of a 30° roll offset for the placement configuration in Figure 3-4. The angular radius of the earth disk, as seen by the satellite at an altitude (h) of 500 km, is determined as follows,

$$\rho = \sin^{-1}\left(\frac{R_E}{R_E + h}\right) = 68° \tag{3.1}$$

where, R_E represents the radius of the Earth. For the case of an SSO orbit, the sun angle to the orbital plane (β) remains constant. A satellite moving in the SSO orbit observes the sun, circulating around the orbital normal in a circle of angular radius ($90° - \beta$) . The β angle is dependent on the local time of ascending node (LTAN) of the orbit and for the mission orbit, the β angle is 60°. Therefore, the angular radius of the sun's relative motion,

Stellenbosch University https://scholar.sun.ac.za

as seen from the satellite, is 30°. As evident in Figure 3-4, neither the sun nor the earth is in the FOV of the star camera for a roll offset of 30°.

3.1.4 Rate Sensor

The three axis gyro contained in the STIM300 IMU, was selected to be used for the mission ADCS. The IMU includes 3 high accuracy Micro-Electromechanical Systems (MEMS) based gyros with 24 bit resolution data output. The specified measurement noise for the gyro is less than 28 arc-second per second and the bias drift value is less than 5 arc-second per second [39]. The placement of the IMU in the satellite was chosen such that its measurement axes are aligned with the BRC frame.

Figure 3-5: STIM300 inertial measurement unit [39]

3.2 The On-board Computer

The CubeComputer module, a general purpose OBC and part of ESL ADCS hardware suit, shall be used as an OBC for the mission ADCS. The module utilizes a high performance, low power 32-bit ARM Cortex-M3 based microcontroller (MCU). In addition to the internal watchdog, the module also incorporates an external watchdog for added reliability. It features 256 KB memory of EEPROM and 4 MB of Flash for code storage. Fault tolerant schemes to cater for the single event upset (SEU) and the single event latch-up (SEL) are also employed in the CubeComputer design. The power consumption for the module is less than 200 mW. The CubeComputer has communication interface on I^2C interface and also provides the CAN and the UART interfaces. The module is successfully qualified through the vibration and thermal vacuum tests. The module has also qualified the radiation tests of total ionization dose (TID) with 20 krad radiation dose and single event effect (SEE) at 60

Stellenbosch University https://scholar.sun.ac.za

MeV level. The CubeComputer module was flown as the ADCS OBC in the QB50 precursor satellites and thus has a space heritage as well [40].

Figure 3-6: CubeComputer an on-board computer module [40]

3.3 The Actuators

The reaction wheels were selected for the pointing controllers as one of the requirements of the mission is fine pointing control as mentioned in Section 1.2.2. A reaction wheel provides the manoeuvring torques by exchanging its angular momentum with the satellite body. The external disturbance torque on the satellite produces angular rates and increases the angular momentum of the satellite body. This angular momentum is absorbed by the wheel during the wheel pointing modes resulting in the angular momentum of the wheel build-up over time. The RW saturates instantly as soon as its motor attains the maximum angular speed. In order to unload the RW angular momentum, a controlled external torque is required that can either be delivered by the thrusters or by the magnetorquers. The magnetorquers were selected for the mission due to their simple design, reliable operation and suitability to the CubeSat compact structure.

3.3.1 Actuator Sizing

This section illustrates the evaluation of different parameter of the reaction wheels and the magnetorquers for the mission satellite. These parameters include torqueing requirements and the momentum storage capacity for the RW and the minimum magnetic moment requirements from the magnetorquers.

Stellenbosch University https://scholar.sun.ac.za

3.3.1.1 RW Sizing

The minimum torque required for the RW is determined from the agility requirements for the mission. Assuming a bang-bang control such that the maximum wheel torque is used for the slew manoeuvre, the minimum torque required by the wheel is calculated as follows [32],

$$N_{slew} = \frac{4\theta I}{t^2} \tag{3.2}$$

where, 'I' is the MOI for the axis of slew manoeuvre and θ is the required slew angle in the specified time 't' seconds. The agility requirement for the mission, as mentioned in Section 1.2.2, is 30° in 30 seconds around the roll and the pitch axes and the largest MOI axis is taken for the torque requirements calculations,

$$N_{slew} = \frac{4(30° \times \pi/180)(0.36)}{(30)^2} = 0.838 \text{ mNm}$$

The torque requirements for the RW are now calculated as,

$$N_{wheel\_req} = N_{slew} + N_d \tag{3.3}$$

where, N_d is the worst case maximum disturbance torque calculated in Table 2-1.

$$N_{wheel\_req} = 0.843 \text{ mNm}$$

The maximum angular momentum for the slew manoeuver is calculated as follows [32],

$$h_{slew} = \frac{N_{slew} * t}{2} \tag{3.4}$$

$$= \frac{(0.838)(30)}{2} = 12.57\text{mNms}$$

In RW pointing modes the RW compensates for the disturbance torques acting on the satellite and the wheel angular momentum builds over time. In order to calculate the required momentum storage capacity for the RW, the worst case disturbance torques N_d are integrated over the sunlit part of the orbit period time [30]. The magnetorquers compensate for the disturbance torques in the eclipse and unload the accumulated angular momentum as well. Taking the cumulative worst case disturbance torque value presented in Table 2-1, the required angular momentum storage capacity for the RW is calculated as follows,

Stellenbosch University https://scholar.sun.ac.za

$$h_{wheel\_req} = h_{d\_sunlit} + h_{slew} = N_d(T_o - T_e) + h_{slew} \tag{3.5}$$

where, h_{d_sunlit} is the accumulated angular momentum during the sunlit part of the orbit, T_o is the orbital time period and T_e represents the eclipse duration of the orbit taken from Wertz [32].

$$h_{wheel\_req} = (5.78 \times 10^{-6}) * (5677.2 - 2145) + 12.57 \times 10^{-3} = 32.98 \text{ mNms}$$

3.3.1.2 Magnetorquer Sizing

The magnetorquers are sized to provide enough magnetic torque capability to dump the accumulated RW angular momentum in a specified period of time. As the mission satellite has an imaging payload and shall capture images during the sunlit part of its orbit therefore, high pointing accuracy and stability can be required at any time during the sunlit part for imaging. The magnetic torques during momentum unloading may disturb the pointing. Therefore, to be on the safe side, the momentum unloading was chosen to be done in the eclipse part of the orbit only. Consequently, the magnetorquer was sized to dump the worst case angular momentum calculated in Equation (2.26) , in a time equal to the eclipse part of the orbit. The magnetic torque required for momentum dumping over the eclipse time is given by,

$$N_{m,req} = \frac{h_d}{T_e} \tag{3.6}$$

$$= \frac{0.0328}{2145} = 15.291 \ \mu\text{Nm}$$

The minimum magnetic dipole moment that has to be generated by each magnetorquer is calculated by taking the minimum magnitude of the geomagnetic field vector (B_{min}) in the orbit [30] .

$$M_{min} = \frac{N_{m,req}}{B_{min}} \tag{3.7}$$

$$= \frac{15.291\mu}{25\mu} = 0.612 \text{ Am}^2$$

Stellenbosch University https://scholar.sun.ac.za

3.4 Magnetorquer Design

Magnetorquer rod assembly consists of a coil of copper wire usually wound on a cylindrical ferromagnetic rod that produces a magnetic dipole, when an electric current is passed through it. The torque produced by a magnetorquer depends on the strength of external magnetic field **B** and the magnetic dipole moment of the magnetorquer **M**.

$$\boldsymbol{\tau} = \mathbf{M} \times \mathbf{B} \tag{3.8}$$

The magnetic moment of a magnetorquer is calculated as follows,

$$M = \mu_{rod} nIA \tag{3.9}$$

where,

n = number of windings

I = DC current through the coil

A = enclosed area of the coil

μ_{rod} is the magnetic amplification of the ferromagnetic rod, which for a cylindrical shape rod can be calculated as follows,

$$\mu_{rod} = 1.66\left(\frac{L}{D}\right)^{1.5} \tag{3.10}$$

The term $\frac{L}{D}$ is called the shape factor of the rod. where, 'L' is the length of the rod and 'D' is the radial diameter. The DC current 'I' in Equation (3.9) can be calculated as follows,

$$I = V/R_{coil}$$

where, V is the operating voltage for the magnetorquer and R_{coil} is the total resistance of the coil wire. As a magnetorquer is an inductive load therefore it also has an S-shaped hysteresis curve. To operate the magnetorquer in the linear region of the curve, the driver circuitry for the torquer was designed such that it is capable of driving the torquer with pulse width modulated (PWM) signal, therefore the operating voltage for the magnetorquers is scalable with the PWM duty cycle. Table 3-2 lists the design parameters for the magnetorquer rod.

Stellenbosch University https://scholar.sun.ac.za

Table 3-2: Magnetorquer rod design parameters

Rod Dimensions	*L*=150 mm , *D*=6.25 mm
Magnetic Amplification	195
Total winding resistance	72 ohm
Operating voltage	2.5V~5V (scalable from PWM)
Number of windings	4000
Magnetic moment	0.83 Am^2 (for 2.5V) 1.66 Am^2 (for 5V)

In order to avoid the mutually induced currents among the rods, the X- and the Y-axis magnetorquer rods was chosen placed in a 'T' shape configuration in the satellite body. A rectangular vacuum core coil was used as the Z-axis magnetorquer. Although a magnetorquer rod can also be used along the Z-axis instead of the rectangular coil; however, the choice of a rectangular coil provides an ease of placement inside the CubeSat. Table 3-3 presents the specifications for the vacuum core magnetic coil.

Table 3-3: Magnetorquer coil design parameters

Coil Dimensions	*L*=200 mm , *W*=200 mm
Magnetic Amplification	1
Total winding resistance	65.25 ohm
Operating voltage	2.5V~5V (scalable from PWM)
Number of windings	600
Magnetic moment	0.92 Am^2 (for 2.5V) 1.84 Am^2 (for 5V)

For an operating voltage of 5V, the design of magnetorquers is capable of providing magnetic moments more than the required moments, calculated in Equation (3.7). It is due to the reason that higher magnetic moments may be required for accelerated HIL testing in the Helmholtz cage. The core material for the rods is made of Supra50 material, which is an iron-nickel soft magnetic alloy with high magnetic permeability. The core was also subjected to the heat treatment process to minimise the magnetic field remanences.

3.4.1 **Magnetic Control Electronics Design**

The magnetic control electronics board is responsible for sampling the magnetometer and sending the data readout to the OBC. Moreover, it receives the magnetorquers on-time commands from the OBC and drives the magnetorquers for the commanded time intervals.

Stellenbosch University https://scholar.sun.ac.za

3.4.1.1 Design Requirements

Envisaging the role of magnetic control board from a system level perspective, the following requirements were set before starting the design of the board:

- The design of magnetic control board shall be compatible with the CubeSat standards.
- The magnetic control board shall provide an SPI interface to communicate with the RM3000 magnetometer and an I^2C interface to communicate with the OBC.
- The magnetic control board shall contain the electronics to drive three magnetorquers and shall also contain the power and communication interfaces for 3x RW units.
- The magnetic control board software shall be responsible to perform time-slicing for magnetometer and magnetorquer operations.

3.4.1.2 Component Selection

The limited power budget and the mass-volume constraints for the CubeSat require selection of highly power efficient and integrated component packages. The component choice for the magnetic control board includes the selection of a suitable MCU and the magnetorquer driver chip. The MCU was required to have low power consumption and should provide built-in I^2C and SPI interfaces. After surveying several off-the-shelf microcontroller solutions, Atmel® picoPower series microcontroller 'ATmega168PA' was selected. According to the Atmel ® Corporation, "All picoPower devices are designed for the lowest possible power consumption from transistor design" [41]. ATmega168PA features built-in SPI, I^2C, on-chip PWM modules, two 8-bit timers and one 16 bit timer. The radiation tolerant version of the MCU is not available; however external mitigation techniques can be implied (CubeSat practice) for prevention.

An H-bridge driver chip was required to drive the magnetorquer. LV8411GR, from ON Semiconductor ® was found to be the best option due to its miniature and highly integrated package. The diver chip has 4 H-bridge channels and each channel can provide continuous output current of 400 mA. Therefore all three magnetorquers can be driven by a single LV8411GR chip.

3.4.1.3 Circuit Design

In order to generate the required magnetic moment, the magnitude and the direction of the current through the magnetorquer need to be controlled. The magnetorquer is connected

Stellenbosch University https://scholar.sun.ac.za

between the two output pins, OUT1 and OUT2, of an H-bridge channel of LV8411GR. The direction of current through the magnetorquer is controlled by the logic signals on the two input pins, IN1 and IN2, of the driver IC. A logic low signal on both of the inputs turns the magnetorquer OFF. The MCU generates a PWM signal at one of its output pins, which is routed to the logic block of each magnetorquer. The MCU also outputs a 2-bit command for each magnetorquer which is also routed to the respective logic block. The logic block routes the PWM signal to either of the H-bridge channel's inputs, IN1 or IN2, depending on the combination logic set by the 2-bit MCU command. In summary, the ON-OFF operations, the operating voltage and the polarity of all three magnetorquers are controlled by a 6-bit command (2-bits for each magnetorquer) and a PWM signal from the MCU. The designed logic circuitry to control a single magnetorquer is shown in Figure 3-7 and Table 3-4 illustrates the control logic combinations.

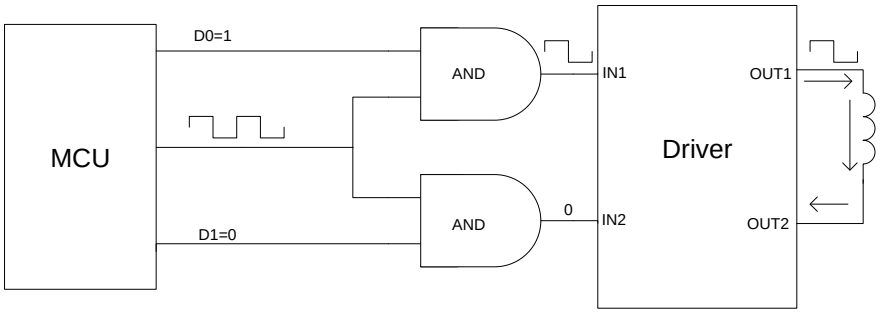

Figure 3-7: Control logic for single magnetorquer

Table 3-4 : Logic combinations for magnetic moment control

D0	D1	IN1	IN2	OUT1	OUT2	Current Flow
1	0	PWM	0	PWM	0	OUT1 to OUT2
0	1	0	PWM	0	PWM	OUT2 to OUT1
0	0	X	X	0	0	No current flow-MT OFF

The PWM signal generated by the MCU shall determine the maximum magnetic moment which a magnetorquer can generate. In order to implement the magnetic moment commands from the magnetic controllers, the on and off times for each magnetorquers shall be managed by the magnetic control board software.

Stellenbosch University https://scholar.sun.ac.za

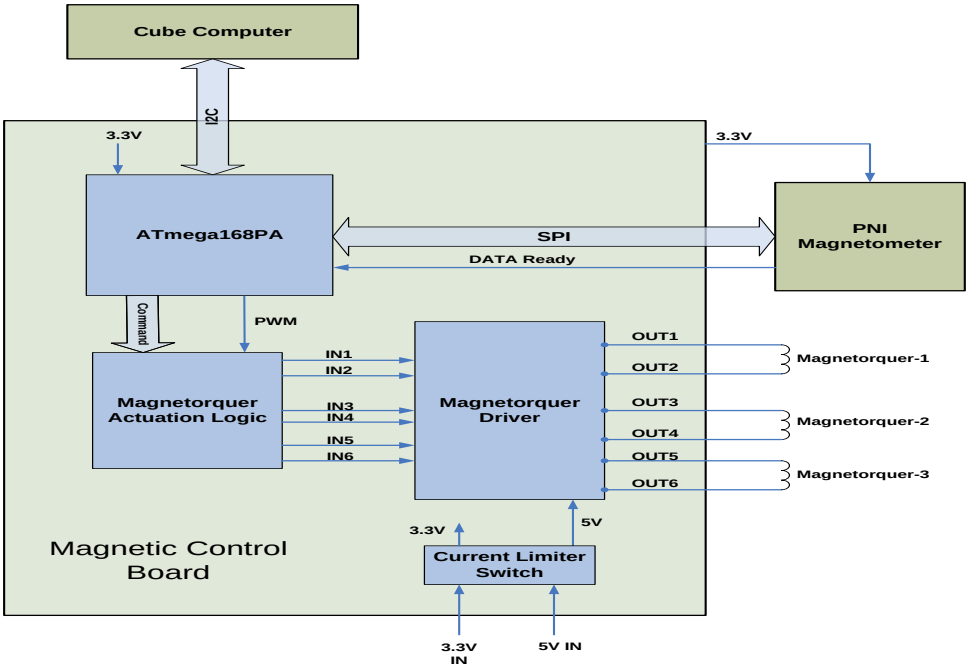

Figure 3-8: Magnetic control board layout

Figure 3-8 illustrates the layout of the magnetic control board. The interface of the magnetic control board with RM3000 magnetometer contains two power lines to provide 3.3V and ground signals to the sensor, four SPI signals and one line for the hand shaking 'data ready' signal. The magnetometer outputs 4 bytes of data for each axis measurement which is collected by the MCU upon reception of a 'data ready' signal from the magnetometer.

The magnetic control electronics also incorporates a current limiter power distribution switch, TPS2092, from Texas Instruments to switch on and switch off the power of magnetic control board. TPS2092 also provides thermal and short circuit protections and outputs a telemetry flag for an overcurrent event. The magnetic control board contains a PC-104 header to interface with the power and the OBC module in the CubeSat. The power and communication lines to the three RW units are also routed through the magnetic control board.

3.4.1.4 Magnetic Control Board Software

For a pure magnetic control case, the magnetometer measurements are required once in a magnetic control cycle, which was set to 10 seconds for this project. The software for this case was also developed and tested for magnetic controllers. However, for attitude determination using the magnetometer, the measurements are required every second for a

Stellenbosch University https://scholar.sun.ac.za

RW control period of 1 second. The basic operation of magnetic control board software for a combined operation of the RW control and the magnetic control is presented here. In this case, the magnetic control board samples the magnetometer every second and implements the commanded on-times for magnetorquers from the OBC. The OBC executes the magnetic control algorithms and update the on-times variables every 10 seconds.

The flowchart in Figure 3-9 illustrates the operation of magnetic control software. An interrupt is generated every time 'the percentage on-times' commands for magnetorquers are received from the OBC on the I^2C bus. Inside the interrupt service routine of the I^2C interrupt, the commanded on-time for each magnetorquer is saved in its respected variable as a multiple of 5 ms. For example an 80% on-time command translates to a value of 160 saved in the respected variable.

The magnetic control board software utilizes two timer blocks, one for PWM generation and the other for time slicing of the control period. The pulse width of the PWM signal determines the average operating voltage of the magnetorquers. The control period for the magnetic controllers was sliced into two portions: 80% for the magnetorquers operation and 20% for magnetometer sampling. A counter variable, CNT keeps the time record of the control period. The timer used for the time slicing generates an interrupt every 5 ms and inside its ISR, CNT is incremented by 1 every time. Moreover, inside the ISR of 5 ms timer, the variable containing the commanded on-time for each magnetorquer is compared with the CNT count value and the 6 bit ON-OFF command for the magnetorquers is updated accordingly on the IO port. When CNT count is greater than 159, which corresponds to 800 ms, all magnetorquer units are switched-off. An idle period of 50 ms (value determined from experimentation) is spent before taking the magnetometer reading. Thereafter, the magnetometer measurements are acquired and are saved in the telemetry packet.

The magnetometer data is transmitted to the OBC, when a read request is received on I^2C bus. When the CNT count value reaches 200, its value is stopped from incrementing until the next on-time command is received. The on-time command also serves as the SYNC signal for the operation. Upon reception of the on-time command, the counter variable, CNT, in the ISR of 5 ms timer is reset again and the cycle is repeated. The on-time command is transmitted to magnetic control board every second and the on-time values are updated by the OBC, once in a magnetic control cycle.

Stellenbosch University https://scholar.sun.ac.za

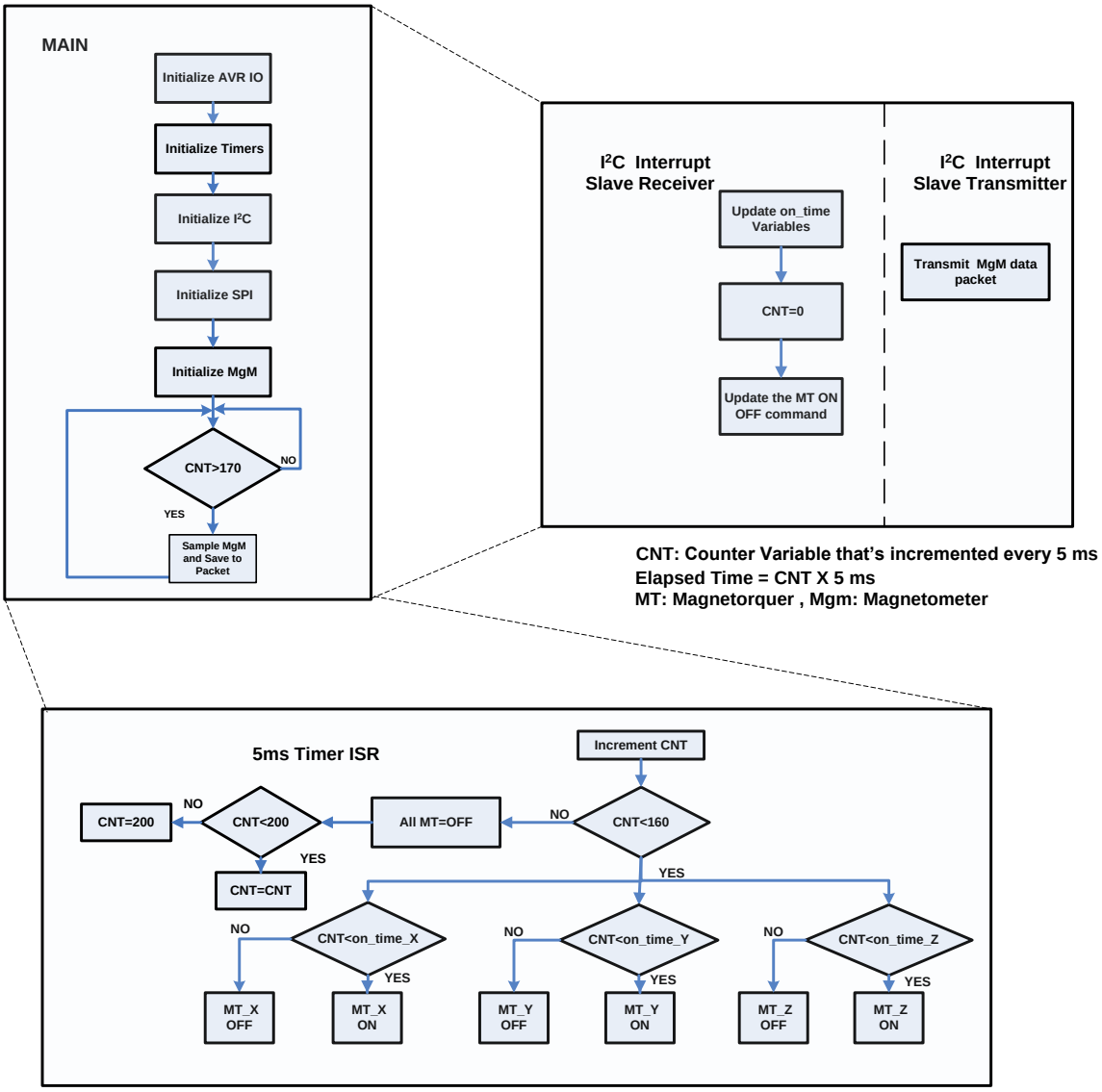

Figure 3-9 : Magnetic control software flow chart

3.5 Reaction Wheel Controller Design

The reaction wheel module consists of a DC motor with a flywheel attached to its shaft, a sensor for speed feedback and control electronics for the DC motor. 'Large CubeWheel' unit from ESL satisfies the torqueing and the momentum storage requirements for the mission determined by Equation (3.2) and Equation (3.5). It has a momentum storage capacity of 40 mNms and can deliver a maximum torque of 2.1 mNm. The mounting configuration for the RW was chosen to be the 3-wheel configuration with one wheel mounted along the each axis of the BRC frame. Previously the control electronics for the

Stellenbosch University https://scholar.sun.ac.za

'CubeWheel' was contained on the 'CubeControl' module and the RW unit only comprised of a BLDC motor with flywheel and a magnetic encoder. For this project an integrated RW electronics board was designed and developed. This board contains the electronic circuitry to drive the Brushless DC (BLDC) motor. A controller to control the flywheel speed is also implemented on this board. RW control electronics precisely control the wheel speed at the commanded reference received from the OBC and sends back the speed and the current telemetry values to the OBC.

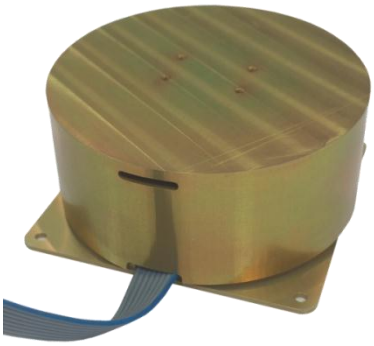

Figure 3-10: Large reaction wheel from the ESL [42]

3.5.1 **Electronics Design**

One of the design requirements for the control electronics board of 'Large CubeWheel' was that it should lend itself to be used for the 'Small CubeWheel' module as well (with slight modifications). This design requirement resulted in an area constraint for the PCB to be as small as 28 mm × 28 mm. An MCU to process the speed control algorithm and the driver for the BLDC motor were the basic components that had to be selected. The selection of components was done by taking into account the area constraint and the low power budget for a CubeSat.

CubeWheel module used a magnetic encoder for angular speed feedback. The encoder chip communicates data on an SPI interface, while the data communications with the OBC are on I^2C bus protocol. ATmega168PA-MU, which is a miniature package of the MCU used for the magnetic control board, was selected for the RW control electronics. As mentioned earlier, the MCU contains integrated SPI, I^2C and the PWM modules with highly power efficient chip design.

Stellenbosch University https://scholar.sun.ac.za

For the BLDC motor driver chip selection, a fully integrated driver package was the preliminary requirement due to the stringent area constraint. The desired BLDC driver should contain the logic and the power stage on a single ship. Moreover, the operating voltage requirement for the driver chip was in the range of 6V to 8V as the battery voltage of CubeSat bus can drop to a level of 7V during the eclipse parts of the mission orbit. After a detailed market survey; L6235 from ST Microelectronics, LB1980JH and LV8827 from On-Semiconductors were found to be the available integrated BLDC motor driver chips in the required voltage range. The performance of L6235 degrades once the operating voltage is less than 8V. The operating voltage for LB1980JH driver was 5V but it was only available in a bulk stock. Therefore, LV8827 from On-Semiconductor was selected for the RW electronics. LV8827 has a miniature package of 4 mm × 4 mm and provides direct PWM operation. In terms of the quiescent current consumption stated in the datasheets, LV8827 is more power efficient than L6235. It also demonstrated sustainable performance at operating voltages ranging from 6.75 V to 8 V during the tests.

LV8827 also features direction control and the braking option. Moreover, it contains an on-chip 5V regulator that was utilized to power up the hall sensors of the BLDC motor. The driver chip also provides a current limit feature to ensure safe operation. LV8827 driver chip includes a built-in controller to control the current through the BLDC motor coils and it was utilized to control the speed of the motor. The reference current for the control loop can be set by a PWM signal at the 'PWMIN' input of the chip and it can be varied by changing the duty cycle of the input PWM signal. The current through the motor coils can be limited through a sense resistor R_f between the RF and the ground pins of the driver chip.

The rotor of a BLDC motor is normally a permanent magnet and its stator contains the three phase windings. The driver chip generates a sequence to actuate the phases of the stator windings based on the current position of the rotor. The position of the rotor is sensed by the Hall sensors and the information is provided to the driver chip to commutate the motor. The driver chip also controls the current through the motor coils, which control the torque of the motor. The reference for the current control loop is set by the duty cycle of the PWM signal at the "PWMIN' input. The spin direction of the motor can be set by the F/R input and the motor can be stopped using the brake option by applying a logic HIGH signal on the S/S input.

Stellenbosch University https://scholar.sun.ac.za

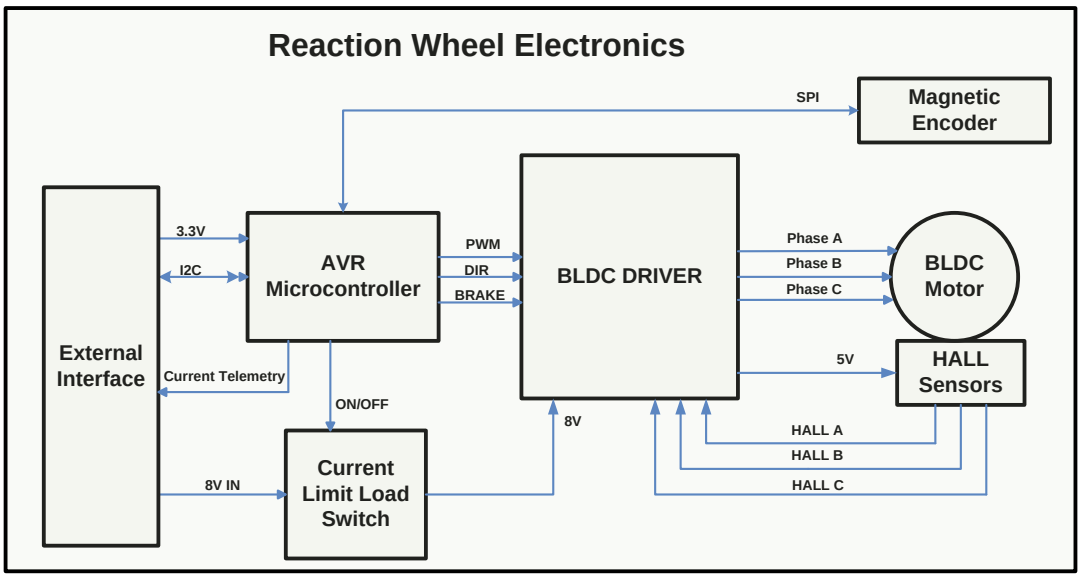

Figure 3-11: Reaction wheel drive electronics board layout

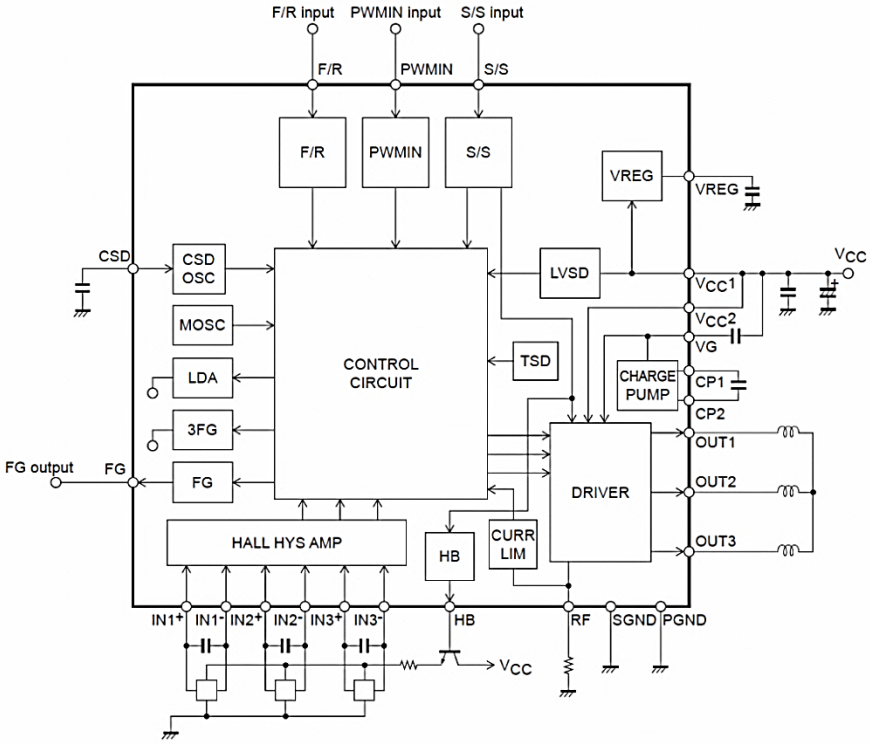

Figure 3-12: LV8827 BLDC driver architecture [43]

The maximum current for the BLDC motor was limited to 0.175 A. The value of R_f resistor required for setting this value of current is calculated from the following relation,

Stellenbosch University https://scholar.sun.ac.za

$$I_{limit} = \frac{V_{Ref}}{R_f} \tag{3.11}$$

According to the datasheet, the value of V_{Ref} ranges from 0.19V to 0.23V with a typical value of 0.21 V.

$$R_f = \frac{V_{Ref}}{I_{limit}} = \frac{0.21}{0.175} = 1.2\Omega$$

This value sets the value of current corresponding to the maximum acceleration or a 100 % duty cycle to 175mA. The value of maximum current can be scaled down in the software by limiting maximum value of the PWM signal duty cycle.

The wheel control electronics board provides an I^2C interface at its connector to communicate with the OBC and a UART interface for testing and debugging purposes. Moreover, it provides an analogue telemetry signal for the driver current as well. The interface with power subsystem contains 3.3 V, 8 V and ground lines. In order to optimize the design for minimum power usage, while fulfilling all functional requirements, the following strategies were adopted:

- The driver chip can be turned off by the MCU to save quiescent current of the driver chip and the Hall sensors during the periods when the wheel control is not active. The MCU can be put into power saving mode or sleep mode for power savings. This mode can be terminated anytime by the OBC by sending a telecommand on the I^2C bus.
- The operating voltage for the MCU was chosen to be 3.3 V as the power consumption at 5V is more than the power usage at 3.3 V.
- The specified frequency range for PWM input is from 0.5 kHz to 60 kHz. The power consumption for the driver IC is higher at lower PWM frequencies. However, at higher frequencies settings the resolution for PWM duty cycle is lower which results in lower speed control resolution. The other aspect is the current ripple that results into the torque ripple eventually. The torque ripple effects are smaller at higher PWM frequencies. An optimal value of 28.8 kHz was chosen for the PWM frequency after conducting a series of power measurement experimentations.

Stellenbosch University https://scholar.sun.ac.za

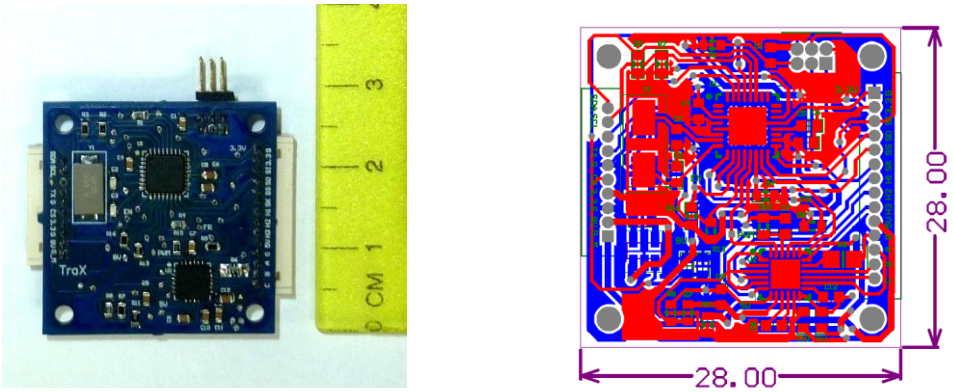

Figure 3-13 : Integrated RW electronics board

The MCU software utilizes a 16-bit timer to generate PWM signal for speed control. Another 8-bit timer was used to generate an interrupt every 5ms and inside the ISR of this 8-bit timer, the magnetic encoder data is acquired for speed calculations. As the control period for speed control is 100 ms, the encoder is sampled 20 times in one control period. The speed control algorithm is executed in the main software loop and the reference speed for the controller is updated inside the ISR of the I^2C interrupt.

3.5.2 **Encoder Noise Suppression**

In order to suppress noise from the encoder data, two low pass filtering techniques were considered. In the first technique the speed was calculated by taking the arithmetic mean of the last 5 of the 20 encoder samples each control cycle. In the second technique a discrete low pass filter (LPF) was implemented for the encoder data.

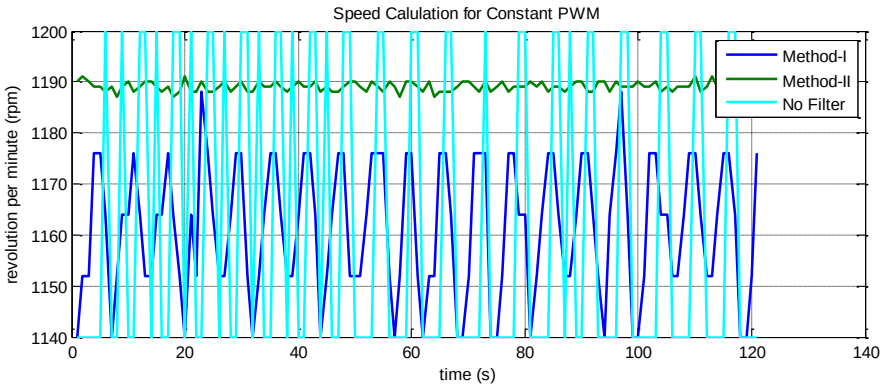

Figure 3-14: Performances of the noise suppression algorithms

The LPF method for noise filtration is described by Equation (3.12) and the value of α was chosen as 0.95 through experimentation.

Stellenbosch University https://scholar.sun.ac.za

$$y(k) = \alpha\, y(k-1) + (1-\alpha)y(k) \tag{3.12}$$

The plots shown in Figure 3-14 illustrate the performance of the two low pass filter techniques. The RW was operated in the open loop mode with constant duty cycle of the PWM input and three values for the current speed were calculated. Firstly, by using an arithmetic mean method, secondly by applying a discrete low pass filter and thirdly without using any filtration algorithm. It is evident from the plots that the LPF method has better filtering performance than the arithmetic mean method and it was therefore used for encoder noise low pass filtering.

3.5.3 **RW Speed Controller Design**

The steps followed to design the speed controller for the RW are explained in this section.

3.5.3.1 Design Requirements

The controller was designed for the following performance specifications:

- The 2% settling time for the speed controller shall be 3 seconds.
- An overdamped response with a damping ratio of 0.8 and a zero steady state error.

3.5.3.2 System Modelling

The plant model for the control system contains a BLDC motor and its driver electronics. The plant was modelled as a first order system that takes PWM counts as input and outputs an angular speed. Figure 3-15 explains different parameters of the plant model involved in getting an angular speed from a certain PWM count input.

The parameters of the model described in Figure 3-15 are evaluated as follows:

1. K_{PWM} , the PWM constant, is the relation between the PWM counts and the driver output current and is calculated from the driver chip current settings and the PWM frequency settings.

$$K_{PWM} = \frac{I_{limit}}{Max\ PWM\ Counts}$$

where, I_{limit} is the maximum current for the BLDC motor and was set to 175 mA and the maximum value for PWM counts was chosen as 346 for optimal power usage.

Stellenbosch University https://scholar.sun.ac.za

$$K_{PWM} = \frac{0.175}{346} = 5.05 * 10^{-4}\ \text{Amp/PWM Count}$$

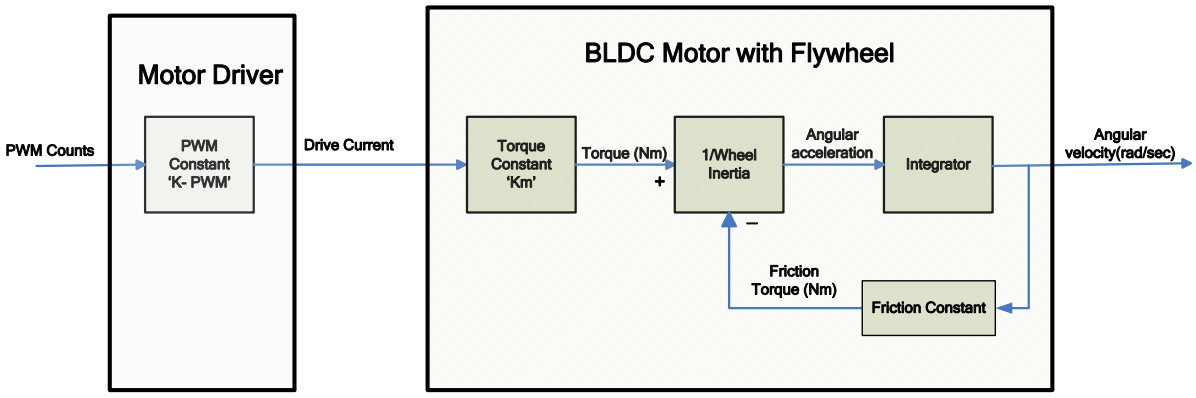

Figure 3-15: Plant model for RW system

2. K_m , the motor torque constant, is the relation between motor input current and the output torque and it is specified in the BLDC motor datasheet [44].

$$K_m = 9.05\ \text{mNm/A}$$

3. For Large CubeWheel , the inertia of the flywheel is as follows,

$$I_{wheel} = 47.3\ \text{kg} - \text{mm}^2$$

4. The dynamic friction constant for the motor is specified in the datasheet [44].

$$K_{friction} = C_v = 1.35 \times 10^{-5}\ \text{mNm/rpm}$$

5. K_T , the constant relating the PWM counts with the angular acceleration in rev / s^2, is evaluated as follows,

$$K_T = \frac{K_{PWM} * K_m}{I_{wheel} * 2\pi} = 0.0154$$

3.5.3.3 State Space System Representations

As described in the earlier section that the RW is modelled as first order system, therefore it has only one state that is the angular speed of flywheel. The state space model of the system is presented as:

Stellenbosch University https://scholar.sun.ac.za

$$\dot{x_1} = Ax_1 + B\,\mathrm{u} \tag{3.13}$$

$$y = C\,x_1 + d\,\mathrm{u} \tag{3.14}$$

where,

$\mathrm{x}_1 =$ angular velocity in revolution per second

$\mathrm{u} =$ PWM_Counts

$A = K_{friction}$

$B = K_T$

$C = 1$

$d = 0$

In discrete form,

$$\begin{aligned} x_1(k+1) &= F\,x_1(k) + g\,u(k) \\ y(k) &= C\,x_1(k) \end{aligned} \tag{3.15}$$

The continuous to discrete domain conversion was done using Matlab c2d command with a sampling time of 0.1 seconds.

3.5.3.4 State Feedback Integral Control

The performance specifications, mentioned in Section 3.5.3.1, require an integral control to attain zero steady state error. In order to add integral dynamics to the original plant described by Equation (3.15), the plant model is augmented with the integrator state and a new state $v(k)$ is added to the system [45, 46].

$$v(k+1) = v(k) + y(k+1) - r$$

As the system state x_1 is the angular speed and it is also the output of the system, therefore $y = x_1$ and

$$v(k+1) = v(k) + x_1(k+1) - r$$

From Equation (3.15),

$$v(k+1) = v(k) + [F\,x_1(k) + g\,u(k)] - r$$

Stellenbosch University https://scholar.sun.ac.za

The state space model of the system with integrator dynamics can be written as,

$$x_1(k+1) = F\,x_1(k) + g\,u(k)$$

$$v(k+1) = v(k) + F\,x_1(k) + g\,u(k) - r$$

In matrix form,

$$\begin{bmatrix} x_1(k+1) \\ v(k+1) \end{bmatrix} = \begin{bmatrix} F & 0 \\ F & 1 \end{bmatrix} \begin{bmatrix} x_1(k) \\ v(k) \end{bmatrix} + \begin{bmatrix} g \\ g \end{bmatrix} u(k) + \begin{bmatrix} 0 \\ -1 \end{bmatrix} r \tag{3.16}$$

In the steady state conditions, the next value of the state is equal to the previous value, therefore:

$$\begin{bmatrix} x_{1_{ss}} \\ v_{ss} \end{bmatrix} = \begin{bmatrix} F & 0 \\ F & 1 \end{bmatrix} \begin{bmatrix} x_{1_{ss}} \\ v_{ss} \end{bmatrix} + \begin{bmatrix} g \\ g \end{bmatrix} u_{ss} + \begin{bmatrix} 0 \\ -1 \end{bmatrix} r \tag{3.17}$$

In order to remove the presence of reference signal in the dynamic model, Equation (3.17) is subtracted from Equation (3.16) and a new augmented state $\tilde{\mathbf{x}}$ is defined such that,

$$\tilde{\mathbf{x}}(k+1) = \bar{\mathbf{F}}\tilde{\mathbf{x}}(k) + \bar{\mathbf{g}}\tilde{u}(k)$$

with,

$$\tilde{x} = \begin{bmatrix} x_1(k) - x_{1_{ss}} \\ v(k) - v_{ss} \end{bmatrix} \quad \text{and} \quad \tilde{u} = u(k) - u_{ss}$$

$$\bar{\mathbf{F}} = \begin{bmatrix} F & 0 \\ F & 1 \end{bmatrix} \qquad \text{and} \qquad \tilde{\mathbf{g}} = \begin{bmatrix} g \\ g \end{bmatrix}$$

The state feedback control law is now,

$$\tilde{u} = -\underline{\mathbf{k}}\tilde{\mathbf{x}} = -[K_p \;\; K_i]\tilde{\mathbf{x}}$$

Or

$$u(k) - u_{ss} = -[K_p \;\; K_i] \begin{bmatrix} x_1(k) - x_{1_{ss}} \\ v(k) - v_{ss} \end{bmatrix}$$

Stellenbosch University https://scholar.sun.ac.za

For steady state conditions, $\tilde{\mathbf{x}}(k+1) - \tilde{\mathbf{x}}(k) = \mathbf{0}$, therefore:

$$v(k+1) - v(k) = 0$$

This implies that

$$y(k) - r = 0 \text{ or } y(k) = r \quad [45, 46]$$

It means that the output is following the constant reference input with zero steady state error.

3.5.3.5 Controller Gains for the Desired Closed Loop Performance

The inclusion of an integrator made the original first order system model a second order system with two poles. In order to attain the desired performance specifications the positions of closed loop poles in s-plane were determined as follows,

$$\zeta = 0.8$$

For a 2% settling time of 3 seconds,

$$\omega_n = \frac{4}{\zeta * 3} = 1.667\ rad/s$$

The closed loop complex conjugate poles were,

$$s_{1,2} = -\zeta\omega_n \pm j\ \omega_n\sqrt{1-\zeta^2}$$

$$s_{1,2} = -1.33 \pm i$$

For a sampling time of $T_s = 100\ ms$, the corresponding z-plane positions were determined as follows,

$$z = e^{sT_s}$$

$$z_{1,2} = 0.8708 \pm 0.0874i$$

Finally, to determine the values of gains $-[K_p\ \ K_i]$ in order to place the closed loop poles at these locations in z-plane, Matlab command 'place' was used.

3.5.4 **RW Performance Test Results**

The responses for step inputs of 300 and 1000 RPM are plotted in Figure 3-16 and Figure 3-17 respectively. It is evident from Figure 3-16 that the 2% settling time for the step response is 3.2 seconds which is close to the designed settling time of 3 seconds. The slight differences between simulated and experimental responses in the later part of the transient

Stellenbosch University https://scholar.sun.ac.za

period is most probably due to the un-modelled frictions in the simulated model that are nonlinear and depend on the operating speed regions.

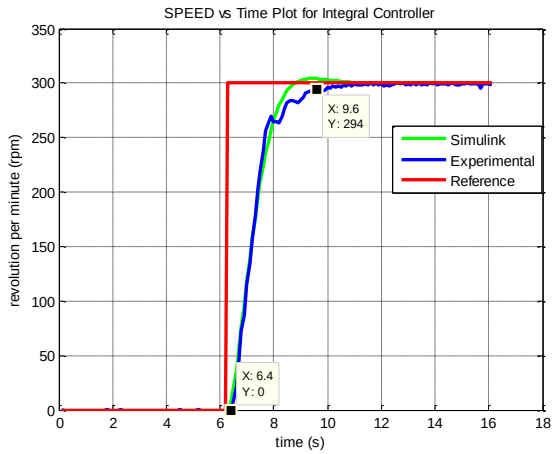

Figure 3-16 : Response to 300 RPM step command

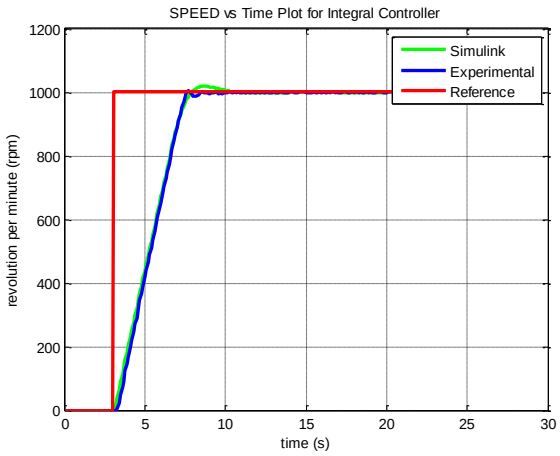

Figure 3-17: Response to 1000 RPM step command

Figure 3-18 and Figure 3-19 show the responses for ramp inputs with slopes of 10 and 20 RPM/second respectively. As the closed loop system has one free integrator term and the system is type-1, therefore, there is a constant steady state error for a ramp input.

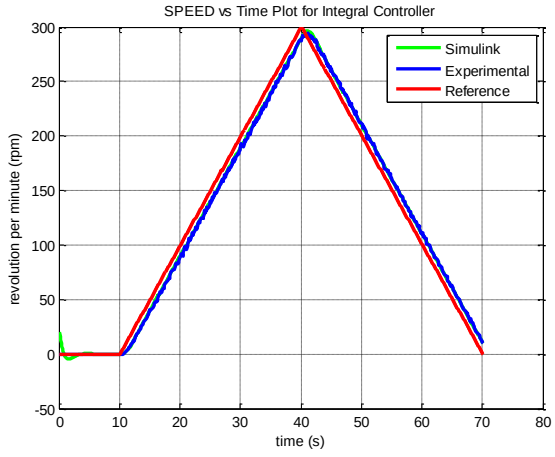

Figure 3-18: Response to a ramp input of slope 10 rpm/second

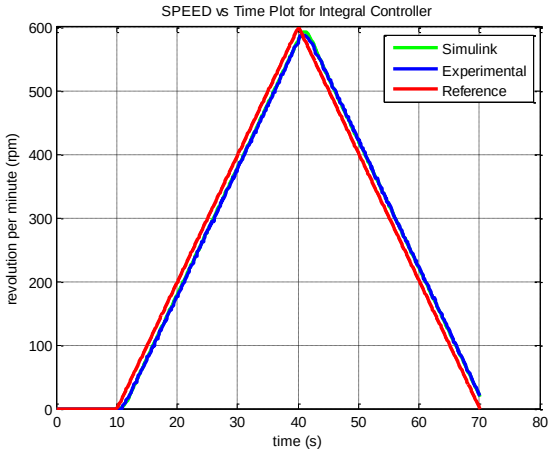

Figure 3-19: Response to a ramp input of slope 20 rpm/second

Stellenbosch University https://scholar.sun.ac.za

Table 3-5: Power consumption of large CubeWheel module for 8 V

Device	**Power Consumption**
LV8827 Driver Chip at 3000 RPM	117 mW
Driver Chip Quiescent Power at 0 RPM	35 mW
Hall Sensors Unit	55.5 mW
Atmega168PA MCU @ 3.3V	<15 mW [43]
Magnetic Encoder @ 3.3V	<5 mW [47]

The power consumption for different components of the RW module is presented in Table 3-5. If the RW control is not activated, all the units except the MCU and the magnetic encoder can be switched-off through a telecommand. In this case, the RW can operate in low power stand-by mode with a power usage of less than 20 mW.

3.6 Summary

The choice of ADCS sensors and actuators for the mission was discussed in this chapter. The ADCS sensors were selected according to the attitude knowledge requirements for the mission, which were derived from the pointing accuracy requirements. The RM3000 magnetometer, the CubeStar nano star tracker, the CubeSense integrated FSS and horizon sensor module were selected for the mission. The actuators for the mission included RW and magnetorquers. The RW was sized according to the agility and momentum storage requirements for the mission. The magnetorquer was sized to unload the worst case accumulated angular momentum of the wheel in a time equal to the eclipse period of the orbit. The ADCS hardware design included design of two printed circuit boards, namely, the magnetic control board and the reaction wheel control electronics. The magnetic control board was designed to interface with the magnetometer and drive the magnetorquers. The RW control electronics for the large CubeWheel was designed, developed and tested successfully.

Stellenbosch University https://scholar.sun.ac.za

4. THE ADCS Algorithms

The algorithms used for the orientation control of a satellite in its orbit are categorized into two sections: the attitude determination algorithms and the attitude control algorithms. The attitude determination algorithms use the attitude sensors output vectors and their corresponding modelled vectors in the reference frame to determine the attitude of the satellite relative to the reference frame. The OBC contains the mathematical models to propagate the position information of the satellite in its orbit, which is then used by the sun model and the earth magnetic field model to output the current position vector of the sun and the instantaneous magnetic field vector respectively. The vectors generated by these models serve as the reference vectors or the modelled vector in the attitude determination algorithms. Ranging from simple geometric techniques to some complex non-linear methods, numerous attitude determination algorithms exist in the satellite industry. However, this chapter will only discuss a few of these algorithms which were used for the mission satellite ADCS. The derivations and the implementation methods of these algorithms are also presented.

The attitude control section of the ADCS algorithms is comprised of a set of control laws, which command the actuators to orient the satellite according to the reference attitude command. The algorithms for satellite body rate damping and for attitude stabilization are also part of this section. As described in chapter 3, the actuators for the mission ADCS include magnetorquers and the reaction wheels, therefore the attitude control algorithms described in this chapter include both the magnetic controllers and the RW controllers. The derivations of the ADCS algorithms in this chapter are based on the Advanced ADCS Course material [48] at SU, unless referenced otherwise.

4.1 Attitude Determination

The attitude determination methods discussed in this section include the TRIAD estimation method, a Rate Kalman Filter (RKF) and a full state Extended Kalman Filter (EKF).

Stellenbosch University https://scholar.sun.ac.za

4.1.1 **TRIAD Estimator**

The TRIAD estimator is a simple geometric solution for attitude determination problem. In order to estimate the orientation of one reference frame with respect to the other, the TRIAD method requires components of two vector pairs represented in the two reference frames. For the satellite attitude determination using the TRIAD method, two measured vectors in the BRC frame and their respective modelled vectors in the ORC frame are used to calculate a DCM. This DCM describes the orientation of the BRC frame relative to the ORC frame, or in other words the attitude of the satellite [49].

4.1.1.1 TRIAD Implementation

The first step to implement the TRIAD estimator is to construct two triads of orthogonal unit vectors. The first triad is constructed from two different measured vectors in BRC frame. Let $\mathbf{b}_1$ and $\mathbf{b}_2$ be the two vectors measured by two attitude sensors then the first triad of unit vectors $\mathbf{m}_1$, $\mathbf{m}_2$ and $\mathbf{m}_3$ is determined as follows,

$$\mathbf{m}_1 = \frac{\mathbf{b}_1}{\|\mathbf{b}_1\|} \tag{4.1}$$

$$\mathbf{m}_2 = \frac{\mathbf{b}_1 \times \mathbf{b}_2}{\|\mathbf{b}_1 \times \mathbf{b}_2\|} \tag{4.2}$$

$$\mathbf{m}_3 = \mathbf{m}_1 \times \mathbf{m}_2 \tag{4.3}$$

The vector $\mathbf{b}_1$ that is used to calculate the first unit vector $\mathbf{m}_1$ in the triad is referred as the anchor vector. For better estimation accuracy, the output vector of the more accurate sensor should be chosen as the anchor [50]. The second triad of unit vectors $\mathbf{r}_1$, $\mathbf{r}_2$ and $\mathbf{r}_3$, is formed by two reference vectors $\mathbf{o}_1$ and $\mathbf{o}_2$, which are in fact the model vectors in the ORC corresponding to $\mathbf{b}_1$and $\mathbf{b}_2$ respectively.

$$\mathbf{r}_1 = \frac{\mathbf{o}_1}{\|\mathbf{o}_1\|} \tag{4.4}$$

$$\mathbf{r}_2 = \frac{\mathbf{o}_1 \times \mathbf{o}_2}{\|\mathbf{o}_1 \times \mathbf{o}_2\|} \tag{4.5}$$

$$\mathbf{r}_3 = \mathbf{r}_1 \times \mathbf{r}_2 \tag{4.6}$$

Stellenbosch University https://scholar.sun.ac.za

In the second step of the TRIAD implementation, the estimated DCM **C** is calculated from the two triads formed in the preceding step. Finally, the elements of the DCM **C** are then used to find the current estimated quaternion $\hat{\mathbf{q}}$.

$$\mathbf{C} = \mathbf{m}_1\mathbf{r}_1^{\mathrm{T}} + \mathbf{m}_2\mathbf{r}_2^{\mathrm{T}} + \mathbf{m}_3\mathbf{r}_3^{\mathrm{T}} \tag{4.7}$$

The Triad estimator is easy to implement and computationally less expensive, but its outputs are noisy for noisy sensor measurements.

4.1.2 **Rate Kalman Filter**

The Kalman Filter (KF) is an optimal recursive estimator that provides optimal estimates of the states of a process based on potentially noisy measurement data taken over a period of time [51, 52]. The filter was first described by Rudolf E. Kalman in 1960 and is still a useful tool, particularly in the navigation and aerospace industry.

During the detumbling phase of a satellite mission, the power budget is very limited as the satellite has still to acquire the sun for power generation. In order to save the power, the angular rate information during the de-tumbling phase of the mission satellite was taken from the RKF rather using the gyro rates. The RKF implemented for the project provides 3-axis angular rate estimates based on the magnetometer measurements.

Similar to a general KF structure, the RKF also consists of a linearized system model and a measurement model. The system model comprises of the equations, which describe the dynamics of the system and is used to propagate the states being estimated. The measurement model is the relation between the measurements and the estimated states. The general form of a time domain linear system model is given as follows,

$$\dot{\mathbf{x}}_t = \mathbf{F}_t\mathbf{x}_t + \mathbf{G}_t\mathbf{u}_t + \mathbf{s}_t \tag{4.8}$$

Similarly, the measurement model is written in the general form as,

$$\mathbf{y}_t = \mathbf{H}_t\mathbf{x}_t + \mathbf{m}_t \tag{4.9}$$

where, $\mathbf{x}_t$ in the system model expression designates the state vector , $\mathbf{u}_t$ is the input vector and $\mathbf{s}_t$ describes the process noise or the system noise. Similarly, $\mathbf{y}_t$ is the measurement output from the sensors and $\mathbf{m}_t$ refers to the sensor noise. The noise characteristics in the KF models is zero mean with Gaussian distribution.

Stellenbosch University https://scholar.sun.ac.za

4.1.2.1 RKF System Model

The Euler dynamics equation, expressed in Equation (2.12), is used as system model in RKF and the inertial referenced angular rates of the satellite are the system states to be estimated. As the RKF was used during the rate damping modes with magnetic control, therefore the control torques in Equation (2.12) only included the torques from the magnetorquers. The effect of disturbances and the gyroscopic torques in Equation (2.12) were taken as system noise.

$$\dot{\boldsymbol{\omega}}_B^I = \mathbf{J}^{-1}(\mathbf{N}_{\mathrm{m}t}) + \mathbf{J}^{-1}(\mathbf{N}_{\mathrm{D}t} - \mathbf{N}_{\mathrm{GYRO}-t}) \tag{4.10}$$

where, $\mathbf{J}$ is the inertia tensor matrix of the satellite. The RKF system model in continuous domain is described as follows,

$$\dot{\mathbf{x}}_t = \mathbf{G}_t\mathbf{u}_t + \mathbf{s}_t$$

where, $\mathbf{G}_t = \mathbf{J}^{-1}$, $\mathbf{u}_t = \mathbf{N}_{\mathrm{m}t}$ and $\mathbf{s}_t = \mathbf{J}^{-1}(\mathbf{N}_{\mathrm{D}t} - \mathbf{N}_{\mathrm{GYRO}-t})$

The equivalent discrete domain system model was obtained from the continuous domain model as follows,

$$\mathbf{x}(k+1) = \boldsymbol{\Phi}\,\mathbf{x}(k) + \boldsymbol{\Gamma}\mathbf{u}(k) + \mathbf{s}(k) \tag{4.11}$$

If ΔT be the sampling time of the discrete filter,

$$\boldsymbol{\Phi} = \boldsymbol{e}^{\Delta T[\mathbf{F}_t]_{t=k\Delta T}} = \mathbf{I}_{3\times 3} \qquad \text{(identity matrix)}$$

$$\boldsymbol{\Gamma} \cong \Delta T[\mathbf{G}_t]_{t=k\Delta T} = \Delta T\,\mathbf{J}^{-1}$$

$$\mathbf{u}(k) = [\mathbf{N}_m]_{t=k\Delta T}$$

$$\mathbf{s}\,(k) = [\mathbf{s}_t]_{t=k\Delta T} = \mathrm{N}\{\mathbf{0}, \mathbf{Q}(k)\}$$

The matrix $\mathbf{Q}$ is a diagonal matrix of order 3×3 referred as the system noise covariance matrix.

4.1.2.2 RKF Measurement Model

In order to determine the measurement model of the RKF, it was assumed that the orbit referenced body rates are approximately equal to the inertial rates i.e. $\boldsymbol{\omega}_{BO} \cong \boldsymbol{\omega}_{BI}$. Secondly, it was assumed that the orbit rates stay almost constant between successive

Stellenbosch University https://scholar.sun.ac.za

sampling instants. In this case, the change in the Euler angles at sampling instant 'k' can be approximated as,

$$(\Delta\phi)_k \approx \Delta T(\omega_{xi})_k\,, (\Delta\theta)_k \approx \Delta T\left(\omega_{yi}\right)_k\,, (\Delta\psi)_k \approx \Delta T(\omega_{zi})_k \tag{4.12}$$

For a small angle rotation (θ), $\theta \approx 0 \rightarrow \sin\theta \approx \theta$ and $\cos\theta \approx 1$, therefore the rotation matrix described by Equation (2.1) can be approximated for small rotations $(\theta, \emptyset, \psi)$ as follows,

$$\mathbf{C} \approx \begin{bmatrix} 1 & \psi & -\theta \\ -\psi & 1 & \phi \\ \theta & -\phi & 1 \end{bmatrix}$$

Let $(\Delta\mathbf{A})_k$ be the DCM representing the change in attitude between the successive sampling instants $k-1$ and k. Applying the small angle approximation to $(\Delta\mathbf{A})_k$, the DCM matrix can be written as follows,

$$(\Delta\mathbf{A})_k \approx \begin{bmatrix} 1 & (\Delta\psi)_k & -(\Delta\theta)_k \\ -(\Delta\psi)_k & 1 & (\Delta\phi)_k \\ (\Delta\theta)_k & -(\Delta\phi)_k & 1 \end{bmatrix}$$

From the relations expressed in Equation (4.12),

$$(\Delta\mathbf{A})_k \approx \begin{bmatrix} 1 & \Delta T(\omega_{zi})_k & -\Delta T(\omega_{yi})_k \\ -\Delta T(\omega_{zi})_k & 1 & \Delta T(\omega_{xi})_k \\ \Delta T(\omega_{yi})_k & -\Delta T(\omega_{xi})_k & 1 \end{bmatrix} \tag{4.13}$$

If the previous measurement of an inertially fixed unit vector in the BRC frame is $\mathbf{v}_{k-1}$, then the value of the measurement at the next sampling instant can be predicted as,

$$\mathbf{v}_k = (\Delta\mathbf{A})_k\mathbf{v}_{k-1} \tag{4.14}$$

The change in the unit vector measurements between two sampling instants can be written as,

$$\begin{aligned} \Delta\mathbf{v}_k &= \mathbf{v}_k - \mathbf{v}_{k-1} \\ &= (\Delta\mathbf{A})_k\mathbf{v}_{k-1} - \mathbf{v}_{k-1} \\ &= [(\Delta\mathbf{A})_k - \mathbf{I}]\mathbf{v}_{k-1} \end{aligned} \tag{4.15}$$

Stellenbosch University https://scholar.sun.ac.za

$$= \begin{bmatrix} 0 & \Delta T(\omega_{zi})_k & -\Delta T(\omega_{yi})_k \\ -\Delta T(\omega_{zi})_k & 0 & \Delta T(\omega_{xi})_k \\ \Delta T(\omega_{yi})_k & -\Delta T(\omega_{xi})_k & 0 \end{bmatrix} \mathbf{v}_{k-1} \tag{4.16}$$

From the matrix-vector multiplication properties, Equation (4.16) can be rewritten as,

$$\Delta \mathbf{v}_k = \begin{bmatrix} 0 & \Delta T(v_z)_k & -\Delta T(v_y)_k \\ -\Delta T(v_z)_k & 0 & \Delta T(v_x)_k \\ \Delta T(v_y)_k & -\Delta T(v_x)_k & 0 \end{bmatrix} \begin{bmatrix} \omega_{xi} \\ \omega_{yi} \\ \omega_{zi} \end{bmatrix} \tag{4.17}$$

The measurement output at sampling instant k is,

$$\mathbf{y}_k = \Delta \mathbf{v}_k$$

The measurement model in its general form can now be written as,

$$\mathbf{y}_k = \mathbf{H}_k \, \mathbf{x}_k + \mathbf{m}_k$$

$$= \begin{bmatrix} 0 & \Delta T(v_z)_k & -\Delta T(v_y)_k \\ -\Delta T(v_z)_k & 0 & \Delta T(v_x)_k \\ \Delta T(v_y)_k & -\Delta T(v_x)_k & 0 \end{bmatrix} \begin{bmatrix} \omega_{xi} \\ \omega_{yi} \\ \omega_{zi} \end{bmatrix} + \mathbf{m}_k \tag{4.18}$$

where, $\mathbf{m}_k$ is the discrete measurement noise with zero mean and covariance matrix **R,** which is a diagonal matrix of order 3×3 , referred as the measurement noise covariance matrix.

4.1.2.3 RKF Implementation

The RKF algorithm was implemented as a sequence of five steps, involving mathematical calculations, which was repeated every sampling instant. These steps are divided into two sections; state propagation (model update) and the state correction (measurement update). During the propagation step, the states $\hat{\mathbf{x}}_k$ (the angular rates) and the state covariance matrix $\mathbf{P}_k$ are propagated based on the system model (linearized Euler dynamics equations). After acquiring measurement data, during the measurement update step, the output matrix $\mathbf{H}_k$ is updated and the Kalman gains are calculated. Afterwards, the propagated states and the state covariance matrix are corrected based on the new Kalman gain and the output matrix. The subscript $(k+1/k)$ used in the following steps means that the variable is determined at the sampling instant $k+1$, using the measurement information up to the sampling instant k.

Stellenbosch University https://scholar.sun.ac.za

4.1.2.3.1 Model Update

1. Propagate the state vector by performing numerical integration (modified Euler integration) of the non-linear dynamics model

$$\hat{\mathbf{x}}_{k+1/k} = \hat{\mathbf{x}}_{k/k} + 0.5\Delta T(3\Delta\mathbf{x}_k - \Delta\mathbf{x}_{k-1}) \tag{4.19}$$

$$\Delta\mathbf{x}_k = \mathbf{J}^{-1}(\mathbf{N}_{m,k} - \mathbf{N}_{GYRO,k})$$

2. Propagate the state covariance matrix

$$\mathbf{P}_{k+1/k} = \mathbf{\Phi}_k\mathbf{P}_{k/k}\mathbf{\Phi}_k^T + \mathbf{Q} \tag{4.20}$$

Before performing the measurement update the measurement data is acquired, which in this case is the magnetometer readout. Moreover, the geomagnetic field vector given by the magnetometer is normalized before using in the RKF.

4.1.2.3.2 Measurement Update

3. Compute the output matrix $\mathbf{H}_{k+1}$ as described in Equation (4.18) and update the Kalman gain

$$\mathbf{K}_{k+1} = \mathbf{P}_{k+1/k}\mathbf{H}_{k+1}^T[\mathbf{H}_{k+1}\mathbf{P}_{k+1}\mathbf{H}_{k+1}^T + \mathbf{R}]^{-1} \tag{4.21}$$

4. Update the state vector using the updated $\mathbf{H}_{k+1}$ matrix and the Kalman gain $\mathbf{K}_{k+1}$

$$\hat{\mathbf{x}}_{k+1/k+1} = \hat{\mathbf{x}}_{k/k} + \mathbf{K}_{k+1}[y_{k+1} - \mathbf{H}_{k+1}\hat{\mathbf{x}}_{k+1/k}] \tag{4.22}$$

5. Update the state covariance matrix

$$\mathbf{P}_{k+1/k+1} = [\mathbf{I}_{3\times3} - \mathbf{K}_{k+1}\mathbf{H}_{k+1}]\mathbf{P}_{k+1/k} \tag{4.23}$$

4.1.3 **Extended Kalman Filter**

A full state EKF was used in the mission ADCS, to estimate the current quaternions and the inertial body rates. The EKF is a variation of the KF, which is particularly useful in the state estimation of non-linear systems. Due to the nonlinear nature of satellite dynamics and kinematics, an EKF is widely used for satellite attitude determination. The EKF utilizes the nonlinear system model and linearizes it around the point where the true state is equal to the

Stellenbosch University https://scholar.sun.ac.za

estimated state. The state vector for the full state EKF has seven elements and is given as follows,

$$\mathbf{x} = \begin{bmatrix} \boldsymbol{\omega}_{BI} \\ \mathbf{q} \end{bmatrix} \tag{4.24}$$

4.1.3.1 System Perturbation Model

The general form of an EKF system model with non-linear dynamics is as follows,

$$\dot{\mathbf{x}_t} = \mathbf{f}\{\mathbf{x}_t, t\} + \mathbf{s}_t \tag{4.25}$$

where, $\mathbf{s}_t$ represents the system noise vector with zero mean and the covariance matrix $\mathbf{Q}$.

$$\mathbf{s}_t = \mathbf{N}\{\mathbf{0}, \mathbf{Q}(\mathrm{t})\} \tag{4.26}$$

A perturbation state vector $\delta\mathbf{x}$ is defined as the difference between the true state vector $\mathbf{x}_t$ and the estimated state vector $\hat{\mathbf{x}}_t$.

$$\delta\mathbf{x}_t \triangleq \mathbf{x}_t - \hat{\mathbf{x}}_t \tag{4.27}$$

The system model given by Equation (4.25) is linearized around the estimated state by using first order Taylor series expansion.

$$\mathbf{f}\{\mathbf{x}_t, t\} \approx \mathbf{f}\{\hat{\mathbf{x}}_t, t\} + \mathbf{F}_t\, \delta\mathbf{x}_t \tag{4.28}$$

with , $$\mathbf{F}_t = \left[\frac{\partial \mathbf{f}}{\partial \mathbf{x}}\right]_{\mathbf{x}_t = \hat{\mathbf{x}}_t}$$

Differentiating Equation (4.27) results,

$$\delta\dot{\mathbf{x}}_t = \dot{\mathbf{x}}_t - \dot{\hat{\mathbf{x}}}_t$$

Replacing $\dot{\mathbf{x}_t}$ in the above equation with the relation, given by Equation (4.25)

$$\delta\dot{\mathbf{x}}_t = \mathbf{f}\{\mathbf{x}_t, t\} + \mathbf{s}_t - \mathbf{f}\{\dot{\hat{\mathbf{x}}}_t, t\}$$

From Equation (4.27) and (4.28), the linearized perturbation model can now be written as,

$$\delta\dot{\mathbf{x}}_t = \mathbf{F}_t\delta\mathbf{x}_t + \mathbf{s}_t \tag{4.29}$$

Stellenbosch University https://scholar.sun.ac.za

$\mathbf{F}_t$ is the Jacobian matrix and the derivation of this matrix in terms of state variables is presented in Appendix A. In order to implement a discrete EKF, $\mathbf{F}_t$ is discretized to get the discrete state perturbation matrix $\mathbf{\Phi}_k$

$$\mathbf{\Phi}_k = [e^{\Delta T \mathbf{F}_t}]_{\mathbf{x}_t=\hat{\mathbf{x}}_t, t=k\Delta T} \tag{4.30}$$

As the values of the elements of $\mathbf{F}_t$ matrix are small quantities (see Appendix A) therefore $\mathbf{\Phi}_k$ can be approximated by a second order Taylor series expansion.

$$\mathbf{\Phi}_k \approx [\mathbf{I}_{7\times7} + \Delta T \mathbf{F}_t + \frac{1}{2}\Delta T^2 \mathbf{F}_t^2] \tag{4.31}$$

The system perturbation model in discrete domain can now be written as,

$$\delta\mathbf{x}_{k+1} = \mathbf{\Phi}_k \delta\mathbf{x}_k \tag{4.32}$$

4.1.3.2 Measurement Perturbation Model

The non-linear measurement model for the EKF, in discrete domain, can be expressed in its general form as follows,

$$\mathbf{y}_k = \mathbf{h}\{\mathbf{x}_{t_k}, t_k\} + \mathbf{m}_k \tag{4.33}$$

where, $\mathbf{m}_k$ refers to the measurement noise, which is Gaussian distributed with zero mean and the covariance matrix $\mathbf{R}_k$.

$$\mathbf{m}_k = \mathbf{N}\{\mathbf{0}, \mathbf{R}_k\}$$

The measurement model is linearized by applying the same method as used for the system perturbation model.

$$\mathbf{h}\{\mathbf{x}_k, t_k\} \approx \mathbf{h}\{\hat{\mathbf{x}}_{t_k}, t_k\} + \mathbf{H}_k\, \delta\mathbf{x}_k \tag{4.34}$$

with,

$$\mathbf{H}_k = \left[\frac{\partial \mathbf{h}}{\partial \mathbf{x}}\right]_{\mathbf{x}_t=\hat{\mathbf{x}}_t}$$

The linearized perturbation output model, also known as, innovation error model can be derived as follows,

Stellenbosch University https://scholar.sun.ac.za

$$\begin{aligned}\mathbf{e}_k &= \mathbf{y}_k - \hat{\mathbf{y}}_k \\ &= \mathbf{h}\{\mathbf{x}_{t_k}, t_k\} + \mathbf{m}_k - \mathbf{h}\{\hat{\mathbf{x}}_{t_k}, t_k\} && \text{from Equation (4.33)} \\ &\approx \mathbf{h}\{\hat{\mathbf{x}}_{t_k}, t_k\} + \mathbf{H}_k\, \delta\mathbf{x}_k + \mathbf{m}_k - \mathbf{h}\{\hat{\mathbf{x}}_{t_k}, t_k\} && \text{from Equation (4.34)} \\ &\approx \mathbf{H}_k\, \delta\mathbf{x}_k + \mathbf{m}_k \end{aligned} \tag{4.35}$$

4.1.3.3 Innovation Computation

In case of the EKF implemented for the satellite ADCS, the vector difference between the normalized measured vector in the BRC frame and its corresponding modelled vector transformed to the BRC is referred as the innovation. The measured vector also contains the measurement noise and is obtained from the sensor measurement. The ideal modelled vector in the ORC frame is free of noise and is transformed to the BRC frame by multiplying it with the current DCM $\mathbf{A}_k$.

$$\left[\bar{\mathbf{v}}_{meas,k}\right]_{ideal} = \mathbf{A}_k\{\mathbf{q}_k\}\bar{\mathbf{v}}_{model,k} \tag{4.36}$$

However, a more realistic model includes the noise effects in both the measurement and the modelled vectors and uses the estimated quaternions to evaluate the DCM $\mathbf{A}_k$.

Let $\bar{\mathbf{v}}_{model,k}$ be the ideal or true modelled vector in the ORC and the transformation of this vector in the BRC frame is represented by $\bar{\mathbf{v}}_{meas,k}$. Including the model noise $\mathbf{m}_{model,k}$ and the measurement noise $\mathbf{m}_{meas,k}$ in the two vectors,

$$\bar{\mathbf{v}}_{meas,k} - \mathbf{m}_{meas,k} = \mathbf{A}_k\{\hat{\mathbf{q}}_k + \delta\mathbf{q}_k\}(\bar{\mathbf{v}}_{model,k} - \mathbf{m}_{model,k}) \tag{4.37}$$

The perturbation quaternions vector $\delta\mathbf{q}_k$ in Equation (4.37) is the difference between the true quaternions $\mathbf{q}_k$ and the estimated quaternions $\hat{\mathbf{q}}_k$. The estimated DCM is linearized about the point $\mathbf{q}_k = \hat{\mathbf{q}}_k$ as follows,

$$\mathbf{A}_k\{\hat{\mathbf{q}}_k + \delta\mathbf{q}_k\} \approx \mathbf{A}_k\{\hat{\mathbf{q}}_k\} + \sum_{i=1}^{4}\left[\frac{\partial\mathbf{A}\{\hat{\mathbf{q}}_k\}}{\partial\mathbf{q}_i}\right]_{\mathbf{q}_k=\hat{q}_k}\delta\mathbf{q}_{i,k} \tag{4.38}$$

If the measured output $\mathbf{y}_k$ is $\mathbf{v}_{meas,k}$ then the innovation error model described in Equation (4.35) can be written as,

Stellenbosch University https://scholar.sun.ac.za

$$
\begin{aligned}
\mathbf{e}_k &= \mathbf{v}_{meas,k} - \hat{\mathbf{v}}_{meas,k} \\
&= \mathbf{v}_{meas,k} - \mathbf{A}_k\{\hat{\mathbf{q}}_k\}\bar{\mathbf{v}}_{model,k} \\
&= \mathbf{A}_k\{\hat{\mathbf{q}}_k + \delta\mathbf{q}_k\}\bar{\mathbf{v}}_{model,k} + \mathbf{m}_k - \mathbf{A}_k\{\hat{\mathbf{q}}_k\}\bar{\mathbf{v}}_{model,k} \\
&= \left[\mathbf{A}_k\{\hat{\mathbf{q}}_k\} + \sum_{i=1}^{4}\left[\frac{\partial\mathbf{A}\{\hat{\mathbf{q}}_k\}}{\partial\mathbf{q}_i}\right]_{\mathbf{q}_k=\hat{q}_k}\delta\mathbf{q}_{i,k}\right]\bar{\mathbf{v}}_{model,k} - \mathbf{A}_k\{\hat{\mathbf{q}}_k\}\bar{\mathbf{v}}_{model,k} + \mathbf{m}_k \\
&= \left[\sum_{i=1}^{4}\left[\frac{\partial\mathbf{A}\{\hat{\mathbf{q}}_k\}}{\partial\mathbf{q}_i}\right]_{\mathbf{q}_k=\hat{q}_k}\delta\mathbf{q}_{i,k}\right]\bar{\mathbf{v}}_{model,k} + \mathbf{m}_k \\
&= [\mathbf{h_1} \quad \mathbf{h_2} \quad \mathbf{h_3} \quad \mathbf{h_4}]\delta\mathbf{q}_k + \mathbf{m}_k \\
&= [\mathbf{0_{3\times3}} \quad \mathbf{h_1} \quad \mathbf{h_2} \quad \mathbf{h_3} \quad \mathbf{h_4}]\delta\mathbf{x}_k + \mathbf{m}_k \\
&= \mathbf{H}\{\hat{\mathbf{q}}_k, \bar{\mathbf{v}}_{model,k}\}\delta\mathbf{x}_k + \mathbf{m}_k
\end{aligned}
\tag{4.39}
$$

with,

$$
\mathbf{h}_i = \frac{\partial\mathbf{A}\{\hat{\mathbf{q}}_k\}}{\partial\mathbf{q}_i}\bar{\mathbf{v}}_{model,k} \qquad \text{for } i = 1,2,3,4
$$

and

$$
\mathbf{m}_k \approx \mathbf{m}_{meas,k} - \mathbf{A}_k\{\hat{\mathbf{q}}_k\}\mathbf{m}_{model,k} \tag{4.40}
$$

4.1.3.4 The EKF Implementation

Similar to the KF implementation, the EKF algorithm also consists of the model update or prediction step and the measurement update, also called correction step. The model update propagates the state vector using non-linear system equation and predicts the state perturbation covariance matrix. The measurement update then corrects the propagated state vector and the state covariance matrix based on the measurements. The subscript convention in the EKF algorithm is the same as used for the RKF algorithm.

Model Update

1. Propagate the inertial angular rates by numerically integrating the Euler dynamic equation and then calculate the quaternions using the following equation

$$
\hat{\boldsymbol{q}}_{k/k-1} = \left[\cos(k_q)\,\mathbf{I}_{3\times3} + \frac{1}{\left\|(\hat{\boldsymbol{\omega}}_{BO})_{k/k-1}\right\|}\sin(k_q)\,\boldsymbol{\Omega}_{k/k-1}\right]\hat{\mathbf{q}}_{k-1} \tag{4.41}
$$

Stellenbosch University https://scholar.sun.ac.za

with, $k_q = \frac{\Delta T}{2}\left\|(\hat{\boldsymbol{\omega}}_{BO})_{k/k-1}\right\|$ and $(\hat{\boldsymbol{\omega}}_{BO})_{k/k-1} = (\hat{\boldsymbol{\omega}}_{BI})_{k/k-1} - \hat{\mathbf{A}}_k[0\ -(\omega_o)_k\ 0]^T$

2. Propagate the perturbation covariance matrix

$$\mathbf{P}_{k+1/k} = \boldsymbol{\Phi}_{k+1/k}\mathbf{P}_{k/k}\boldsymbol{\Phi}^T + \mathbf{Q}_k \tag{4.42}$$

Measurement Update

3. Update the EKF gain using the respective **R** matrix of the measurement sensors

$$\mathbf{K}_{k+1} = \mathbf{P}_{k+1/k}\mathbf{H}^T_{k+1/k}[\mathbf{H}_{k+1/k}\mathbf{P}_{k+1/k}\mathbf{H}^T_{k+1/k} + \mathbf{R}]^{-\mathbf{1}} \tag{4.43}$$

4. Obtain the innovation

$$\mathbf{e}_{k+1} = \mathbf{v}_{meas,k+1} - \hat{\mathbf{A}}_{k+1/k}\mathbf{v}_{model,k+1} \tag{4.44}$$

5. Obtain the state perturbation vector

$$\delta\mathbf{x}_{k+1} = \mathbf{K}_{k+1}\mathbf{e}_{k+1} \tag{4.45}$$

6. Update the state vector

$$\hat{\mathbf{x}}_{k+1/k+1} = \hat{\mathbf{x}}_{k+1/k} + \delta\mathbf{x}_{k+1} \tag{4.46}$$

The quaternions in the updated state vector are normalized so that the quaternions constraint of Equation (2.6) remains valid. Hereafter $\mathbf{H}_{k+1/k+1}$ is computed using the updated normalized quaternions.

7. Update the state perturbation covariance matrix

$$\mathbf{P}_{k+1/k+1} = \left[\mathbf{I}_{7\times7} - \mathbf{K}_{k+1}\mathbf{H}_{k+1/k+1}\right]\mathbf{P}_{k+1/k}\left[\mathbf{I}_{7\times7} - \mathbf{K}_{k+1}\mathbf{H}_{k+1/k+1}\right]^{\mathrm{T}} + \mathbf{K}_{k+1}\mathbf{R}\mathbf{K}^{\mathrm{T}}_{\mathrm{k+1}} \tag{4.47}$$

The steps 3-7 are repeated for each sensor update in an estimation cycle.

Stellenbosch University https://scholar.sun.ac.za

4.2 Attitude control

This section describes the attitude control algorithms that were used during the mission ADCS simulations. The magnetic controllers were primarily used for rate damping and RW momentum management while the wheel controllers were utilized for fine pointing control.

4.2.1 Magnetic Control

An active magnetic control for the satellites uses the magnetometer to acquire the geomagnetic field vector in the BRC frame $\mathbf{B}_b$ and generates magnetic dipole moment commands $\mathbf{M}$ for the three orthogonally placed magnetorquers. This magnetic dipole interacts with the geomagnetic field to generate the magnetic control torques.

$$\mathbf{N}_m = \mathbf{M} \times \mathbf{B}_b \tag{4.48}$$

The cross-product relation in Equation (4.48) implies that a magnetorquer cannot generate magnetic torque parallel its axis of placement and the maximum magnetic torque is generated, for the case when $\mathbf{B}_b \perp \mathbf{M}$. As described previously in Chapter 3, the control cycle for the magnetic controllers is 10 seconds for the project, with 0.1 seconds resolution for the magnetorquers on-times. The effective magnetic moment generated for a certain on-time command is determined as,

$$M_{effective} = \frac{t_{on}}{10} M_{max} \tag{4.49}$$

4.2.1.1 B-dot Controller

The B-dot controller is a popular control law for angular rate damping in LEO satellites due to it simple operation. The controller does not require any attitude or rate knowledge and is quite easy to implement. The B-dot controller makes use of the 3-axis magnetic field measurements from the magnetometer and pulses the Y-axis magnetorquer to align the body Y-axis with the orbit normal. Consequently, the body rates along the X-axis and the Z-axis are also damped.

The angle between the magnetic field vector and its component along the body Y-axis is referred as β angle. The B-dot controller generates magnetic moment command M_y

Stellenbosch University https://scholar.sun.ac.za

proportional to the rate of change in the β angle. The characteristic equation of the B-dot control law is expressed as follows [53] ,

$$M_y = K_d\dot{\beta} \tag{4.50}$$

where, $$\beta = \cos^{-1}\left(\frac{B_y}{\sqrt{B_x^2+B_y^2+B_z^2}}\right)$$

The gain K_d was determined experimentally through simulations to achieve the desired performance with minimal magnetorquer on-times.

4.2.1.2 Y-spin Controller

An LEO satellite with its largest MOI around the Y-axis demonstrates a stable and energy efficient spin along the Y-axis. Therefore, a Y-spin magnetic controller is normally implemented with the B-dot controller in the safe mode of the satellite. The Y-spin controller drives the X or the Z-magnetorquer to spin the satellite about the body Y-axis at the reference angular rate. The control law for the Y-spin controller is implemented as follows [54],

$$M_x = K_s\left(\hat{\omega}_{yo} - \omega_{yo-ref}\right)\text{sgn}\,(B_{bz}) \;\;,\quad M_z = 0 \quad \text{if } |B_{bz}| \geq |B_{bx}| \tag{4.51}$$

$$M_z = K_s\left(\omega_{yo-ref} - \hat{\omega}_{yo}\right)\text{sgn}\,(B_{bx}) \;\;,\quad M_x = 0 \quad \text{if } |B_{bx}| > |B_{bz}| \tag{4.52}$$

The gain of Y-spin controller (K_s) was optimised experimentally through simulations. The rate information required for the controller was taken from the RKF.

4.2.1.3 Cross Product Controller

The essence of the cross-product magnetic controller is to minimize a control error vector **e** using the magnetic torques $\mathbf{N}_m$. The definition of the vector **e** is different according to the controller application. For instance, the vector **e** contains the body angular rates for the case of a rate damping implementation and it is comprised of the body angular momentum values for the momentum unloading application. As the name suggests, the control torque is calculated by the vector cross-product operation,

$$\mathbf{N}_m = -\mathbf{e} \tag{4.53}$$

Stellenbosch University https://scholar.sun.ac.za

$$\mathbf{M} \times \mathbf{B}_b = -\mathbf{e} \tag{4.54}$$

After some intermediate mathematical manipulations,

$$\mathbf{M} = \frac{\mathbf{e} \times \mathbf{B}_b}{\|\mathbf{B}_b\|^2} \tag{4.55}$$

4.2.1.3.1 Cross Product Law Applications

The cross-product controller was used in this project for RW momentum management and also for nutation damping during single wheel control. Some of the implementations of cross- product controller regarding different applications are presented here.

Rate Damping:

The control error vector in cross-product controller can be manipulated as follows to be used during the detumbling phase of satellite to serve the same purpose as that of the B-dot and the Y-spin controller,

$$\mathbf{e} = \begin{bmatrix} K_{dx}\widehat{\omega}_{xo} \\ K_{dy}(\widehat{\omega}_{yo} - \omega_{yo-ref}) \\ K_{dz}\widehat{\omega}_{zo} \end{bmatrix} \tag{4.56}$$

However, unlike the B-dot controller, the cross-product controller requires angular rate estimates for active rate damping.

Momentum Unloading:

The implementation of the cross-product law to manage the wheel angular momentum during the wheel pointing modes is given as follows,

$$\mathbf{e} = -K_w \Delta\mathbf{h}_w = -K_w(\mathbf{h}_w - \mathbf{h}_{w-ref}) \tag{4.57}$$

and from Equation (4.55),

$$\begin{bmatrix} M_x \\ M_y \\ M_z \end{bmatrix} = \frac{-K_w}{\|\mathbf{B}_b\|^2} \begin{bmatrix} B_{by}\Delta h_{wz} - B_{bz}\Delta h_{wy} \\ B_{bz}\Delta h_{wx} - B_{bx}\Delta h_{wz} \\ B_{bx}\Delta h_{wy} - B_{by}\Delta h_{wx} \end{bmatrix} \tag{4.58}$$

Cross Product with Y-Momentum Biased:

Stellenbosch University https://scholar.sun.ac.za

In the Y-momentum biased ADCS configuration, with the Y-wheel providing the gyroscopic rigidity, the cross-product controller can be implemented to damp the X and the Z body rates.

$$\mathbf{e} = \begin{bmatrix} K_{dx}\hat{\omega}_{xo} \\ K_{dy}(h_{wy} - h_{wy-ref}) \\ K_{dz}\hat{\omega}_{zo} \end{bmatrix} \tag{4.59}$$

The gains of the cross product controller are determined experimentally through simulations. Steyn [55] revealed a modified form of the cross-product controller that reduces the dependency of the controller output on the magnitude of the geomagnetic field vector and is given as follows,

$$\mathbf{M} = \frac{\mathbf{e} \times \mathbf{B}_b}{\|\mathbf{B}_b\|} \tag{4.60}$$

4.2.2 **Wheel Control**

The wheel controllers are used for precise pointing control and require the estimated attitude and the rate information to control the satellite attitude. The output of the RW wheel controller is a torque command that is numerically integrated to acquire a speed reference for the RW unit.

$$\mathbf{h}_{RW}(k) = \mathbf{h}_{RW}(k-1) + \mathbf{N}_{RW}\Delta T \tag{4.61}$$

and,

$$\mathbf{h}_{RW} = I_{RW}\boldsymbol{\omega}_{RW} \quad \Rightarrow \quad \boldsymbol{\omega}_{RW} = \frac{\mathbf{h}_{RW}}{I_{RW}} \tag{4.62}$$

The quaternion feedback controller was used in the project for 3-axis pointing using reaction wheels. Another control configuration, which utilizes the Y-wheel for pointing in pitch and the cross-product law of Equation (4.58) for the nutation damping was also implemented. However, the wheel control for this configuration was also based on the quaternion feedback controller but implemented for a single RW.

Stellenbosch University https://scholar.sun.ac.za

4.2.2.1 Quaternion Feedback Controller

The difference between the commanded quaternions $\mathbf{q}_c$ and the current quaternions $\mathbf{q}$ is referred as the quaternion error $\mathbf{q}_e$ and is calculated as follows,

$$\mathbf{q}_e = \mathbf{q} \ominus \mathbf{q}_c \tag{4.63}$$

$$\begin{bmatrix} q_{e1} \\ q_{e2} \\ q_{e3} \\ q_{e4} \end{bmatrix} = \begin{bmatrix} q_{c4} & q_{c3} & -q_{c2} & -q_{c1} \\ -q_{c3} & q_{c4} & q_{c1} & -q_{c2} \\ q_{c2} & -q_{c1} & q_{c4} & -q_{c3} \\ q_{c1} & q_{c2} & q_{c3} & q_{c4} \end{bmatrix} \begin{bmatrix} q_1 \\ q_2 \\ q_3 \\ q_4 \end{bmatrix} \tag{4.64}$$

where, $\mathbf{q}_{vec} = [q_{e1} \quad q_{e2} \quad q_{e3}]^{\mathrm{T}}$ is the vector part of the quaternion error and is used in the attitude control. The globally stable quaternion feedback wheel controller is expressed as follows [56] ,

$$\mathbf{N}_{RW} = K_p \mathbf{I}\, \mathbf{q}_{vec} + K_d \mathbf{I}\, \boldsymbol{\omega}_{BO} \tag{4.65}$$

where, $\mathbf{I}$ is the MOI tensor of the satellite. The values of the gains K_p and K_d are determined as follows,

For a small rotation (θ) around the Y-axis, the small angle approximation suggests $\dot{\theta} \approx \omega_{yo} \cong \omega_{yi}$. Assuming the angular rates along the X and the Z-axis to be very small

$$\mathbf{q}_{vec} = \left[\sin\frac{\theta}{2} \quad 0 \quad 0\right]^{\mathrm{T}}$$

The dynamics equation can be simplified as,

$$I_{yy}\ddot{\theta} + K_d I_{yy}\dot{\theta} + K_p I_{yy} \sin\frac{\theta}{2} = N_{my} + N_{dy}$$

The assumption of a small quaternion error suggests $\sin\frac{\theta}{2} \approx \frac{\theta}{2}$. Taking the Laplace transform,

$$\left(s^2 + K_d s + \frac{K_p}{2}\right)\theta(s) = \frac{N_{my}(s) + N_{dy}(s)}{I_{yy}}$$

Stellenbosch University https://scholar.sun.ac.za

For the desired closed-loop performance specified by the damping ratio ζ and the natural frequency ω_n,

$$K_p = 2\zeta\omega_n \quad , \quad K_d = 2\omega_n^2 \tag{4.66}$$

4.3 Summary

An overview of the ADCS algorithms, used in the mission ADCS was presented in this chapter. The TRIAD method is simple to implement, but is more susceptive to the sensor noise. It requires the measurements of two different vectors for attitude determination. The RKF provides the estimates of the inertial body rates by observing the change in the vector measurements. In the mission ADCS, the RKF was used to estimate the body rates during the detumbling mode by utilizing the magnetometer measurements. A full state EKF was implemented to provide the attitude quaternions and the inertial body rates. The EKF utilized the measurements from the available attitude sensors depending on the mission mode. The attitude control algorithms included the magnetic controller and the wheel controllers. The B-dot controller is an effective and easy to implement magnetic controller for active rate damping. It aligns the satellite body Y-axis to the orbit normal. The Y-spin magnetic controller is implemented along with the B-dot controller in the safe mode to spin the satellite along the Y-axis with a reference rate. The cross-product magnetic controller can be implemented for various applications such as rate damping, momentum unloading and nutation damping. The gains of the magnetic controllers were tuned experimentally based on simulation for optimal magnetorquer activity. The RW control algorithms were based on the globally stable quaternion feedback controller that takes the quaternion error and the orbit referenced body rates as input and outputs a torque command. This torque command is converted to the speed command and is sent to the respective RW unit as the reference speed.

Stellenbosch University https://scholar.sun.ac.za

5. Simulations for In-Orbit ADCS Performance

The in-orbit performance of the ADCS of a satellite can be determined through simulations in a realistic simulation environment. Therefore, a simulation environment in Matlab Simulink was developed to simulate the mission ADCS performance. The models for the satellite dynamics and kinematic, described in Chapter 2, were implemented for the simulations. Similarly, the ADCS hardware specifications from Chapter 3 were used to model the ADCS hardware in the simulation environment. The ADCS mission modes were defined based on the in-orbit operations of the satellite and the ADCS algorithms described in Chapter 4 were implemented and executed according to the mode definitions. This chapter provides an overview of the ADCS simulation environment and discusses the ADCS mode definitions with the performance simulations of the ADCS in each mode.

5.1 Simulations Models

Similar to the elements of a general control system loop, the ADCS simulation environment contains a plant, a 'sensors and estimators' block and a controller block. The elements of the simulation environment, arranged in the form of a simple control loop are presented in Figure 5-1.

5.1.1 Plant

The plant in the simplified control loop of Figure 5-1 is the *satellite model*, which contains the implementation of dynamic and kinematics equations of motion of the satellite. The implementation of satellite dynamics also takes into account the POI values of the satellite therefore, the complete inertia tensor matrix was provided as input to the block to parameterize the mission satellite. The other inputs to the satellite model include the control torques from the magnetorquers and the reaction wheels, the disturbance torques, the wheels angular momentum values, the orbital radius and the current orbital angular velocity. The outputs of the block are the true body rates with reference to the IRC and the ORC, and the true attitude in terms of both the quaternions and the DCM. The satellite model block is shown in Figure 5-2.

Stellenbosch University https://scholar.sun.ac.za

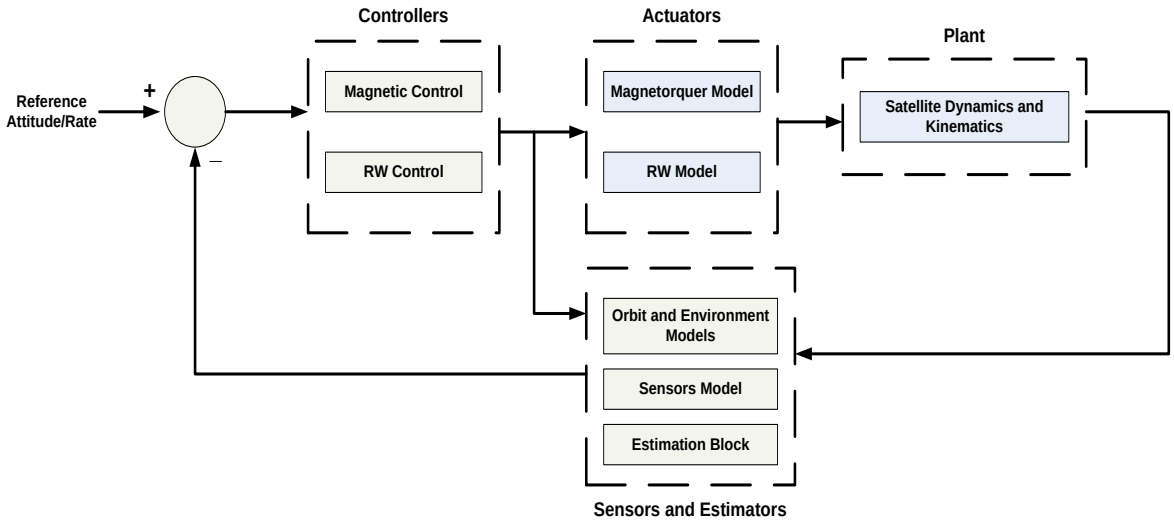

Figure 5-1: The ADCS simulation environment as a simple control loop

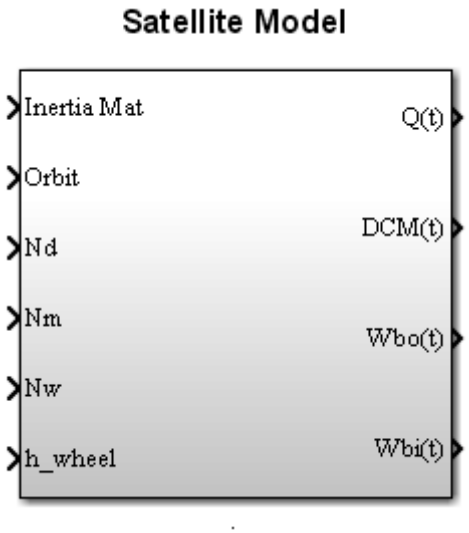

Figure 5-2: The satellite model in Simulink

5.1.2 **Sensors and Estimators**

The *Sensors and Estimators* section of the simulation environment is a set of three blocks namely, the *environmental model*, the *sensors model* and the *estimation* block. The *environmental models* block used in the simulation environment was taken from the ESL ADCS libraries. It consists of the mathematical models to propagate the satellite orbital position and velocity vectors. Moreover, the models to determine the sun position vector and the geomagnetic field vector in the orbit are also part of the block. The Simplified General Perturbations No.4 (SGP4) model [27] was used in the *environmental models* to propagate the orbit using the NORAD Two-Line Elements (TLE) set of the Sumbandila satellite. The

Stellenbosch University https://scholar.sun.ac.za

model outputs the inertial position and the velocity vector of the satellite. From the unit position vector of the satellite $\bar{\mathbf{u}}_I$ and the satellite velocity unit vector $\bar{\mathbf{v}}_I$, in the ECI frame, the transformation matrix from the ECI to the ORC frame can be determined by using the following expression [57],

$$A^{ORC/ECI} = \begin{bmatrix} (\bar{\mathbf{u}}_I \times (\bar{\mathbf{v}}_I \times \bar{\mathbf{u}}_I))^T \\ (\bar{\mathbf{v}}_I \times \bar{\mathbf{u}}_I)^T \\ -\bar{\mathbf{u}}_I{}^T \end{bmatrix} \tag{5.1}$$

A sun orbit propagator and a sun model is also part of the *environmental model* block. The sun propagator takes the simulation time and the current Julian date from the TLE values, to output the latitude and the longitude of the sun in the ECI frame. This information is then used by the sun model to determine the unit position vector of the sun from the satellite, in the ECI frame. The model for the nadir vector in the ORC is simple due to the axis definitions of the ORC and was taken as $\bar{\mathbf{n}}_{ORC} = [0 \quad 0 \quad 1]^T$. A 10th order IGRF model for the earth magnetic field [58] was used in the *environmental model* to determine the local geomagnetic field vector in the ECEF frame. The geomagnetic field vector is then transformed to the ORC frame and is utilized in the magnetometer model.

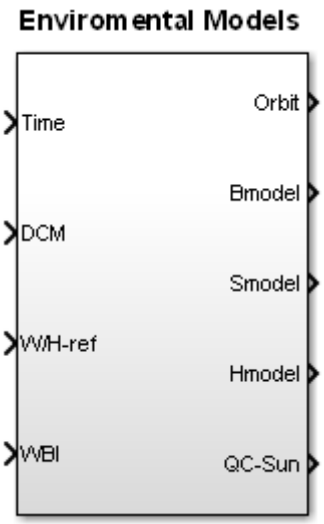

Figure 5-3: The orbit and the environmental block

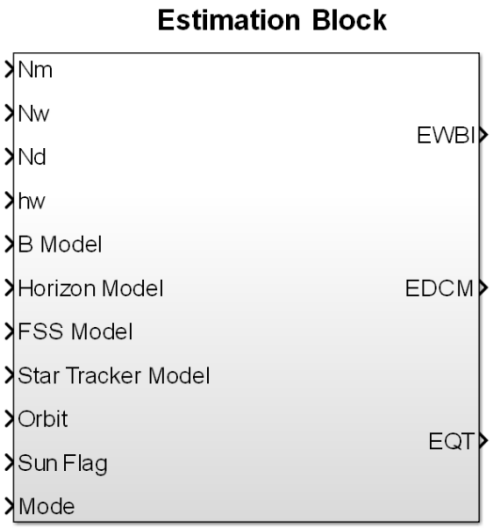

Figure 5-4: The estimation block

The *sensors model* takes as inputs, the modelled vectors in the ORC from the *environmental model* block and the true DCM from the *satellite model* block to transform the modelled vector to the BRC. Moreover, it adds randomly generated zero-mean Gaussian noise to the

Stellenbosch University https://scholar.sun.ac.za

transformed vectors. The standard deviation for the noise is set according to the specification of each sensor. Table 5-1 lists the accuracy values of the ADCS sensors used in the simulations. The *sensors model* block also generates a *sensor valid* signal based on the FOV of a sensor and the *estimation* block utilizes only that sensor information whose *sensor valid* signal is high.

$$\mathbf{V}_{sensor} = \mathbf{A}^{BRC/ORC}\mathbf{V}_{model} + \mathbf{m_k} \tag{5.2}$$

Moreover, an eclipse flag is also generated by the sensors block that goes true as the satellite enters the eclipse part of the orbit. The output of both the FSS and the horizon sensor are invalid during the eclipse period.

Table 5-1: The sensors' parameters used for the simulations

Sensor	Accuracy
Magnetometer	0.1 μT
CubeSense	0.3° Horizon , 0.4° FSS
CubeStar	Bore-sight pointing accuracy < 36 arc sec RMS

A simplified model to simulate the function of a star camera was created in Simulink. The model contains three unit vectors pointing in different directions around the bore sight of the star camera in the BRC. These vectors represent the unit position vectors of three stars that are inside the FOV of the Star Camera. The corresponding vectors in the ORC are obtained by multiplying these vectors with the transpose of the true DCM. Hereafter, random Gaussian noise is added to each vector in the BRC according to the CubeStar specification. The modelled vectors in the ORC and the measured vectors with added noise in the BRC are then fed to the EKF block as the star camera output.

The *estimation* block contains the implementations of all the attitude determination algorithms described in Section 4.1. The input signals and output signals of the block are shown in Figure 5-4. The Mode input of the block selects the estimation algorithm and its sub-modes. The details of the select options are listed in Table 5-2. The orbit input is taken from the *environmental models* block containing the information of the current orbital radius

Stellenbosch University https://scholar.sun.ac.za

and the current orbital velocity. The modelled and the measured vector pairs for each sensor are provided to the block from the *sensors model*.

Table 5-2: The estimation block modes details

Estimator Mode	Estimation Algorithm	Sensors Data
0	No Estimation	---
1	RKF initialization	Magnetometer
2	RKF output	Magnetometer
3	EKF Initialization	Magnetometer , FSS and Horizon Sensor (if available)
4	EKF output	Magnetometer, FSS and Horizon Sensor (during the sunlit part). Only magnetometer during eclipse
5	EKF output	Magnetometer , Star Camera, FSS and Horizon Sensor (during Sunlit)
6	TRIAD	Magnetometer and FSS (valid during Sunlit)

5.1.3 Controllers

The control part of the simulation environment comprises of the *magnetic control* block and the *reaction wheel control* block. These blocks incorporate the implementations of the control algorithms discussed in Section 4.2. The *magnetic control* and the *reaction wheel control* blocks are shown in Figure 5-5 and Figure 5-6.

The Mode input of the *magnetic control* block selects a specific magnetic controller and the Mode select values for selecting different magnetic controllers are described in Table 5-3. The *magnetic control* block requires as inputs the magnetometer readings, the orbit reference body rates, the reference angular momentum along the Y-axis, the reference rate for the Y-spin controller and the angular momentums of the wheels. The outputs of the *magnetic control* block are the magnetic toques for the *satellite model* block and the *estimation* block.

Stellenbosch University https://scholar.sun.ac.za

Moreover, the magnetorquers on-times are also provided as output for performance analysis purposes.

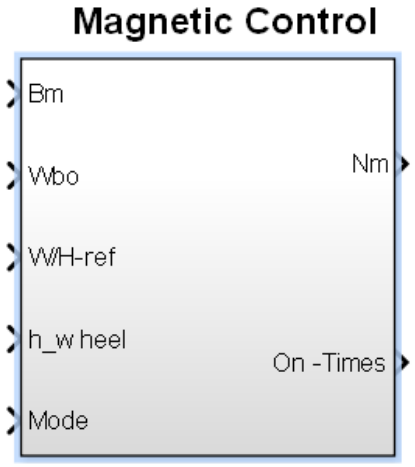

Figure 5-5: The Magnetic control Simulink block

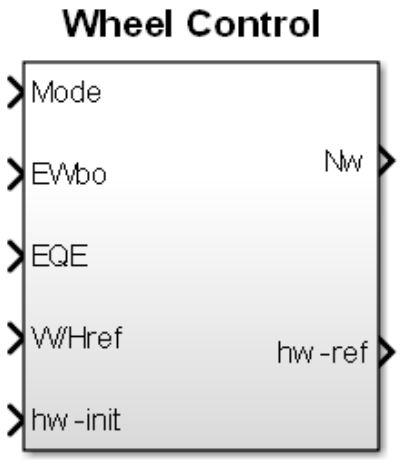

Figure 5-6:The RW control Simulink block

Table 5-3: The magnetic control modes

Magnetic Control Mode	**Control Algorithm**
0	Magnetorquer OFF , No Control
1	Cross-Product law for Nutation Damping
2	Cross-Product law for Momentum Unloading
3	B-dot Controller
4	B-dot Controller + Y-spin Controller

The *reaction wheel control* block consists of the implementations of the RW controllers described in Section 4.2.2. The Mode input of the *reaction wheel control* block is meant to select a specific wheel controller and its values for different controllers are presented in Table 5-4. The estimated quaternions and the estimated orbit referenced body rates are required as inputs by the block. Moreover, the initial angular momentum of the wheels and the reference angular momentum for the Y-momentum biased configuration are also provided to the block.

Stellenbosch University https://scholar.sun.ac.za

The outputs of the block are the RW torques for the *satellite model* and the *estimation* block. Moreover, the reference angular momentum is also provided for the RW model block in order to get the speed references for the RW speed controllers.

Table 5-4: The RW control modes

Wheel Control Mode	Control Algorithm
0	RW Wheel off , No wheel control
2	Pitch control only
3	3-axis quaternions feedback control

The RW model and its specifications in the simulation environment were the same as used for the RW speed controller design in Chapter 3. The magnetic moments of the magnetorquers were scaled to 1 Am^2 in simulations. The magnetorquer model used during the simulations converts the magnetic moment commands to the magnetorquers on-times and outputs the effective torques calculated by using Equation (4.48). The mission state machine was implemented in *mode switch* block that takes the simulation time as input and outputs the programmed modes for the controllers and the estimators.

5.2 Rate Estimators

This section presents the performance simulations of the RKF and the EKF for rate estimation during the tumbling state. The estimator outputs were utilized in the controlled state as well. However, the performances of the estimators in the controlled state shall be discussed later with the controller simulations.

5.2.1 The RKF Performance

The performance of the RKF during the tumbling state of the satellite is shown in Figure 5-7. The true inertial body rates during the tumbling state were taken as $[-3, 0.5, 2]\ deg/s$. The RKF was initialized at $t = 200\ s$. The initial estimated body rates in the RKF algorithm were taken as $[0\ 0\ 0]\ deg/s$.

Stellenbosch University https://scholar.sun.ac.za

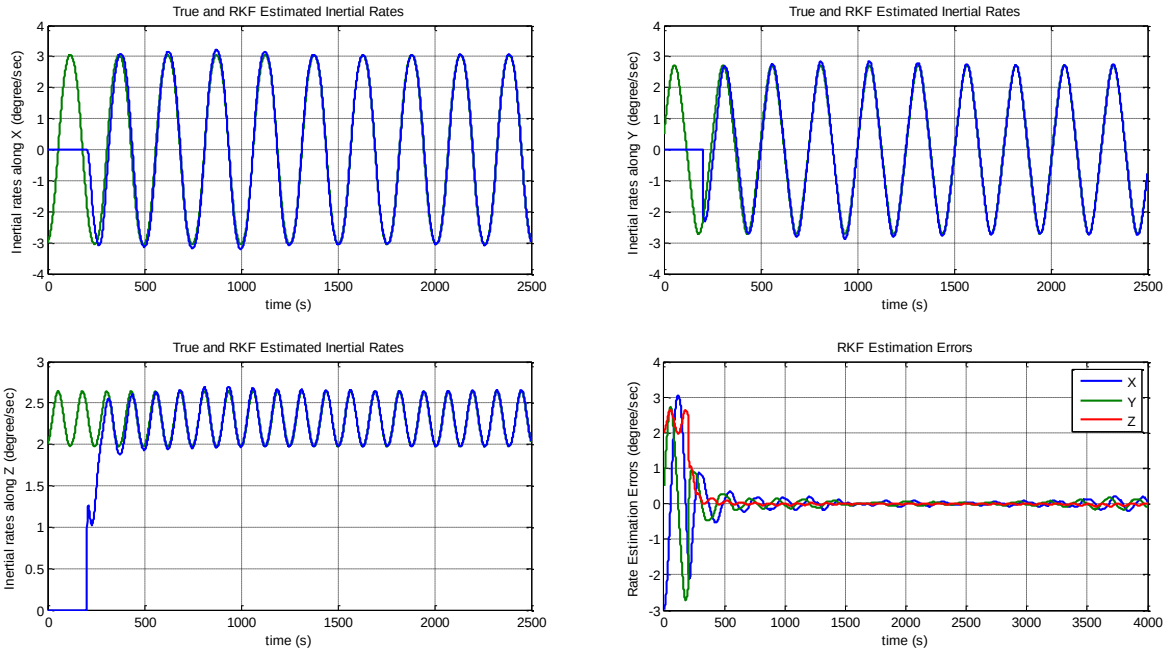

Figure 5-7: The RKF rate estimates during the tumbling state

In order to get better filtering performance, the elements of the **R** matrix were assigned higher values or in other words, the model predictions were given more weight as compared to the measurements. The initial value of the **P** matrix is assigned depending on the knowledge of the initial states, which in this case was not accurate as the filter was initialized with $[0\ 0\ 0]\ deg/s$. Therefore, the diagonal elements of the **P** matrix were initialized with a value of 3 (rad/s) ^{2}. The RKF estimation errors were less than $0.3°/s$ within 300 seconds of the initialization as evident from Figure 5-7. As the magnetic field vector rotates in the orbit therefore the RKF estimation errors changes over time as depicted in Figure 5-7.

5.2.2 **The EKF Performance**

The performance of the EKF in the tumbling state is presented in Figure 5-8. The body rates during the tumbling state were taken the same as those for the RKF. The EKF was initialized after 500 seconds with initial conditions $[0\ 0\ 0]\ deg/s$. The maximum rate estimation error after 300 seconds from the EKF initialization, was less than $0.15°/s$. It is evident from the estimation error plots that the EKF rate estimates are more accurate than the RKF estimates.

Stellenbosch University https://scholar.sun.ac.za

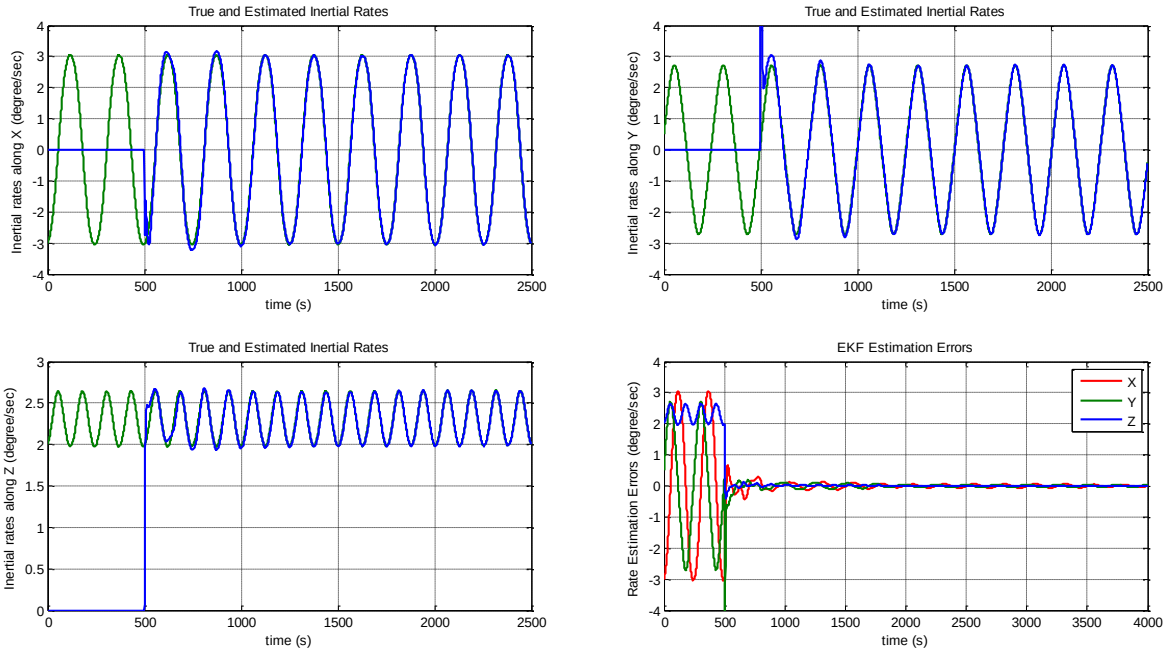

Figure 5-8: The EKF rate estimates during the tumbling state

Although the rate estimates from the EKF are more accurate, the RKF is computationally less expensive and is more robust in operation as it estimates 3 states from the measurements of 3 components of an inertial vector. The EKF estimates 7 states from the measurements of 3 components of a vector. Therefore, the RKF was used for rate estimation during the detumbling modes in the mission ADCS. The performances of the rate estimators in the stabilized mode shall be discussed in later sections.

5.3 ADCS Modes Definitions

5.3.1 Idle Mode

The Idle Mode refers to the period, when there is no control activated. In the mission ADCS scenario, the satellite is in the Idle Mode after separation from the launch vehicle and tumbles with the rates $[-3, 0.5, 2]\ deg/s$. The RKF is initialised in the Idle Mode so that it may converge before activating the magnetic control.

5.3.2 Safe Mode

The Safe Mode is also referred as the detumble mode and is activated to damp the body rates, when the satellite is released from the launch vehicle. The magnetic B-dot controller is activated during the detumble mode. As mentioned in the Section 4.2.1.1, the controller does not require any rate or attitude information and is fully based on the magnetometer readouts.

Stellenbosch University https://scholar.sun.ac.za

However, for telemetry purposes, the rate information is taken from the RKF. Once the satellite body rates are less than $0.3°/s$, the satellite is taken into the stable spin mode by activating Magnetic Control Mode-4. The Safe Mode shall be activated at any instant in the mission orbit, if the satellite body rates exceed a threshold of $3°/s$.

5.3.3 Imaging Mode

The RW control in Mode-3 is used with the Estimator Mode-5 during the Imaging Mode. The sensor updates from all available sensors including the star camera are used during this mode. The Imaging Mode is only activated during the sunlit part of the orbit.

5.3.4 Nominal Mode

In the Nominal Mode, the solar array of the satellite is pointed towards the sun during the sunlit part of the orbit using the RW control and during the eclipse part of the orbit the satellite keeps the nadir pointing attitude. The wheel control in Mode-3 is activated along with the Estimator Mode-4 during the Nominal Mode.

5.3.4.1 Momentum Management

The magnetic control in Mode-2 is used for unloading the RW angular momentum during the eclipse part of orbit in the Nominal Mode. The attitude and the rate information are taken from the EKF in the Estimation Mode-4 with only the magnetometer updates available.

5.4 Simulation Performance

In order to test the simulation performance of the designed ADCS, an ADCS events sequence was defined that switched different ADCS modes at different intervals of the simulation. Table 5-5 describes the ADCS events sequence programmed for the simulation.

Table 5-5: The ADCS events for the simulations

Time	**ADCS Events**	**Description**
>0 sec	Idle Mode	Initial rates $[-3, 0.5, 2]\ deg/s$. The RKF was initialized
>700 sec	B-dot controller was activated Rate telemetry was taken from	Y-magnetorquer was used to damp the X

Stellenbosch University https://scholar.sun.ac.za

	RKF	and the Z body rates.
>1 orbit	Magnetic Control Mode-4 was activated. B-dot + Y-spin Controller	The X and the Z-axis magnetorquers were used to spin the satellite around the body Y-axis at a reference angular of $-1\ °/s$
>2 orbit	The EKF was initialized	Rate Telemetry was from the RKF. The magnetic control Mode-4 was still activated
>3 orbit	Wheel control mode-2 with magnetic control mode-1 was activated.	The Y-wheel controller was used to absorb the angular momentum of the body along the Y-axis and to keep the commanded pitch pointing. Cross-product magnetic controller was used for the nutation damping. The attitude and the rate estimates were from the EKF in Estimator Mode-4.
>4 orbit	Wheel control mode-3 was activated with the Estimator Mode-4. The satellite was in its Nominal Mode	Sun tracking was performed during the sunlit part and momentum unloading operation was carried out, while keeping the nadir pointing attitude during the eclipse part of the orbit.
>5 orbit	The satellite entered from the Nominal Mode to the Imaging Mode. During the eclipse, the nadir pointing Nominal Mode was activated again.	Fine Target Pointing manoeuvre was performed with star tracker updates.
>6 orbit	Nominal Mode	Satellite remained in the Nominal Mode throughout the orbit.

Stellenbosch University https://scholar.sun.ac.za

5.4.1 The B-dot and the Y-Spin Controller Performance

The performance of the B-dot and the Y-Spin controller is depicted in Figure 5-9. The plots of the true inertial body rates are presented in the figure. The simulation was started with initial body rates of $[-3\ 0.5\ 2]\ deg/s$. The RKF was initialized at the start of the simulations with initial conditions $[0\ 0\ 0]\ deg/s$ and it converges within 100 seconds. The B-dot controller was activated at $t = 700\ s$ and the controller damped the X and the Z body rates to values less than $0.3\ °/s$ within 2250 seconds. At the start of the second orbit, the magnetic control Mode-4 was activated and the satellite undergoes a stable Y-spin with a reference rate of $-1°/s$.

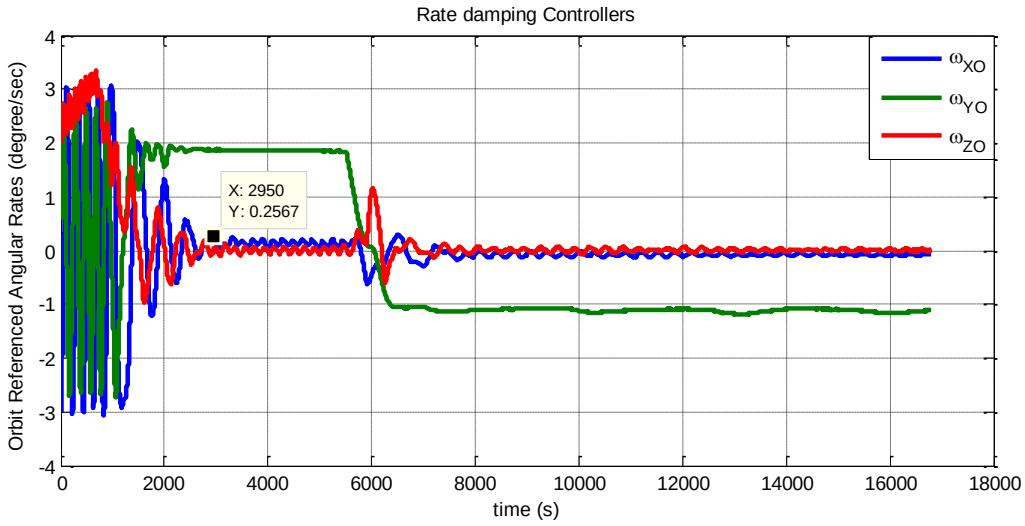

Figure 5-9: Orbit referenced body rates during the detumbling mode

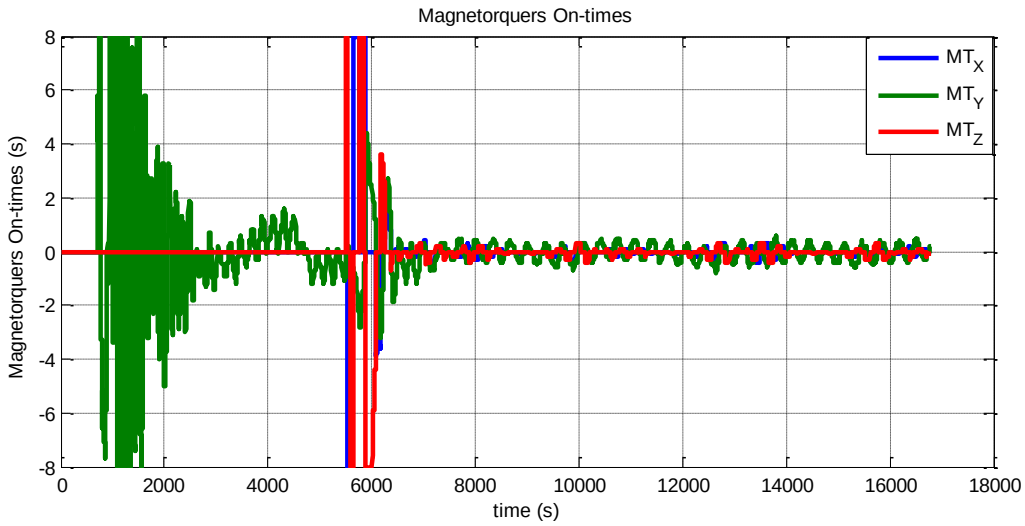

Figure 5-10: Signed on-times of the magnetorquers during the detumbling mode

Stellenbosch University https://scholar.sun.ac.za

The output of the RKF was used for the Y-spin controller. Figure 5-11 presents the plots of estimation errors of the RKF. As shown in Figure 5-11, the estimation errors are less than 0.07 $°/s$ before switching on the Y-spin controller in the start of the second orbit. The maximum estimation error after switching on the Y-spin controller remains less than 0.14 $°/s$ in all three axes. The gains of the B-dot and the Y-Spin controller were optimized for minimum magnetorquers on-times. The magnetorquers on-times for $K_d = 27.27$ and $K_s = 90.90$ during the detumbling mode simulations are presented in Table 5-6.

Table 5-6: The magnetorquers on-times for the detumbling controllers

Magnetorquer	X	Y	Z	Total
On-time (seconds)	381.2	1489	343.8	2214

As depicted in Figure 5-9 that the Y-spin controller spins the satellite at a reference rate of -1 $°/s$. The magnetorquers on-times for the detumbling controllers are plotted in Figure 5-10.

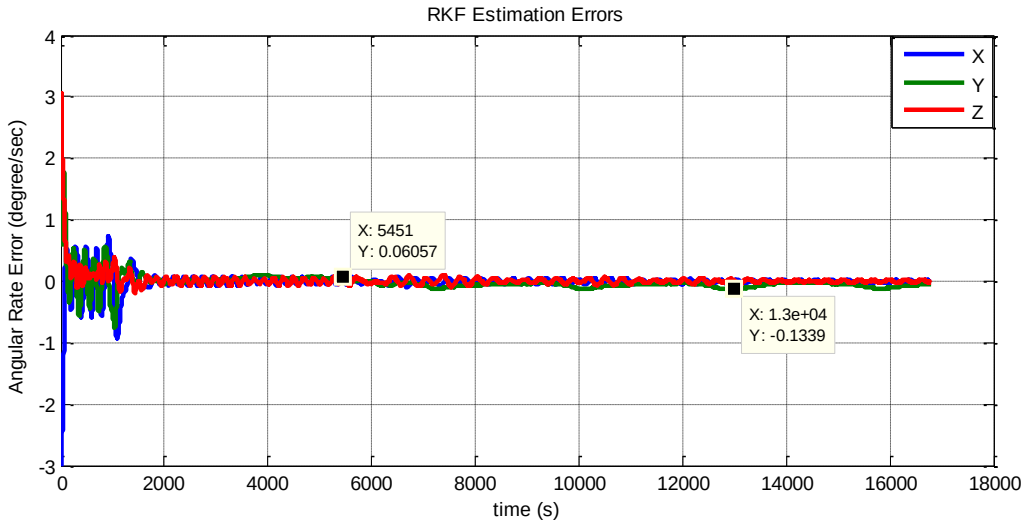

Figure 5-11: The RKF estimation errors during the detumbling mode

5.4.2 The Y-wheel RW Controller with Magnetic Nutation Damping

The Y-wheel RW controller was used to absorb the angular momentum of the satellite before activating the 3-axis RW control. It utilizes the Y-axis RW to point the satellite to the commanded pitch angle. Moreover, the cross-product law of Equation (4.56) is used along with the RW controller to damp the X and the Z-axis nutation rates. The performance of the

Stellenbosch University https://scholar.sun.ac.za

Y-wheel controller along with the nutation damping magnetic controller is depicted in Figure 5-12.

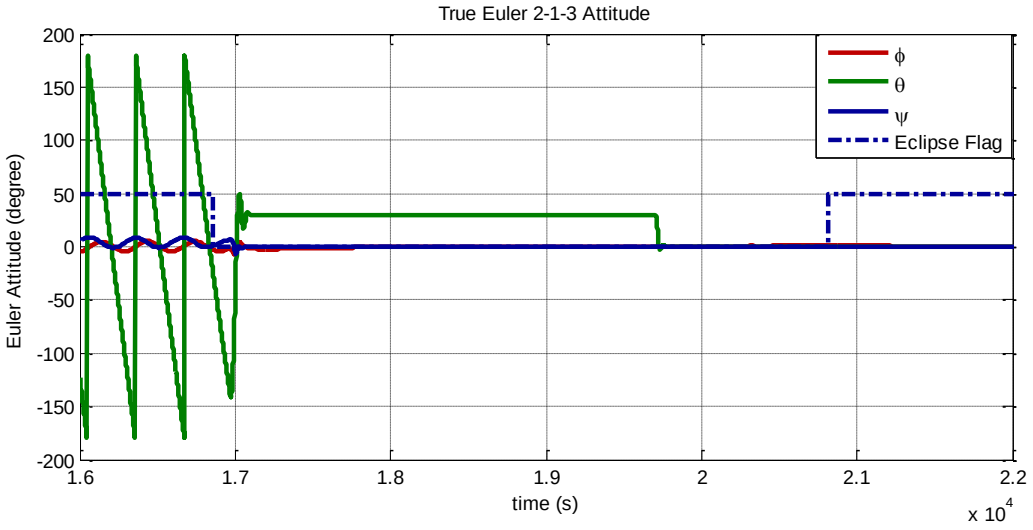

Figure 5-12: The Y-wheel control with cross-product nutation damping

The rate and the attitude estimates for this configuration were taken from the EKF in the Estimator Mode-4. The quaternion feedback controller was designed for a settling time of 30 seconds and a damping ratio of 0.8 using Equation (4.66). Figure 5-12 shows the true Euler attitude angles during the simulations for a 30° pitch command. Figure 5-13 presents the attitude estimates from a TRIAD algorithm using the FSS and the magnetometer data. It is clear from Figure 5-13 that the TRIAD estimates are noisy and not available during the eclipse, therefore these estimates are only used for EKF initializations in the mission ADCS.

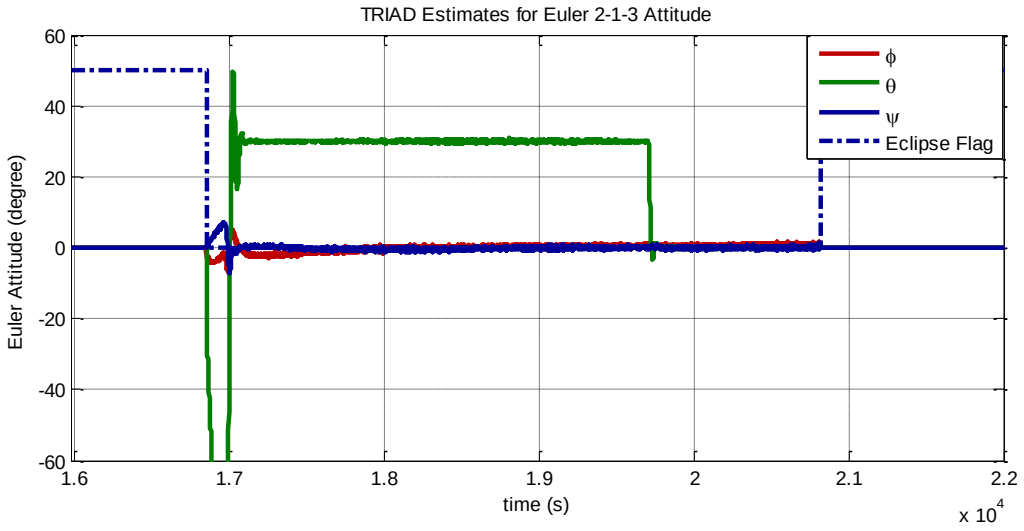

Figure 5-13: The TRIAD attitude estimates

Stellenbosch University https://scholar.sun.ac.za

5.4.3 **Wheel Pointing during Imaging Mode**

The EKF performance using star tracker measurements is depicted in Figure 5-14. A sinusoidal Euler attitude reference with [10° 10° 10°] peak was applied and the attitude was controlled by taking the true quaternions and the true body rates. After 200 seconds, the EKF was initialized in the Estimator Mode-5 with the star camera updates. The plots of the true and the estimated states are shown in Figure 5-14. The RMS errors for the attitude estimates were less than $12\ arc-second$ in all three axes and the RMS estimation errors for the angular rates were less than $4\ arc-second\ /\ second$ over a period of 2500 seconds.

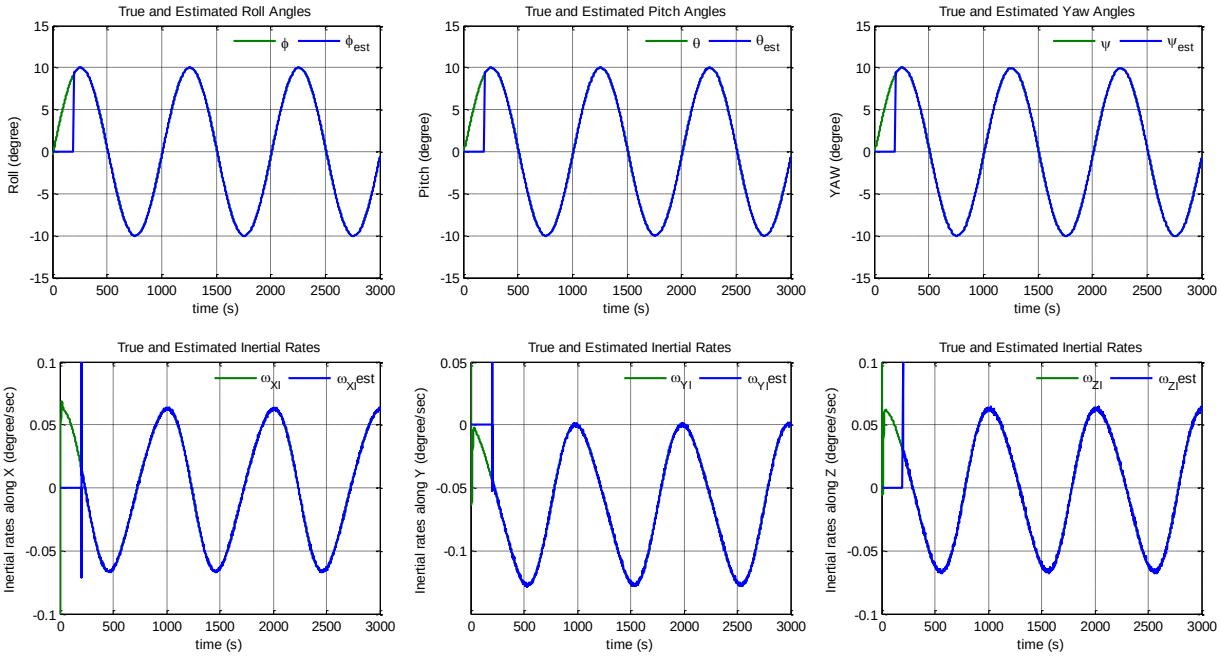

Figure 5-14: The EKF performance in controlled state

The Euler attitude angles during an imaging manoeuvre are shown in Figure 5-15. A 3-axis manoeuvre of $[-30^{\circ}, 10^{\circ}, 20^{\circ}]$ was commanded to point the satellite to the target. The RMS pointing errors for this simulation case were $[0.0254^{\circ}, 0.0240^{\circ}\ 0.0172^{\circ}]$. The pointing errors were less than 0.05° as required for the mission. The maximum angular rates during the steady state part of the pointing manoeuvre were less than 0.004°/s and thus the pointing stability requirements are also fulfilled.

Stellenbosch University https://scholar.sun.ac.za

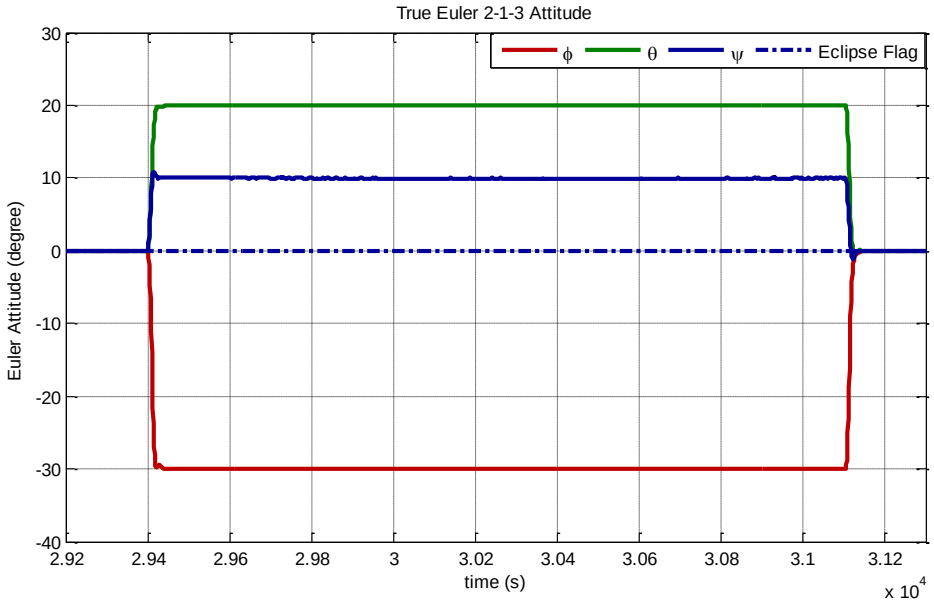

Figure 5-15: 3-axis pointing manoeuvre during the Imaging mode

5.4.4 Sun Tracking during the Nominal Mode

During the Sun Pointing mode, the quaternion feedback controller was used to point the satellite towards the sun. The attitude and the rate feedback were taken from the EKF in the Estimator Mode-4. The mission satellite has the solar cells array mounted on its –Y facet. In order to generate the reference quaternion command to point the –Y facet of the satellite towards the sun, the method described by Chen [59] was implemented. A unit vector $\mathbf{u}_c$ is defined in this method as follows,

$$\mathbf{u}_c = \frac{\mathbf{u}_{sp}^{BRC} \times \mathbf{S}_o}{\left\| \mathbf{u}_{sp}^{BRC} \times \mathbf{S}_o \right\|} \tag{5.3}$$

where $\mathbf{u}_{sp}^{BRC}$ is the unit position vector of the main solar panel in the BRC, which is $[0 \quad -1 \quad 0]^T$ for the mission satellite. $\mathbf{S}_o$ is the unit position vector of the sun in the ORC. The commanded quaternions for sun tracking can now be computed as follows,

$$\mathbf{q}_c = \begin{bmatrix} \mathbf{u}_c \sin\dfrac{\delta}{2} \\ \cos\dfrac{\delta}{2} \end{bmatrix} \tag{5.4}$$

Stellenbosch University https://scholar.sun.ac.za

where δ denotes the angle between the vectors $\mathbf{u}_{sp}^{BRC}$ and $\mathbf{S}_o$ and can be determined from the dot-product of the vectors [59, 30]. Figure 5-16 shows the Euler attitude during the sun tracking Nominal Mode. The Y-component of the FSS measurements in the BRC is shown in Figure 5-17. It is evident from Figure 5-17 that the Y-component of the unit sun vector in the BRC is -1, which implies that the body –Y axis is aligned with the unit sun vector during the sun tracking mode.

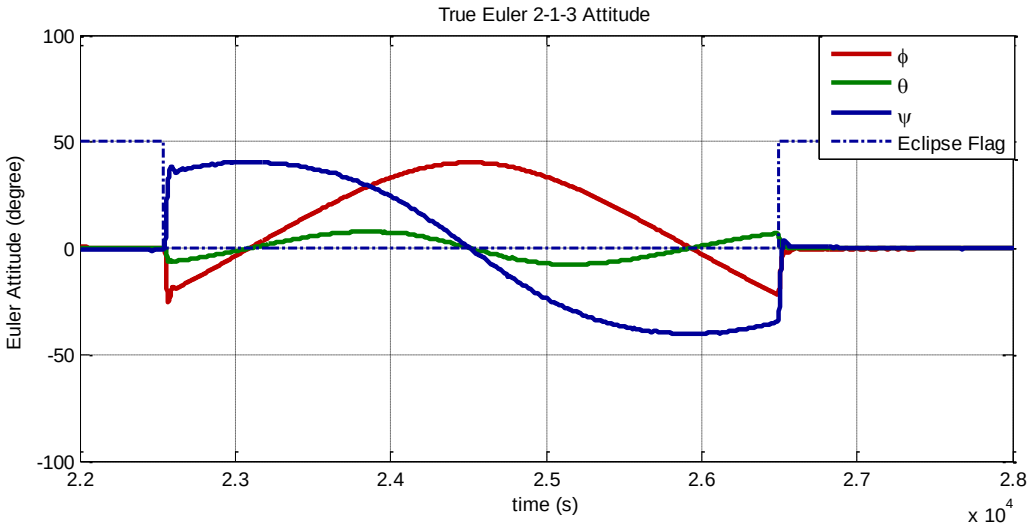

Figure 5-16: Sun Tracking with RW during the Nominal mode

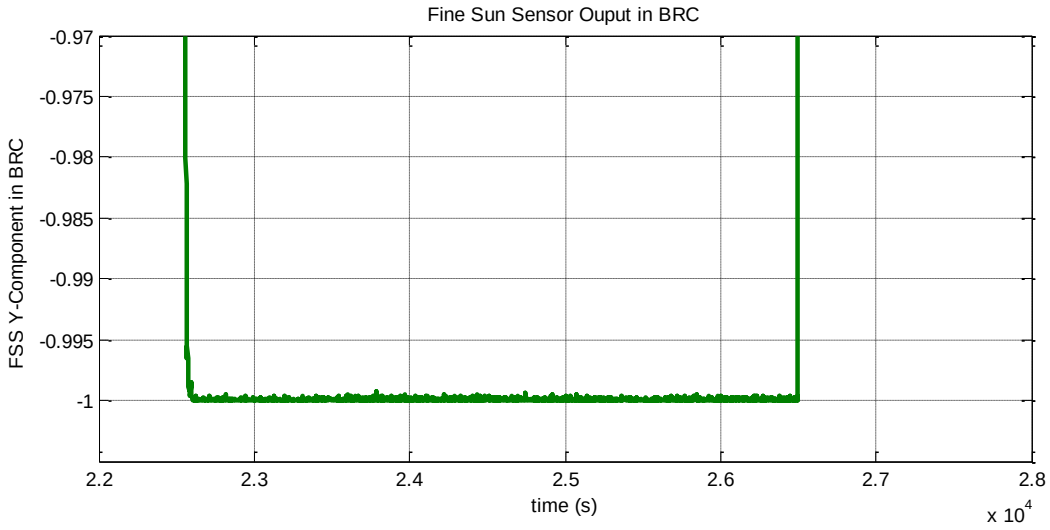

Figure 5-17: The Y-component of the FSS measurement vector during sun tracking

Stellenbosch University https://scholar.sun.ac.za

5.4.5 **Momentum Unloading Simulations**

Momentum unloading controller of Equation (4.58) was implemented to unload the accumulated angular momentum during the eclipse part of the Nominal Mode. The simulation results for three orbits are shown in the following figures. The satellite remains in Nominal Mode for the first orbit and is switched to the Imaging Mode as it comes out of eclipse. Hereafter, the Nominal Mode is activated again as soon as the satellite enters the eclipse. Figure 5-18 shows the plots of the Euler attitude during the simulation. The RW angular momentums are depicted in the plots of Figure 5-19 and the magnetorquer on-times for the momentum unloading operation are shown in Figure 5-20.

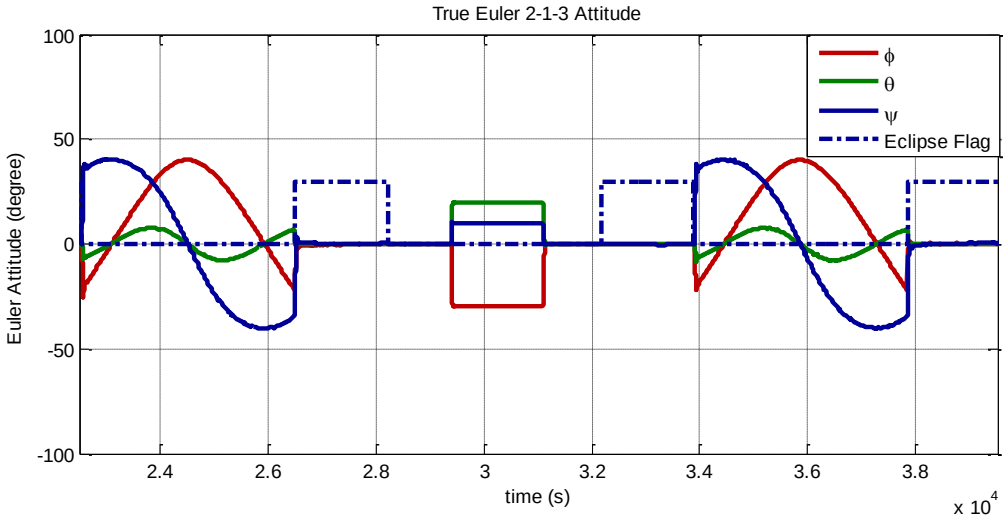

Figure 5-18: Mode transition from the Nominal mode to the Imaging mode

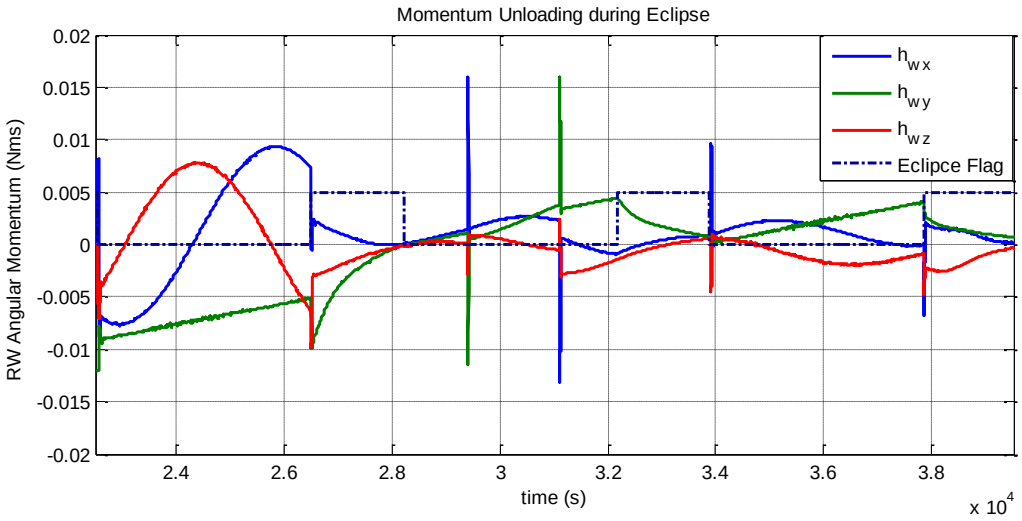

Figure 5-19: The RW angular momentums during the pointing modes

Stellenbosch University https://scholar.sun.ac.za

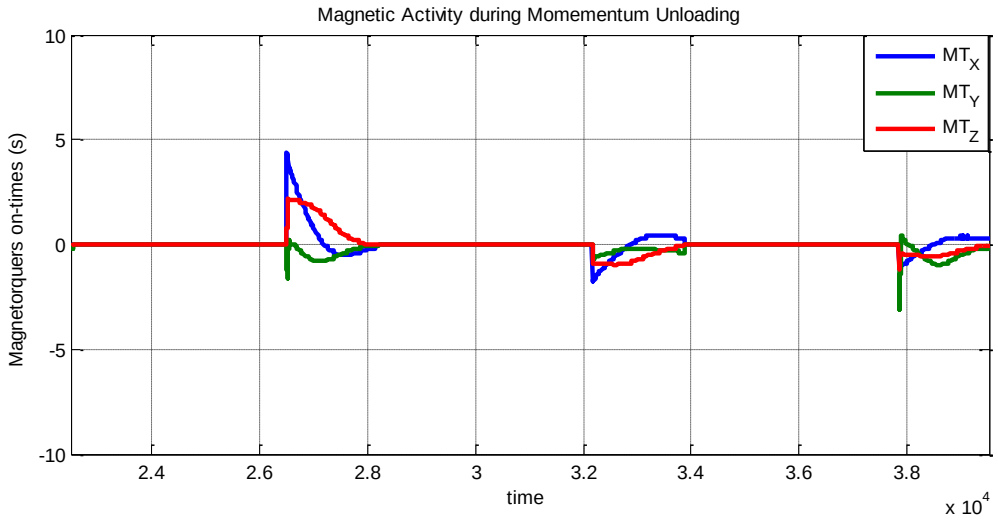

Figure 5-20: Signed on-times of the magnetorquers for momentum unloading operation

5.5 Summary

In order to evaluate the performance of the mission ADCS, a simulation environment was developed. The dynamics and kinematics of the satellite were modelled in the Matlab Simulink environment. The magnetic field vector and the unit position vector of the sun in the ORC were provided by the *environmental model* block in the simulation environment. The *sensors model* block contains the models of the ADCS sensors with realistic noise parameters. The *actuators* block contains the models of the RW and the magnetorquers. The RKF, the EKF and the TRIAD estimators were implemented inside the *estimation* block. The B-dot, the Y-spin and the cross-product controllers were implemented in the *magnetic control* block. The Y-wheel control and the 3-axis quaternion feedback controller were implemented in the *reaction wheel control* block. The ADCS modes were defined according to different on-board operations, which utilize different controllers and the estimator combinations. An ADCS event sequence was programmed in the simulation that switched different ADCS modes to evaluate the performance of the designed ADCS. The satellite was successfully brought from a tumbling state to a 3-axis stabilized state. The pointing accuracy achieved during the Imaging Mode was less than 0.03° RMS and the pointing stability during the target pointing was less than $0.004\ °/sec$. It can be concluded from the ADCS simulations results that the selected ADCS hardware and the designed ADCS algorithms fulfil the in-orbit performance requirements mentioned in Section 1.2.2.

Stellenbosch University https://scholar.sun.ac.za

6. The ADCS Testing in an HIL Environment

The cost of a satellite mission, from the design phase to the placement in orbit, is extraordinarily high therefore, comprehensive ground testing of all the subsystems of a satellite is extremely important to avoid some unforeseen behaviour that may occur after the launch. During the design phase of the ADCS hardware, unit level tests were conducted to verify the functionality of each ADCS unit. A subset of these ADCS units was then integrated together in different test configurations to perform the HIL testing in a test environment. This chapter presents the details of the HIL testing of the integrated ADCS units and illustrates the HIL test environment. Furthermore, the hardware configuration, the test strategies and the HIL test results are also illustrated. The main objectives of the HIL testing were to test the integrated operation of the ADCS units to validate the ADCS hardware and the software functionality. Moreover, the HIL testing was meant to verify the reliable operation of data exchange protocols among the ADCS units and also to test the ADCS algorithms in a test environment.

6.1 HIL Test Environment

Similar to the HIL test facilities, described in Section 1.3.4, the HIL testing environment at the ESL has a spherical air-bearing based turn table that features low friction motion to closely emulate the frictionless environment in space. The test facility also includes a Helmholtz cage to generate the magnetic field for the magnetometer and the magnetorquer operation. Moreover, a bright light source was included in the test environment to generate the sun reference vector for attitude determination.

6.1.1 Air-Bearing Table

The spherical air-bearing table at the ESL is based on the ‘ball and socket’ design in the ‘Tabletop’ configuration. It allows full 360° motion in the yaw or about the axis of spin, while the motion about the pitch and the roll is physically constrained to approximately 25°.

Stellenbosch University https://scholar.sun.ac.za

The socket assembly contains the holes for the air flow as can be seen in Figure 6-1 and pressurized nitrogen gas is utilized to form an air gap between the ball and the socket.

Figure 6-1: Air-bearing socket

Figure 6-2:Pressurized Nitrogen supply

The use of nitrogen gas is advantageous over compressed air as it is free from contaminations, such as water vapours or oil particles normally found in the compressed air. The outer surface of the ball is polished to minimize the surface friction.

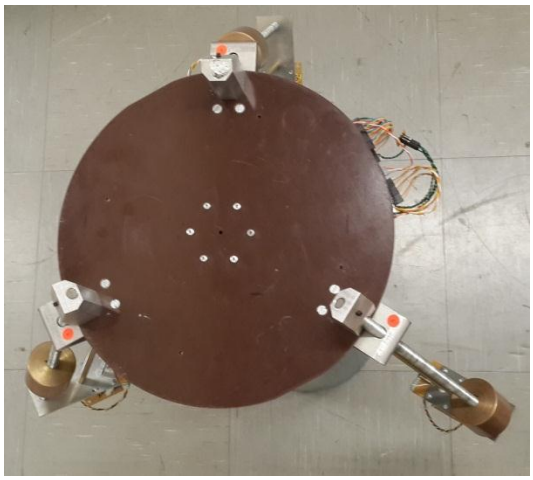

Figure 6-3: Top view of air-bearing table

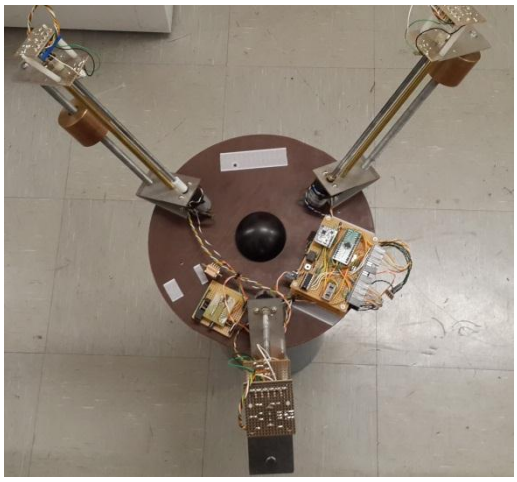

Figure 6-4: Bottom view of air-bearing table

The air-bearing table contains counter weights to manually adjust the CoM of the system as shown in Figure 6-3 and Figure 6-4. In the absence of the counter weights, the CoM would always be above the CoP and the system would be unstable like an inverted pendulum. If the

Stellenbosch University https://scholar.sun.ac.za

CoM is exactly below the CoP point, the system on the table top shall remain stationary, as the upward air pressure force balances the downward gravitational force.

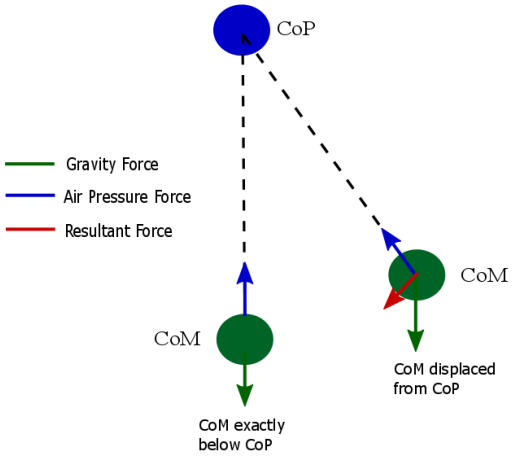

Figure 6-5: Pendulum motion of air-bearing system

It is quite difficult to position the CoM to exactly coincide with the CoP through manual adjustments of counter weights. Therefore, the counter weights are adjusted so that the CoM should be below the CoP, and both the points approximately coincide with each other. In this case, the system shall demonstrate a stable pendulum motion, as the CoM tries to maintain its steady position exactly below the CoP, due to the gravitational force. Figure 6-5 explains the pendulum motion of the air-bearing system.

6.1.2 **Helmholtz Cage System**

The design of the Helmholtz cage system in the ESL is explained by Van Vuuren [25]. It can generate uniform magnetic field within a cubic envelope of 20 cm at the centre of the cage. The maximum magnetic field strengths that can be achieved are 107.68 µT along the X-axis, 101.84 µT along the Y-axis and 99.11 µT along the Z-axis. In order to reject the ambient magnetic field variations and have a stable reference vector for attitude determination, a feedback control for the magnetic field inside the cage was implemented during this project. For this purpose, a fluxgate magnetometer was incorporated in the setup for the magnetic field feedback. Moreover, a PI controller was implemented and was manually tuned for a settling time of 10 seconds. The controller regulates the magnetic field inside the cage at the reference value with a control resolution of 20 nT. The currents inside the coils are controlled by the PWM signals from a microcontroller on the control board. These PWM

Stellenbosch University https://scholar.sun.ac.za

signals are fed to the H-bridge block as inputs, to set the current values for the Helmholtz coils [25]. Figure 6-6 explains the constituents of the Helmholtz Cage system used for the HIL testing.

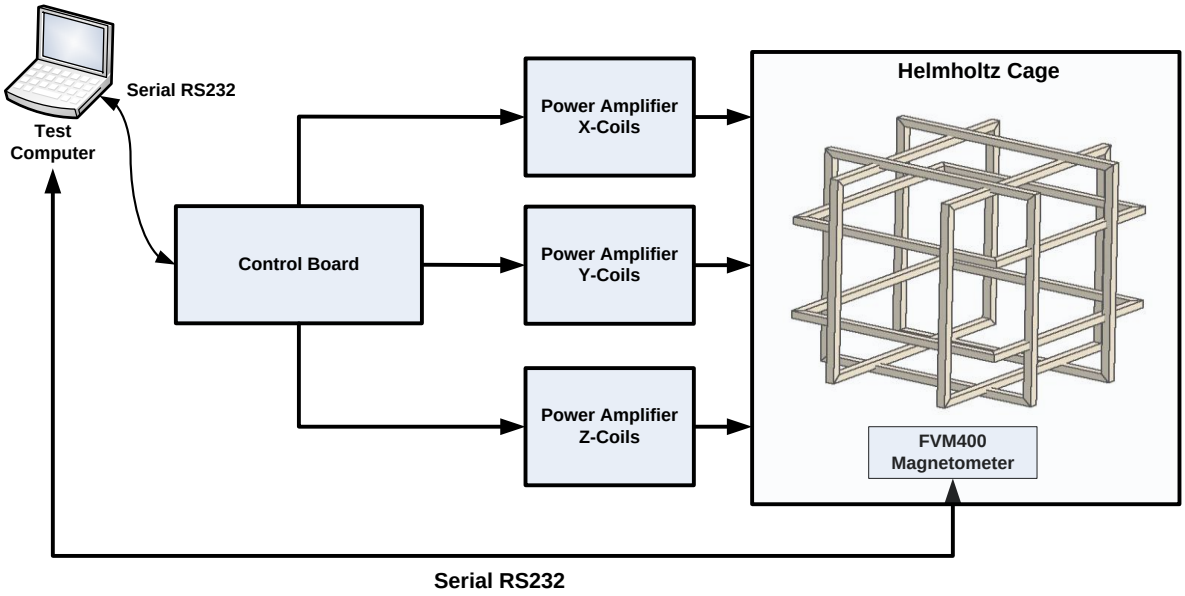

Figure 6-6:Helmholtz Cage System [26]

6.1.3 Sun Simulator

XP-E LEDs from Cree® was used to emulate the sun reference vector for the CubeSense operation. The light source was selected due to its wide viewing angle of 115° so that it can be used at different azimuth and elevation angles in the test environment.

Figure 6-7: Ultra bright LED lamp used in Sun Simulator

6.1.4 Test Computer

The test computer was used to control the magnetic field inside the Helmholtz cage. It communicates with a fluxgate magnetometer and with the current control circuitry of the Helmholtz Cage through the UART interface. The fluxgate magnetometer data was sampled every one second and after processing through a PI controller algorithm, the PWM duty cycles command was sent to the current control circuitry.

Stellenbosch University https://scholar.sun.ac.za

The ADCS algorithms for the HIL testing were also executed on the test computer. The test computer had a wireless radio link with the system on the air-bearing table. The XBee shield transceiver, a wireless UART, was connected with the test computer as a virtual COM port, while a real time Simulink s-function handled all the data communication and the ADCS algorithms.

6.2 HIL Hardware Configuration

The integrated ADCS hardware setup used for the HIL testing shall subsequently be referred as 'HIL-Demonstrator' in this document. The attitude, as described previously, is the orientation of the satellite body frame with respect to the reference frame. This section describes the definitions of the attitude reference frame during the HIL testing and the body reference frame for the HIL-Demonstrator. Moreover, it illustrates the placement of the sensors and the actuators in the HIL-Demonstrator.

The reference frame for the attitude determination during the HIL testing was the earth fixed NED (North East Down) frame and was defined with respect to some fixed objects inside the test lab. The X-axis of the frame points in the direction opposite to the front door of the lab, the Y-axis points to the environment testing room, and the Z-axis points downward to complete the right hand set. The axes of the Helmholtz Cage were also aligned with the NED frame to avoid any frame transformation for the generated magnetic field. The reference frame definitions are depicted in Figure 6-17.

An arbitrary point at one of the corner on the top facet of the HIL-Demonstrator was taken as the origin of the body reference frame and an arrow was then marked on the top facet of the HIL-Demonstrator to be taken as the X-axis of the BRC frame, the Z-axis points to the bottom facet of the HIL-Demonstrator and the Y-axis completes the right hand set of the Cartesian plane. The BRC frame for the HIL-Demonstrator can be seen in Figure 6-8. The placements of the sensors and the actuators were done subsequently with reference to the defined BRC frame.

6.2.1 Sensors Placement

The RM3000 magnetometer, the CubeSense and the Analogue Devices® IMU were the three sensors used in the HIL-Demonstrator. A magnetometer requires distant placement from the constant current carrying devices such as electric motors, magnetorquers, battery and power

Stellenbosch University https://scholar.sun.ac.za

lines to avoid the magnetic disturbances. Moreover, it must be mounted away from the ferromagnetic materials. Therefore, the magnetometer was mounted on the top of a bar, made of polystyrene material as shown in Figure 6-8. The polystyrene material was chosen as it is lighter in weight and has non-ferromagnetic properties.

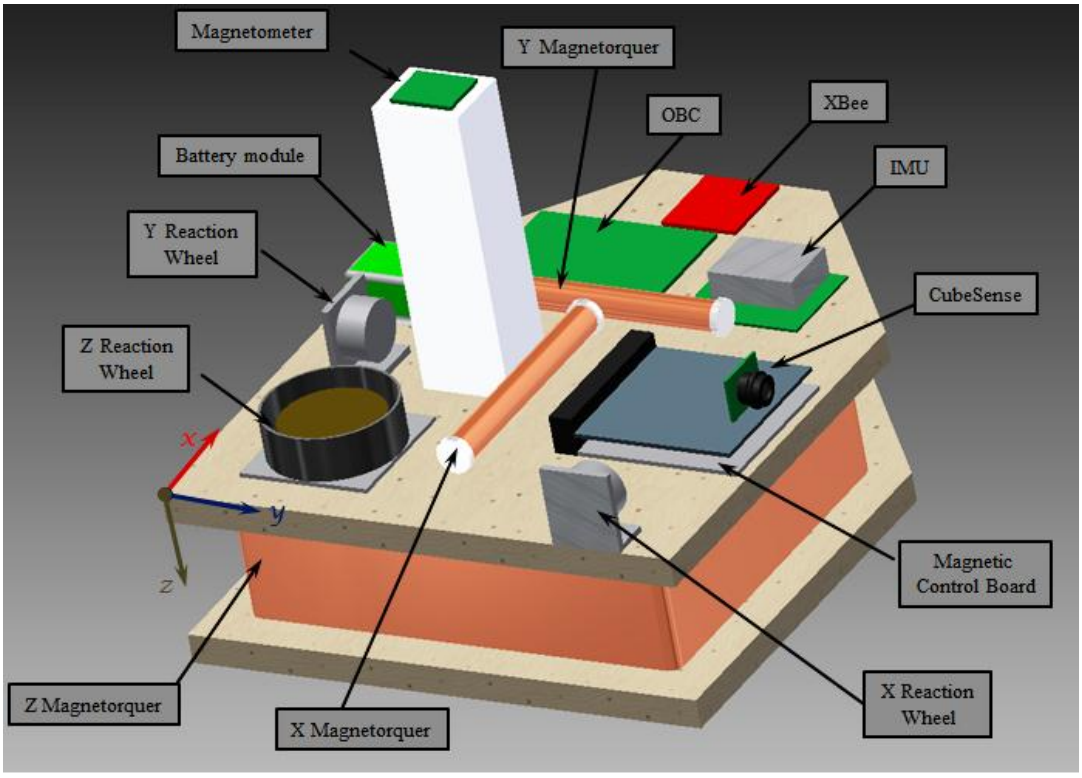

Figure 6-8: ADCS hardware configuration in HIL-Demonstrator

The height of the bar was chosen such that the magnetorquers and the magnetometer should be within the uniform magnetic field envelope at the centre of the cage. The RM3000 magnetometer measures the geomagnetic field vector and the placement orientation of the magnetometer in the HIL-Demonstrator was chosen such that its measurement frame coincided with the BRC frame and the mounting DCM for the magnetometer was therefore an identity matrix.

The CubeSense requires an unobstructed view of the sun simulator to measure the sun reference vector during the HIL testing. It was placed on the HIL-Demonstrator such that the camera bore sight was along the Y-axis of the BRC frame with an unobstructed field of view. The CubeSense outputs the position vector of the sun in its sensor reference coordinates (SRC) frame, which is described in the CubeSense User Manual. An axis transformation was required to convert the measured reference vector to the BRC frame. The DCM matrix to

Stellenbosch University https://scholar.sun.ac.za

transform the CubeSense SRC measurements to the BRC was evaluated and is given as follows,

$$\mathbf{C}^{BRC/SRC} = \begin{bmatrix} 1 & 0 & 0 \\ 0 & 0 & 1 \\ 0 & -1 & 0 \end{bmatrix}$$

The 3-axis MEMS gyro contained inside the IMU ADIS16375 from the Analogue devices®, was used for the body angular rate measurements during the HIL testing. The mounting matrix for the IMU in the HIL-Demonstrator was also an identity matrix.

6.2.2 **Actuators Placement**

Three RW units and three magnetorquers were integrated in the HIL-Demonstrator as actuators. The large CubeWheel was used along the Z-axis of the BRC frame while 2 small CubeWheel units were used along the X- and the Y-axis. Each RW was placed such that its angular momentum vector is aligned with the respective BRC frame axis.

The X- and the Y-axis magnetorquers rods were placed on the HIL-Demonstrator in a 'T' configuration to avoid the mutual induction phenomenon among the rods. The polarity of the magnetorquers was tested with a compass before placing on the HIL-Demonstrator. The compass needle points in the direction of the magnetic field lines which originate from the north pole of the magnetic dipole and travel to the south pole. The magnetorquers were placed on the HIL-Demonstrator such that for a positive on-time command, the north pole of each magnetorquer should be in the positive direction of the respective BRC frame axis.

6.2.3 **Data Communication**

DVK90CAN1, a development kit for the AVR AT90CAN128 was used as the OBDH unit in the HIL-Demonstrator. The OBDH unit handled the system I^2C bus as the master, while the CubeSense, the magnetic control board and the 3x RW units were connected on the system bus as the slave devices. Moreover, the OBDH unit communicated with the IMU on the SPI interface and it interfaced with the test computer via a UART link through an XBee wireless module. Figure 6-9 illustrates the data communication protocols among the ADCS units in the HIL-Demonstrator.

The role of the OBDH unit in the HIL testing was to gather data from the sensors and to pass this data to the test computer through the XBee module. The test computer processed the sensors' data in the ADCS algorithms and generated the commands for the actuators. These

Stellenbosch University https://scholar.sun.ac.za

commands were then sent to the OBDH unit through the XBee shield and the OBDH unit passed it on to the magnetic and the wheel control boards on the I^2C system bus.

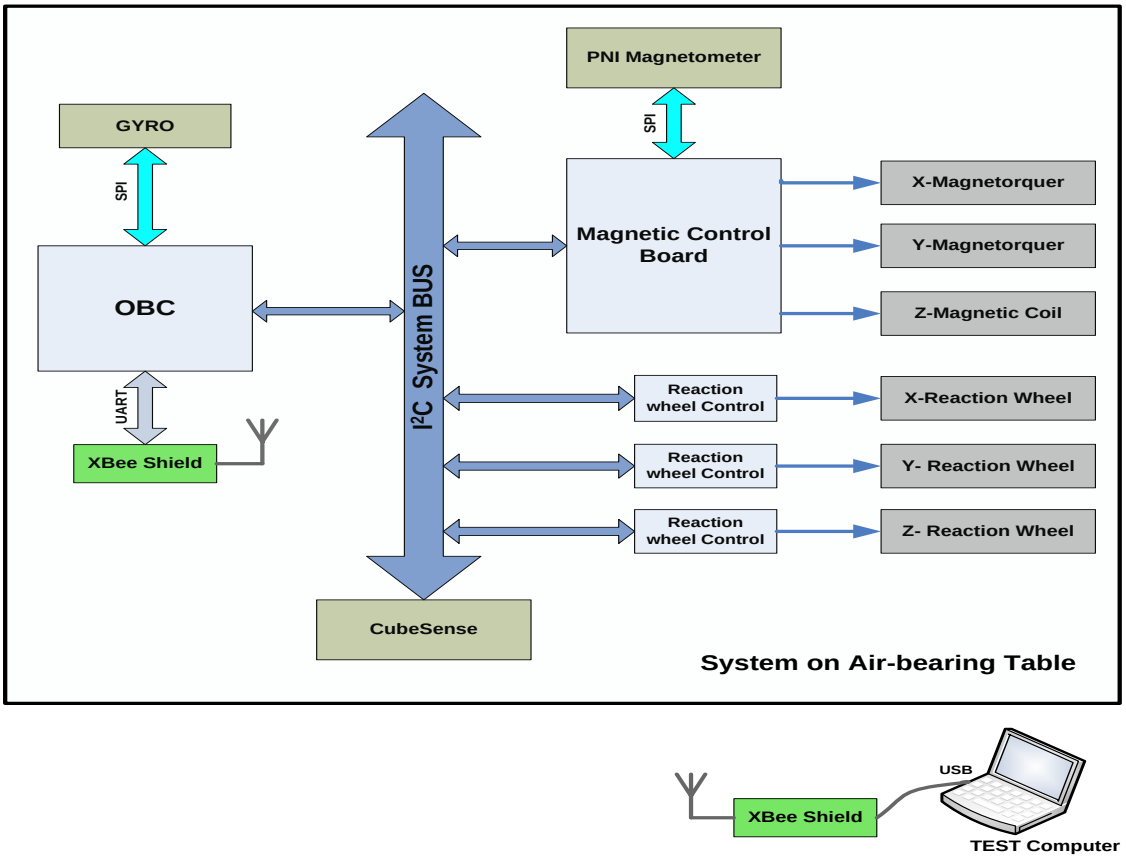

Telemetery Data Packet										
Packet Header	BXM	BYM	BZM	ω_{bx}	ω_{by}	ω_{bz}	ω_{RWX}	ω_{RWY}	ω_{RWZ}	CubeSense Data
4 bytes	4 bytes	4 bytes	4 bytes	2 bytes	2 bytes	2 bytes	2 bytes	2 bytes	2 bytes	5 bytes

Telecommand Data Packet					
MT_X ON Time	MT_Y ON Time	MT_Z ON Time	RW_X Speed Command	RW_Y Speed Command	RW_Z Speed Command
1 byte	1 byte	1 byte	2 bytes	2 bytes	2 bytes

Figure 6-9:Data communication among HIL-Demonstrator units

The telemetry packet sent from the OBDH unit to the test computer is shown in Figure 6-9. It consisted of 33 bytes of data which included: 4 bytes of packet header, 12 bytes of magnetometer data, 6 bytes of 3-axis rates from the gyro, 6 bytes of current angular speeds from the 3 reaction wheels, the CubeSense status byte and 4 bytes of CubeSense measurement data. During each control cycle, the commands for the actuators were sent to the OBDH from the test computer, in a telecommand packet of 9 bytes, which included 3 bytes of magnetorquer on-times and 6 bytes of speed commands for the 3 RW units.

Stellenbosch University https://scholar.sun.ac.za

6.2.4 **Power Interface**

A 3 cell Lithium Polyamide battery with 1000 mAh capacity was used as an on-board power supply for the HIL-Demonstrator. A small PCB of power voltage converter was designed for the HIL- Demonstrator, which contained the voltage regulator circuitry to convert the battery voltage levels to 3.3 V and 5 V.

6.3 Magnetometer Calibration

The magnetometer, RM3000, was calibrated for the sensitivity matrix and the offset vector inside the Helmholtz cage. The measurements of a high precision fluxgate magnetometer FVM400 from MEDA® were used as reference for the RM3000 calibration. The calibration setup included the magnetic control board to sample the RM3000 magnetometer and to send the 3-axis 32-bit raw magnetic field measurements to the test computer. The test computer also acquired the magnetic field data from the fluxgate magnetometer in micro-Tesla units.

$$Calibrated\ Magnetic\ Field_{\mu T} = Scale\ factor \times RM3000\ Readout\ Counts\ \pm Offsets$$

Two different calibration methods were implemented during the exercise. The details of these calibration methods are described in Appendix B. In the first method, the offset along each axis was determined by nullifying the magnetic field inside the cage and reading the RM3000 raw outputs. These offsets were then added or subtracted from the raw measurements of the RM3000 for bias compensation. Afterwards, the gain along the X-axis was determined by generating a constant magnetic field vector along the X-axis and then sliding the RM3000 upon the FVM400 such that the RM3000 raw readouts along the Y- and the Z-axis became less than 100 integer counts. The offset compensated raw X-measurements from the RM3000 were then divided by the applied magnetic field to get the scale factor or the gain along the X-axis. The gains along the Y- and the Z-axis were then determined by adopting the same procedure.

The RM3000 has 3 individual magnetic sensors along the three measurement axes to sense the 3-axis magnetic field vector. Ideally, these 3 magnetic sensors should be orthogonal to each other so that one magnetic field vector component may not affect the other magnetic field vector components. In this case, the sensitivity matrix would have zero off-diagonal elements. However, in a realistic scenario, due to manufacturing inaccuracies and the vibration loads during the satellite launch, the 3 sensors could not be perfectly orthogonal. In

Stellenbosch University https://scholar.sun.ac.za

this case, the sensitivity matrix will have non zero off-diagonal elements. The off-diagonal elements of the sensitivity matrix cannot be determined by the calibration method described as above. Therefore, a second calibration scheme was implemented to get a complete calibration model for the RM3000 including the off-diagonal elements of the sensitivity matrix as well.

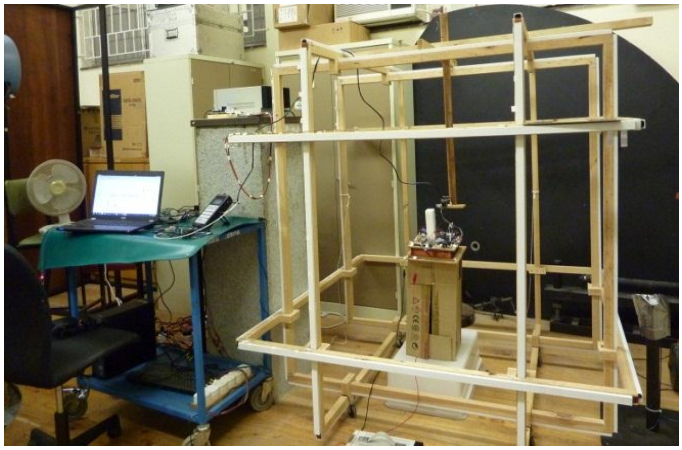

Figure 6-10: Magnetometer calibration setup

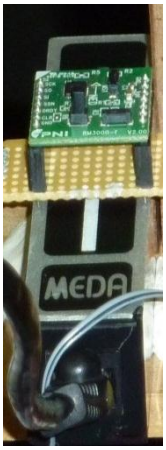

Figure 6-11: RM3000 and the reference magnetometer

In the second calibration method, the RM3000 magnetometer was placed on top of the FVM400 fluxgate magnetometer such that the measurement axes of both the magnetometers are aligned to each other. A controlled magnetic field was generated inside the Helmholtz cage following a reference, generated by an IGRF model. The test was run for three orbits and magnetic field measurements from the fluxgate magnetometer in micro-Tesla and the 3-axis raw outputs from the RM3000 were saved to a file. Subsequently, the Recursive Least Square (RLS) algorithm, described by Steyn [55], was applied on the experimental data to estimate the complete sensitivity matrix and the offset vector. Plots of the modelled and the calibrated magnetic field components for the RLS method are presented in Figure 6-12. The difference between the magnitudes of the reference and the calibrated magnetic field measurements during the calibration process is plotted in Figure 6-13. The calibration model determined by the two methods are described as follows,

Method1:

$$Calibrated\ Magnetic\ Field_{\mu T} = \begin{bmatrix} 0.02 & 0 & 0 \\ 0 & 0.02 & 0 \\ 0 & 0 & 0.0185 \end{bmatrix} \begin{bmatrix} Bx_{RM} \\ By_{RM} \\ Bz_{RM} \end{bmatrix} + \begin{bmatrix} -9.8675 \\ -1.6769 \\ 1.3642 \end{bmatrix}$$

Stellenbosch University https://scholar.sun.ac.za

Method2:

$$Calibrated\ Magnetic\ Field_{\mu T} = \begin{bmatrix} 0.0199 & 0.0001 & -0.0002 \\ -0.0005 & 0.0200 & 0.0001 \\ 0.0006 & 0.0010 & 0.0182 \end{bmatrix} \begin{bmatrix} Bx_{RM} \\ By_{RM} \\ Bz_{RM} \end{bmatrix} + \begin{bmatrix} -9.6918 \\ -1.3871 \\ 0.9583 \end{bmatrix}$$

Although the two calibration models produced results close to each other, the calibration model from method-2 was more comprehensive and was used during the HIL testing. The RMS errors for method-2 calculated over last 15000 seconds of the test are less than 0.1μT.

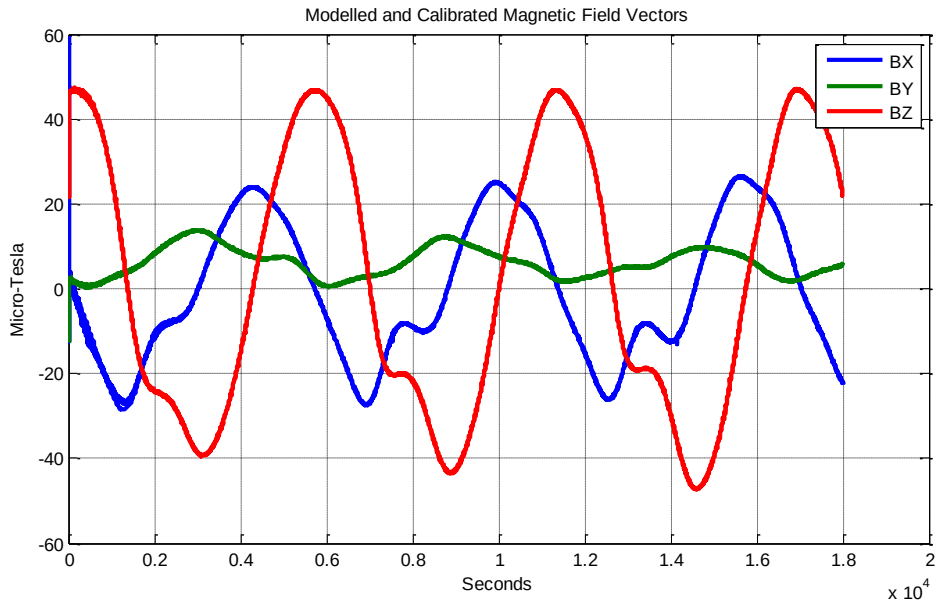

Figure 6-12:Modelled and the calibrated magnetic fields

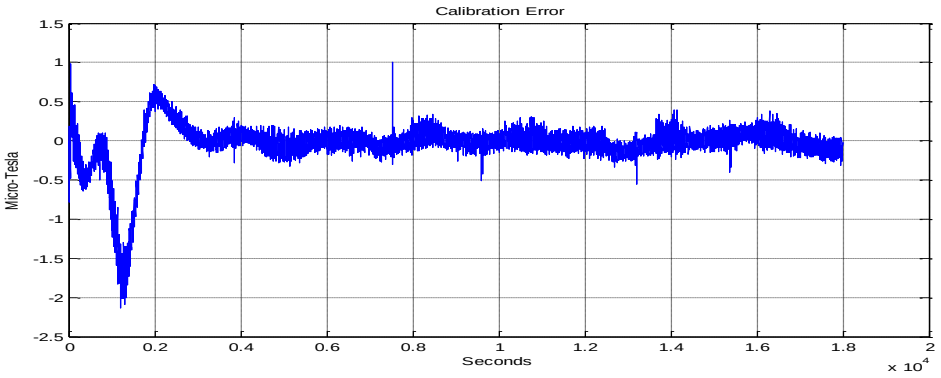

Figure 6-13: Calibration errors for the RLS method

Stellenbosch University https://scholar.sun.ac.za

6.4 HIL Test Scenarios

The HIL testing of the ADCS units was carried out in three phases. In the first phase, only the functionality of the magnetic controllers was tested. In the second stage, the RW based pointing control was tested and in the final stage, the momentum unloading controller was tested such that the RW keeps the commanded attitude and the magnetorquers perform the management of the angular momentum build-up over time. The MOI along the Z-axis, I_{zz}, was determined using Equation (6.1) during different test configurations. The Z-axis RW was spun at constant speed and the body rate along the Z-axis ω_{bz} was measured from the gyro.

$$I_{zz} = \frac{I_{wheel}\Delta\omega_{wheel}}{\Delta\omega_{bz}} \tag{6.1}$$

6.4.1 HIL Testing of the Magnetic Controllers

During the HIL testing of the magnetic controllers, the functionality of the rate damping magnetic controller and the stable spin magnetic controller were tested. Moreover, the magnetometer based RKF was also implemented and tested for the rate estimation during the stable spin mode. In the ADCS design of the project mission, the B-dot magnetic controller was used after separation from the launch vehicle to damp the body X and the Z-rates and to align the body Y-axis with the orbit normal. Afterwards, the Y-spin magnetic controller was activated along with the B-dot controller to spin the satellite along its Y-axis at the reference rate. However, on the air-bearing table, the motion along the Y- and the X-axis was physically restricted to 25° and the spin motion was only possible about the Z-axis. Therefore, the B-dot law was modified to align the body Z-axis to the Z-axis of the NED frame and damp the body rates along the X- and the Y-axis. The Z-spin controller, expressed in Equation (6.4) and (6.5), was implemented to spin the HIL-Demonstrator along the Z-axis at the commanded reference rate. The functionality of the Z-Spin and the Y-Spin controller is principally the same except that each controller utilizes a different set of magnetorquers. The B-dot control law implemented along the Z-axis is described by Equation (6.2) and Equation (6.3).

$$M_Z = K_D\dot{\beta} \tag{6.2}$$

Stellenbosch University https://scholar.sun.ac.za

where, β is defined as the angle between magnetic field vector and its Z-axis component.

$$\beta = cos^{-1}\left(\frac{B_Z}{\|\mathbf{B}\|}\right) \tag{6.3}$$

The Z-spin magnetic controller utilizes the X and the Y magnetorquers to spin the HIL-Demonstrator about the Z-axis. The Z-spin control law implemented on the test computer is described as follows,

$$M_X = K_S(\omega_{bz} - \omega_{bz-ref})\text{sgn}(B_y) \qquad \text{If } |B_y| \geq |B_x| \tag{6.4}$$

$$M_y = K_S(\omega_{bz-ref} - \omega_{bz})\text{sgn}(B_x) \qquad \text{If } |B_x| > |B_y| \tag{6.5}$$

The magnetic field vector inside the Helmholtz Cage was generated such that it had a 45° angle with respect to each axis of the NED frame and the strength of each vector component was set to 40μT. The HIL-Demonstrator placed on the air-bearing, was disturbed by an external tip-off torque to emulate a scenario similar to the satellite separation from the launch vehicle. The external impulse produced the rates along all three body axes. The B-dot rate damping controller was activated immediately to damp the body rates. The B-dot controller used the magnetic field readouts from the RM3000 magnetometer and commanded the Z-axis magnetorquer to damp the X and the Y rates. As evident from Figure 6-14, the B-dot magnetic controller successfully damped the initial body rates of -3.2°/s and -4.4°/s in the X- and the Y-axis respectively, to values less than 0.5°/s within 1200 seconds.

Once the X and the Y rates became less than 0.5°/s, the 'Magnetic Control Mode-2' was switched on. In this mode, the Z-spin controller was activated along with the B-dot controller. The Z axis magnetorquer coil was used to damp the X & Y body rates while the magnetorquer rods along the X- and the Y-axis were used to spin the HIL-Demonstrator along its Z-axis with a reference rate of -3°/s. The Z-spin magnetic controller successfully achieved the reference rate of -3°/s in approximately 150 seconds, which is evident from the Figure 6-14. The on-times for the magnetorquers during the Magnetic Control Mode-1 and Mode-2 are shown in Figure 6-15. Similar to the actual mission parameters, the magnetic control sample time was set to 10 seconds and the maximum on-time for the magnetorquers was limited to 8 seconds.

Stellenbosch University https://scholar.sun.ac.za

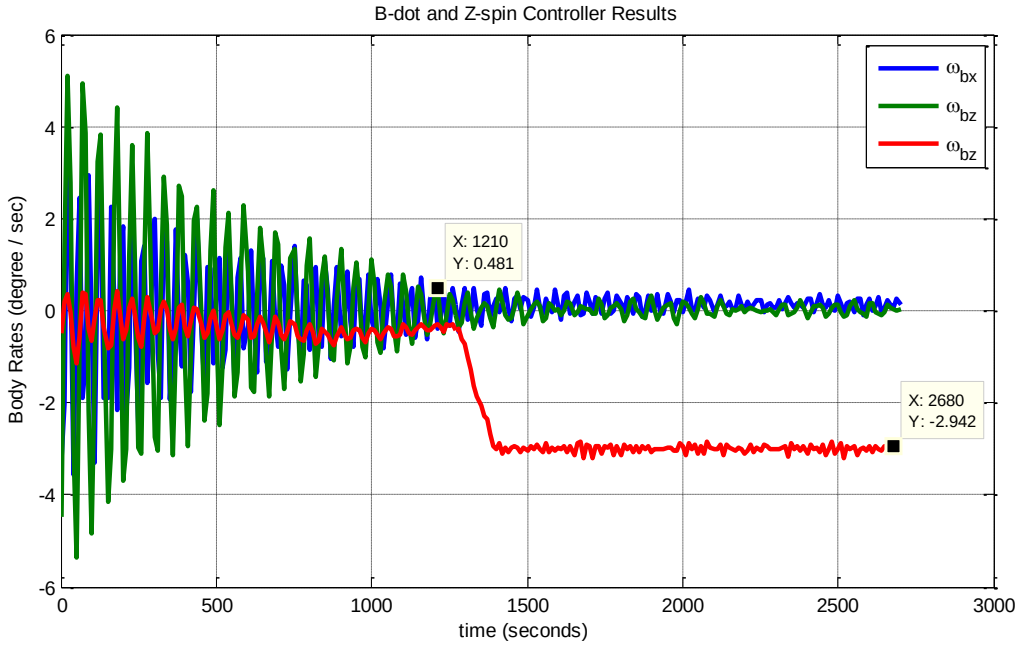

Figure 6-14: Test results for B-dot and Z-spin controllers

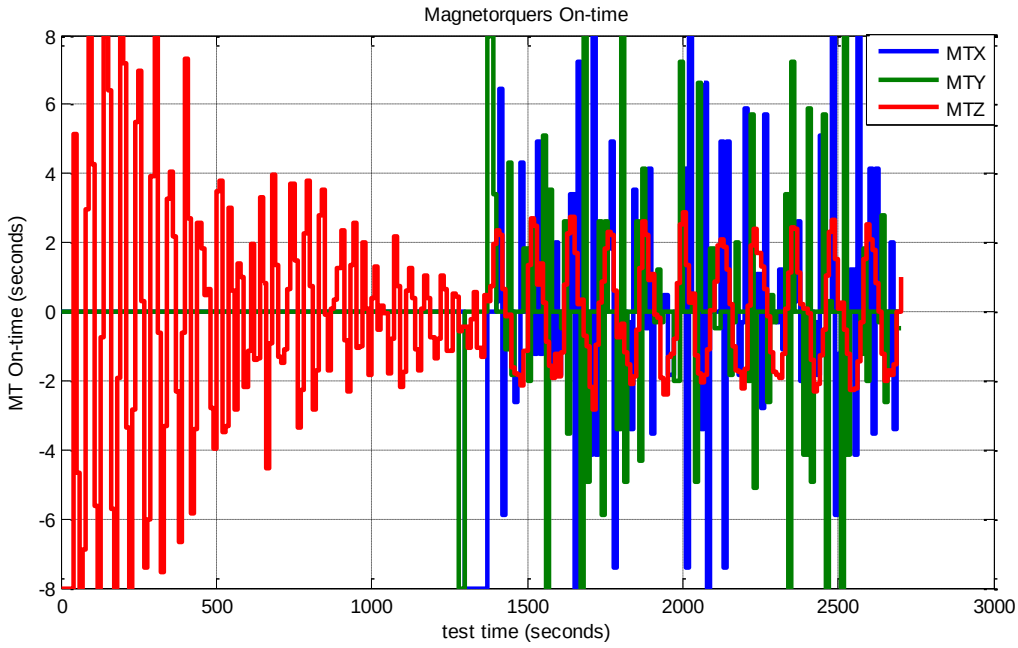

Figure 6-15: Signed on-times of the magnetorquers for B-dot and Z-spin controllers

The RKF was implemented during the HIL testing to estimate the Z-axis rate from the magnetometer readings. The test was started with initial conditions of near zero body rates and then the Z-Spin magnetic controller was activated to spin the HIL-Demonstrator. The

Stellenbosch University https://scholar.sun.ac.za

yaw rate outputs during the test were taken from the RKF estimates, as well as from the IMU. A few tests for different weight parameters of the **Q** and the **R** matrices and for different initial conditions were conducted. The best estimates obtained during the experimentations are shown in Figure 6-16. It is evident from the plots shown in Figure 6-16 that the RKF yaw rate estimates were comparable to the Gyro outputs during the test.

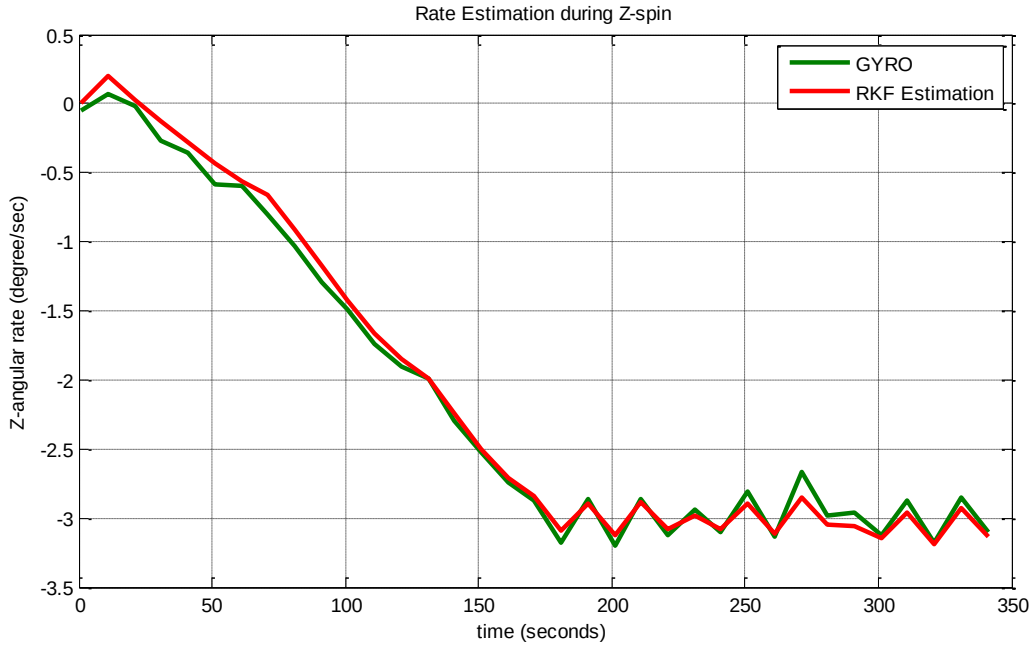

Figure 6-16: RKF performance during Z-spin

As discussed in Chapter 4, the gains of the magnetic controllers are tuned experimentally. Similarly, during the HIL testing; the gains were tuned experimentally by starting with an initial value, taken from the simulations. The objective of these tests was to validate the functionality of the magnetic controller with the designed magnetic control hardware and the software. Although, the HIL environment had some constraints, and was different from the space environment to an extent, the control law and its implementation on the magnetic control hardware was the same, in both the environments. Therefore, it can be concluded that the HIL test results of magnetic control had confirmed the successful operation of the magnetic controllers, the magnetic control hardware and the data exchange protocol between the designed magnetic control board and the OBC.

Stellenbosch University https://scholar.sun.ac.za

6.4.2 **HIL Testing of the RW Controllers**

In the HIL testing of the RW controllers, the quaternion feedback controller was implemented and tested on the air-bearing for pointing control along the yaw axis. In this HIL test scenario, two reference vectors were generated for the attitude determination, which included the magnetic field vector and the sun reference vector. The magnetic field vector was set to have a 45° angle with all three axes of the NED frame and the magnitude of each vector component was set to 40 μT inside the Helmholtz cage. The sun simulator was placed along the Y-axis of the NED frame such that it lies in the FOV of the CubeSense.

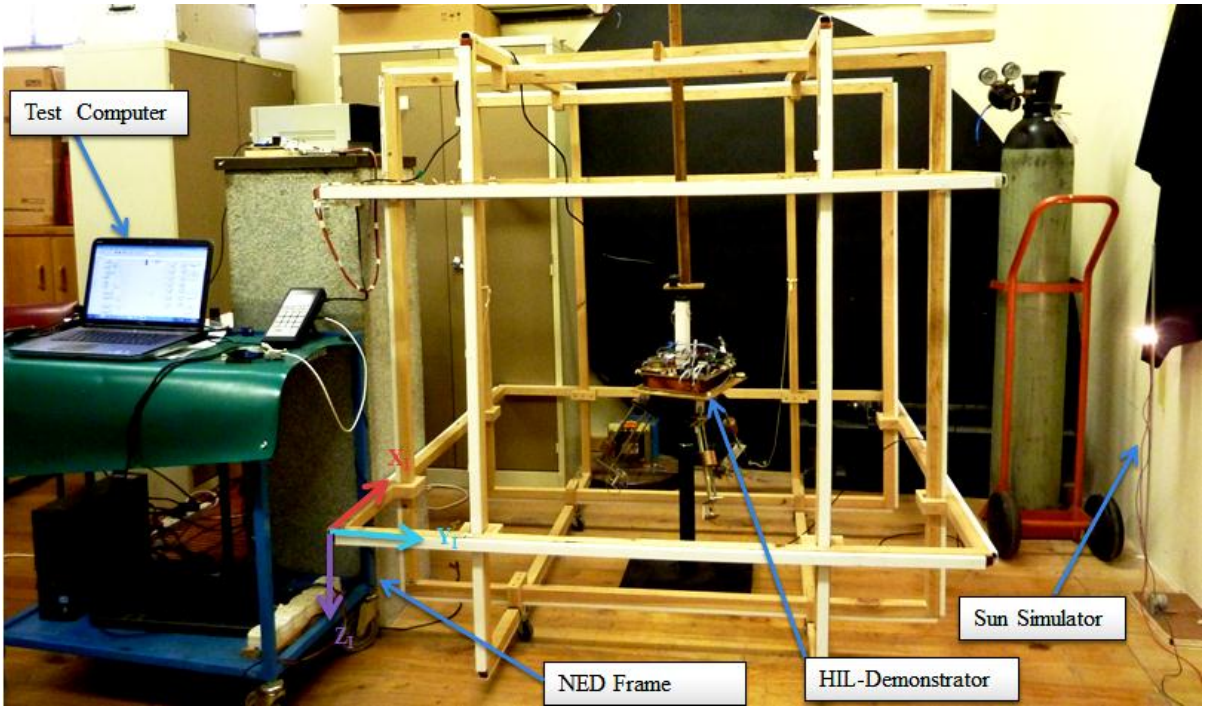

Figure 6-17: HIL test enviroment for RW pointing controllers testing

Before starting the test, the BRC frame was manually aligned with the NED frame and the two reference vectors were determined from the readouts of the magnetometer and the CubeSense. These two vectors were put in the TRIAD algorithm to form a reference TRIAD for the attitude determination.

In the ADCS design for the mission, three RW units were used to point the satellite to any desired attitude. However, in the HIL test scenario, the HIL-Demonstrator was only able to undergo the yaw manoeuvres, as the offset pointing in the roll and the pitch cannot be maintained due to the gravitational torques. The gravitational torques will saturate the X and the Y wheels very quickly. During the HIL testing of the wheel control, the large CubeWheel

Stellenbosch University https://scholar.sun.ac.za

along the Z-axis was used to perform the yaw manoeuvres and the small wheels, placed along the body X- and the Y axis, were used to damp the X and the Y rates.

The quaternion feedback controller expressed in Equation (4.65), was implemented for the yaw axis and is described by Equation (6.6). The gains of the quaternion feedback controller were determined from Equation (4.66), for a settling time of 20 seconds and were tuned during experimentation. The response to a 30° slew command is shown in Figure 6-18. The quaternion feedback controller pointed the HIL-Demonstrator to the desired yaw attitude and kept it within a window of ±0.2° after settling from a maximum overshoot of 0.5 ° (1.6%). The test cases with 15° , 25°, 45° and 60° step commands were also conducted to test the repeatibility and consistency of the controller performance.

$$N_{wheel-z} = K_P I_{zz} q_e(3) + K_D I_{zz} \omega_{bz} \tag{6.6}$$

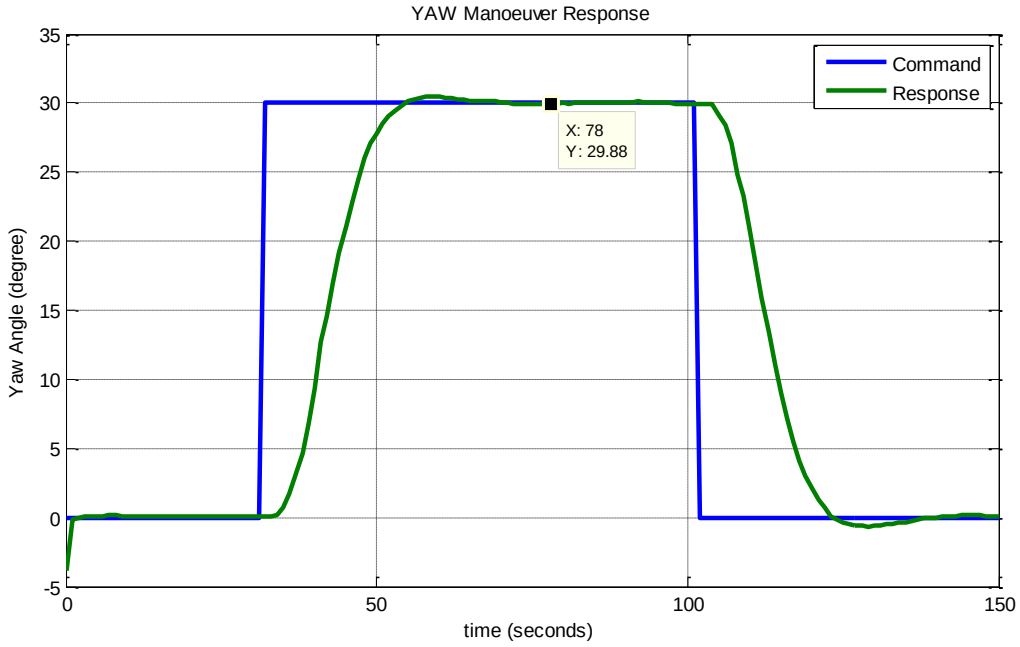

Figure 6-18: Respose to 30° yaw step

The angular rate feedback for the quaternion feedback PD controller was taken from the MEMS gyro, which is integrated in the IMU. The torque command from the quaternion feedback controller was converted to the speed command by using Equation (4.61) and (4.62). This speed command was then sent to the RW unit as a speed reference for the current control cycle. Figure 6-19 shows the Z-axis RW speeds during the 30° yaw manoeuvre test.

Stellenbosch University https://scholar.sun.ac.za

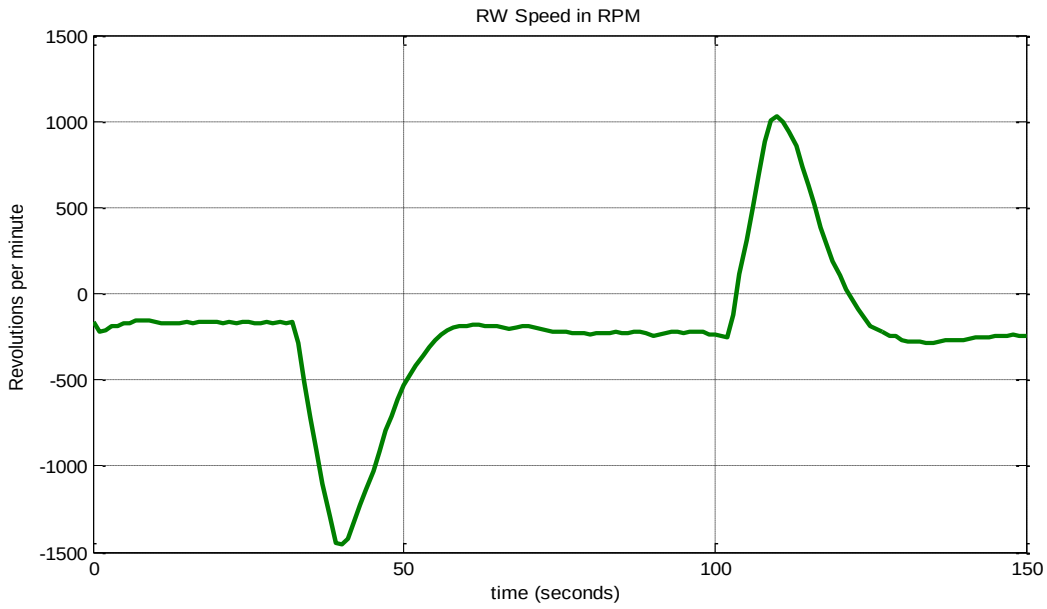

Figure 6-19 : Z-axis RW speed during yaw manoeuvre test

A simple propotional control was implemented to damp the X and the Y rates using the small CubeWheel units. Figure 6-20 shows the three axis body rates during the test and it is obvious from the figure that the body rates along the X- and the Y-axis were damped to values less than 0.11°/s during the test.

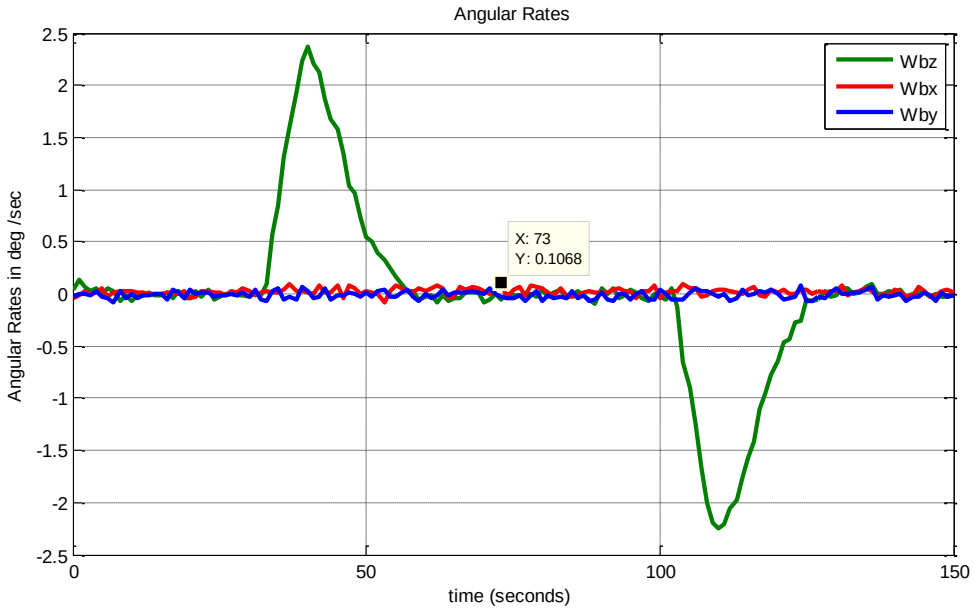

Figure 6-20: Three axis body rates during yaw manoeuvre test

The HIL testing of the RW control validated the design of the quaternion feedback controller and the RW speed controller. The design procedure for the quaternion feedback controller

Stellenbosch University https://scholar.sun.ac.za

and its implementation was similar to the actual mission, but for a single axis. The complete ADCS loop: sampling the sensors, attitude determination, generation of the torque command from the quaternion feedback controller, converting the torque command to the speed reference and finally transmitting it to the RW unit for implementation resembles the on-board ADCS scenario for RW control. The ADCS hardware configuration during this HIL test was almost the same as that of the actual mission, and this test verified the integrated functionality of CubeSense, the RM3000 magnetometer, the gyro, the I^2C communication bus and the RW units.

6.4.3 HIL Testing of the Momentum Unloading Controller

In the final stage of the HIL testing, the magnetic and the RW controller were combined together to create a more comprehensive scenario similar to an actual on-board ADCS operation. In this test, the HIL-Demonstrator was commanded to undergo a yaw manoeuvre of 25° and keep its orientation for 700 seconds as shown in Figure 6-21. For the first 350 seconds, only the RW control was activated. The Z-axis RW kept the yaw orientation, while the small CubeWheel units along the X- and the Y-axis damped the rates along their respective axes. The disturbance torques on the air-bearing platform due to the air friction and the ball surface imperfections caused the wheel angular momentum to build up. In 350 seconds, the Z axis RW speed increased from a near zero value to 350 rpm in order to compensate for the disturbance torques. After 350 seconds, the cross-product magnetic controller for momentum unloading was enabled. The cross-product controller dumped the angular momentum of the wheel in almost 50 seconds and kept it near zero for the next 300 seconds as evident from Figure 6-22. The wheel control law during this test was the same as described by Equation (6.6). The cross- product magnetic control law for 3-axis angular momentum unloading is expressed in Equation (4.58). This expression was modified to be used for single wheel angular momentum unloading. This modified expression is implemented for the momentum unloading during the test and is described by Equation (6.7) and (6.8). The on-times commands from the magnetic controller are plotted in Figure 6-23.

$$M_X = -\frac{K_W}{\|B\|}\left(B_y h_{wheel-z}\right) \tag{6.7}$$

$$M_Y = -\frac{K_W}{\|B\|}\left(-B_x h_{wheel-z}\right) \tag{6.8}$$

Stellenbosch University https://scholar.sun.ac.za

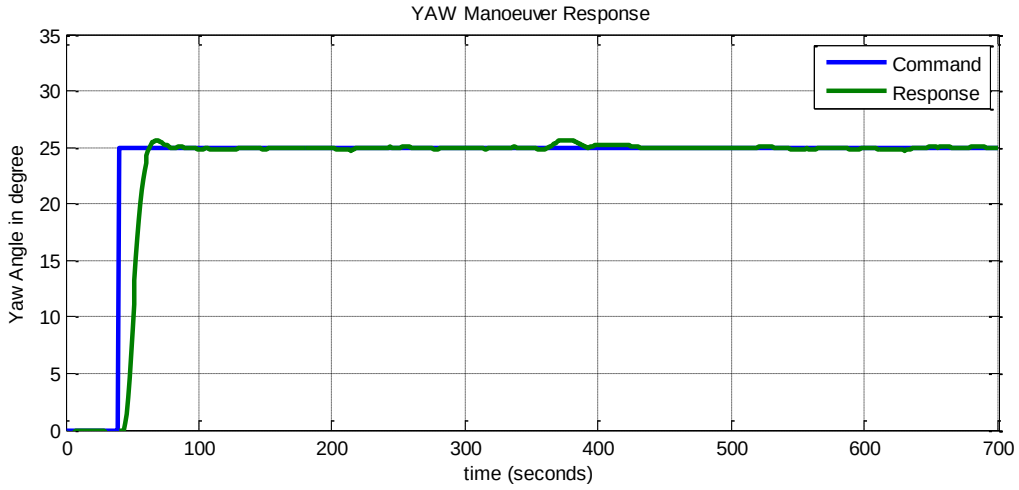

Figure 6-21: Offset yaw pointing during test-3

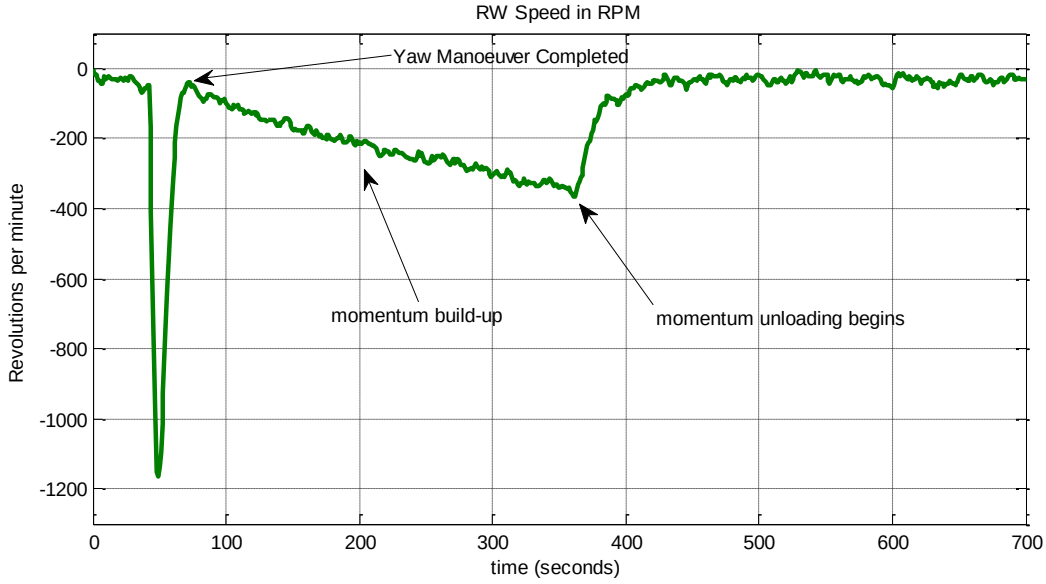

Figure 6-22: Z-axis RW angular speed during test-3

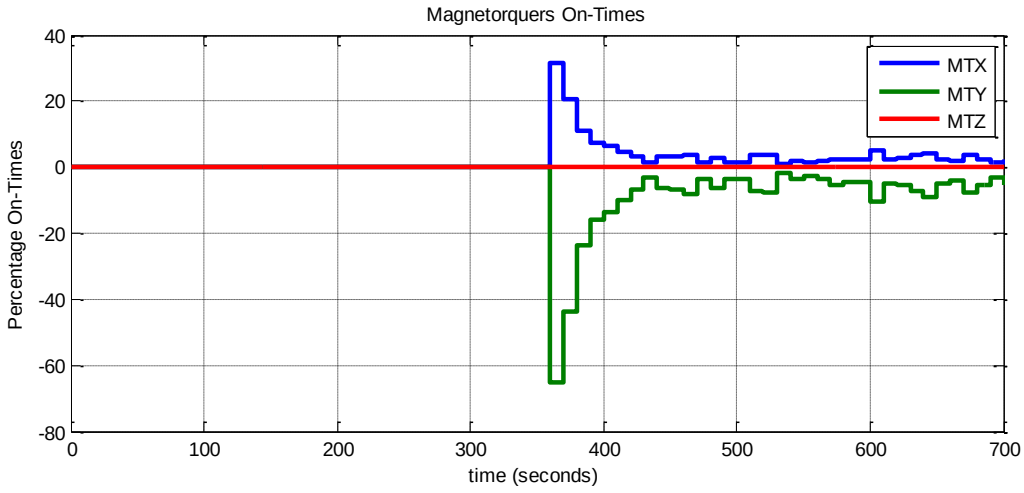

Figure 6-23: Signed on-times of the magnetorquers of magnetorquers during test-3

Stellenbosch University https://scholar.sun.ac.za

K_W, the gain of the cross-product controller for momentum unloading, was tuned by experimentation. The higher value of K_W dumps the angular momentum more quickly and maintains the wheel speed near to zero. However, the magnetic torques for the higher value of the gain produces more disturbances for the pointing controller. The magnetic moments commands generated by the cross-product controller were converted to the magnetorquer on-times and were sent to the magnetic control board for implementation. Figure 6-23 shows the percentage on-times of magnetorquers for the test.

The results of the HIL test-3 validated the integrated operations of both the magnetic control and the RW control. All of the sensors and the actuators for the mission ADCS were part of the test, except the star camera and the horizon sensor. The HIL testing of the ADCS was concluded with this test. On the basis of the test results of the HIL experimentation, it can be concluded with confidence that the designed ADCS hardware in Chapter 3 performed satisfactorily, the communication links among the ADCS units is reliable and the design procedures and the implementation of the ADCS algorithms is validated.

6.5 Summary

The HIL testing of an integrated subset of the ADCS units was carried out on an air-bearing table. The HIL environment was comprised of a sun simulator and a Helmholtz cage. Prior to the HIL tests, the RM3000 magnetometer was calibrated for the sensitivity matrix and the offset vector. In the first stage of the HIL testing, the magnetic controllers and the RW controllers were tested separately in the HIL environment. During the magnetic control tests, the B-dot and the Z-spin controllers were successfully tested. Moreover, magnetometer based RKF was also implemented and tested successfully. During the HIL testing of the RW control, performance of the quaternion feedback controller was tested and verified. In the final stage of the HIL testing, a more comprehensive ADCS scenario was created such that the RW controllers kept the commanded pointing and the cross-product magnetic controller maintained the reference angular momentum. Conclusively, the HIL testing validated the functionality of a subset of the ADCS hardware, the software and the control algorithms in a restricted environment.

Stellenbosch University https://scholar.sun.ac.za

7. Research Conclusions

7.1 Conclusive Research Summary

The aim of the project was to develop and test the ADCS of a small satellite. The mission satellite considered for the project was a nanosatellite with a mass of 20 kg and carrying an imaging payload. The mission orbit was a 500 km altitude, near circular SSO and an LTAN of 10 am / 10 pm. The requirements for an ADCS design included a pointing accuracy of less than 0.05° RMS and a pointing stability of less than 0.005°/s RMS during the imaging mode. The testing of the designed ADCS included the simulations to verify the in-orbit performance and the HIL testing to confirm the functionality of the integrated ADCS units in an HIL environment.

The research work was divided into three phases. In the first phase, the ADCS hardware was selected and the required electronics was designed and developed. In the second phase of the project, the in-orbit performance was determined through simulations in Matlab Simulink environment with realistic ADCS models. Lastly, several of the ADCS algorithms were tested with a subset of the ADCS hardware units for their functionality in an HIL environment.

The sensors for attitude determination were selected on the basis of the pointing accuracy requirements for the mission. The required pointing knowledge derived from the pointing accuracy requirements demands the selection of a sensor with accuracy smaller than 0.03°. The CubeStar, a nano star tracker developed at ESL, was chosen as its specifications fulfil the pointing knowledge requirements. Magnetometer information was required for the magnetic rate damping controllers. The RM3000 from PNI® Corp., a magneto-inductive magnetometer was chosen for the project due to its power efficient technology. The technology has a space heritage from the QBX mission and is also less sensitive to temperature variations. Moreover, CubeSense, an integrated FSS and horizon sensor module was selected to be used for attitude determination during the nominal pointing modes. CubeSense has a wide FOV and has a flight heritage from QB50 precursor missions.

Stellenbosch University https://scholar.sun.ac.za

RW control was needed for the mission ADCS for fine pointing control and the magnetorquers were required for magnetic rate damping and RW momentum-unloading operations. The torque required by the RW units was determined from the agility requirements for the mission and the required angular momentum storage capacity was determined from the disturbance torques on the satellite. On the basis of these requirements, the large CubeWheel module from the ESL was selected to be used in the project mission. Similarly, the magnetic moment required from the magnetorquers was determined from the magnetic torque requirements during the eclipse period of the orbit for unloading the accumulated angular momentum. The magnetorquers units were designed and developed for the required magnetic moment with added margins.

Two PCB modules were designed and developed for the project namely; the magnetic control board and the RW control electronics. The magnetic control board samples the RM3000 magnetometer and drives the magnetorquers. The design included a highly power efficient MCU from Atmel® Pico-power series and a single miniature driver chip to drive all the three magnetorquers. The MCU software manages the magnetic control times and drives the magnetorquers during the first 80% part of the control cycle. During the remaining 20% part of the magnetic control period, the MCU samples the magnetometer. The RW control electronics designed for the project is a small PCB of dimensions 28 mm × 28 mm due to the assembly constraints in the RW unit. It contains an MCU to run the speed control algorithms, to sample the magnetic encoder and to communicate with the OBC on an I^2C interface. Moreover, the PCB contains an integrated driver chip with a miniature package of 4 mm × 4 mm, to run the BLDC motor. Two low pass filtration techniques were investigated to suppress the magnetic encoder noise and the one with better performance was adopted for the speed calculation algorithm. The RW dynamics were modelled in Simulink® and the parameters of the system model were evaluated. A state feedback integral controller was designed for speed control of the RW motor. The performance results of the speed controller met the 3 seconds designed settling time with 0.2 seconds error, which included the communication delay. The controller regulated the wheel speed at the commanded reference within a 3 rpm error band. The controller was designed for zero steady state error, but a 3 rpm error was resulted from the encoder noise.

The camera used as horizon sensor in CubeSense was chosen to be placed on the earth facing deck of the satellite body. Similarly, the boresight of the FSS camera was chosen to be

Stellenbosch University https://scholar.sun.ac.za

aligned with the –Y-axis of the BRC frame so that the sun is in its FOV during a nominal nadir pointing attitude. CubeStar was chosen to be placed on the +Y-facet of the satellite body having a 45° angle with the +Y-axis and the –Z-axis in the YZ plane of the BRC frame. The earth and the sun obstruction were analysed for this placement configuration for a 30° roll offset condition. The placement chosen for the X and the Y-axis magnetorquer rods was a T-shape configuration to avoid any mutually induced currents. Moreover, a 3-wheel configuration was chosen for the RW units for the mission ADCS for its simplicity of operation.

The satellite dynamics and kinematics models were developed in the Simulink environment. The gravity gradient and the magnetic disturbance torques were also modelled for the simulations. The RW model developed for the speed control design was embedded in the simulation environment. Similarly, the noise characterises of the selected ADCS sensors were considered for sensor models. An estimation block was developed for the simulations, which has implementations of the attitude determination algorithms including the TRIAD method, the RKF and the full-state EKF. Moreover, the magnetic controllers were implemented in a magnetic control block, which include the B-dot controller, the Y-spin controller and the cross-product magnetic controllers. The quaternion feedback RW controller was implemented for single wheel and three wheels configuration inside the RW control block.

The rate estimates from the EKF and the RKF, based on the magnetometer measurements were compared in an uncontrolled tumbling state with magnetometer measurements. Although, the EKF estimates were more accurate than the RKF for tumbling rates of $[-3\,,0.5\,,2]\ \mathrm{deg/s}$, the RKF was chosen to be used for rate estimation during the tumbling mode. The reason is that the RKF is more robust in performance with reduced computation load and can provide reliable estimates for the case of higher body rates. The RKF estimation errors in a controlled state were less than $0.14\ \mathrm{deg/s}$ during the simulations. The EKF estimates were used during the stable state with RW control activated. The attitude estimation errors for the EKF using the star camera updates were less than 12 arc-seconds and the rate estimations errors for the same configuration were less than 4 arc-seconds/second.

An event sequence was defined in the simulation environment to switch different ADCS configurations at different time intervals and brought the satellite from an uncontrolled

Stellenbosch University https://scholar.sun.ac.za

tumbling state to a three axis stabilized state. Starting from a tumbling state with body rates $[-3, 0.5, 2]$ deg/s , the B-dot controller was used to damp the body rates during the first orbit. At the start of the second orbit, the B-dot controller successfully brought the body rates in all three axes below 0.3 deg/s. Hereafter, the satellite was taken to a stable spin mode around the body Y-axis using the Y-spin magnetic controller. The RKF estimates were used for rate information during the Y-spin. Meanwhile, the EKF was initialized so that it may converge before switching on the RW control. The Y-wheel pitch control with magnetic nutation damping was activated to absorb the body angular momentum before transition to the three axis wheel control. The three axis wheel control modes include the target pointing imaging mode with star tracker updates and a nominal pointing mode. During the nominal pointing mode, the ADCS points the –Y facet of the satellite body towards the sun to generate maximum solar power. Whereas, during the eclipse period of the nominal mode, the satellite keeps the nadir pointing attitude and the magnetorquers are used to dump the accumulated wheel angular momentum. The RMS pointing accuracy during the imaging mode was less than 0.03° in all three axis and the maximum body rates during the imaging were less than 0.004 °/s. Hence, the ADCS design complied with the mission requirements.

In the third phase of the project, several of the ADCS algorithms were tested on the air-bearing table in the HIL environment. The Helmholtz cage system was used in the HIL test environment to emulate the magnetic field vector. Moreover, a sun simulator was also included in the test environment to emulate the sun vector for attitude determination. A subset of the ADCS hardware was integrated together for the HIL testing, which included the RM3000 magnetometer, the CubeSense, the IMU, 3x RW units, 3x magnetorquers and an OBDH module. Prior to the HIL tests, the RM3000 magnetometer was calibrated inside the Helmholtz cage for its sensitivity matrix and offset vector parameters. Two schemes were investigated and implemented for the magnetometer calibration. The calibration model determined from the recursive least square method was used during the HIL testing.

The functionality of the B-dot and the stable spin controller was tested during the first stage of the HIL testing. The RKF was also implemented and was tested to provide the estimated rates based on the magnetometer measurements. In the second stage of the HIL testing, the quaternion feedback RW controller was implemented for yaw pointing. A TRIAD estimator was used for attitude determination from the magnetometer and the FSS vector measurements. Two small CubeWheel modules were used to damp the rates in the pitch and

Stellenbosch University https://scholar.sun.ac.za

the roll. The RW pointing controller maintained the commanded yaw reference within a window of ± 0.2° during the test. In the final stage of the HIL testing, the magnetic and the RW controllers were tested simultaneously such that the RW controller keeps the commanded yaw reference and the cross-product magnetic controller dumps the angular momentum build-up during the test. The HIL testing validated the functionality of designed ADCS hardware, the communication protocols among the ADCS units and working of the ADCS algorithms in a test environment.

To conclude, the project can be regarded as successful. Starting from the mission requirements, the ADCS hardware was selected and the interface electronics was successfully designed, developed and tested. One of the outcomes of this work was a power efficient integrated RW electronics board, which can be regarded as a value addition to the CubeWheel module. The in-orbit performance of the mission ADCS was determined in a realistic simulation environment and the functionality of most of the ADCS algorithms were successfully tested on the ADCS hardware in an HIL environment. The HIL-Demonstrator, an HIL test platform, built for the HIL testing can be utilized for testing the ADCS of nanosatellites and also for educational and training purposes.

7.2 Recommendations

Some recommendations are hereby proposed for possible improvements in the design and test setup.

7.2.1 ADCS Hardware

Although the designed hardware electronics fulfils all the functional requirements, however a few design improvements are hereby proposed for the hardware design. Firstly, as the I^2C buffer is contained in the CubeComputer module, therefore it was not included in the RW electronics PCB. However, for a product perspective, it will be better to include the buffer in the RW electronics as well. This will ensure a reliable bus operation irrespective of the selected OBC. Secondly, the BLDC driver chip contains an on-chip 5 V linear regulator that was used to power the Hall sensors. For a modular design perspective, this scheme was more suitable. However, the voltage converter inefficiency would be less using an external 5 V regulated supply from the Power Subsystem for the Hall sensors, rather having the conversion losses in more than one place.

Stellenbosch University https://scholar.sun.ac.za

The RW system with the speed controller has one free integrator and the system is referred as type-1. For a type-1 system, a zero steady state is achieved for a step input. However, there is a constant steady state error for the case of a ramp input. Adding another integrator term in the controller will make the system type-2. The characteristic of a type-2 system is zero steady error for both the step and the ramp input cases. A type-2 controller for RW speed control can be implemented to get better performance for a ramp following case. This will also increase the ADCS performance for large angle manoeuvers as there will be no overshoot due to the RW speed controller.

7.2.2 **Redundancy for Reliability**

The components of a redundant magnetometer can be integrated in the magnetic control PCB that will improve the overall ADCS reliability index. The magnetic control PCB can also accommodate a redundant MCU and the magnetorquer driver electronics. This scheme will also increase the reliability without adding much complexity in the design.

The RW motor speed can also be determined by utilizing the Hall sensors signals. For the Large CubeWheel BLDC motor, 6 pulses per revolution can be obtained through XOR operation on the Hall sensor signals from the motor. Although, this resolution is not good for low speed operation, however, addition of this option in the circuitry can prevent total functionality loss in case of the magnetic encoder failure.

The addition of a redundant fourth RW in the tetrahedral or pyramid configuration can increase the reliability of the system and the ADCS can maintain stability and perform fine pointing even in the case of a single RW failure. In these configurations, the wheel will run at a bias speed, but the net angular momentum of the four wheel system remains zero. This also prevents the effects of motor non-linearity at near zero speeds.

7.2.3 **Test Facility**

A horizon simulator can be included in the HIL test facility to utilize the CubeSense horizon sensor module in the HIL test setup. In this regard, a circular light source with a radius equal to the earth disk radius, as seen by the satellite in its orbit can be used. This will simulate the illuminated earth surface from the reflected sunlight. The light source can be placed in the test facility with dark background for deep space emulation. The addition of horizon sensor in the test facility will increase the attitude determination accuracy during the HIL testing.

Stellenbosch University https://scholar.sun.ac.za

Bibliography

[1] R. Munakata, "CubeSat Design Specifications, Cal Poly SLO," January 2009. [Online]. Available: https://www.qb50.eu/index.php/tech-docs/category/13-extras?download=44:calpoly-cubesat-design-specification-rev-12. [Accessed 09 09 2015].

[2] D. DePasquale, "Nano/Microsatellite Launch Demand Assessment 2011," [Online]. Available: http://www.sei.aero/eng/papers/uploads/archive/SpaceWorks_NanoMicrosat_Launch_22Nov2011_revA.pdf. [Accessed 09 09 2015].

[3] "QB50: The project, Mission Objectives," June 2015. [Online]. Available: https://www.qb50.eu/index.php/project-description-obj/mission-objectives. [Accessed 07 06 2015].

[4] "Space Security 2011 Report," [Online]. Available: http://spacesecurityindex.org/2011/10/. [Accessed 09 09 2015].

[5] M. R. Greene, "The Attitude Determination and Control System of the Generic Nanosatellite Bus," Master's thesis, University of Toronto, 2009.

[6] B. T. Narheim and O. Olsen, "A Norwegian Satellite for Space-based Observations of AIS in the High North," in *21st Annual AIAA/USU Conference on Small Satellites.*, Logan-USA, 2007.

[7] G. d. Carufel, "Assembly, integration and thermal testing of the generic nanosatellite," Master's thesis, University of Toronto, 2009.

[8] K. A. Carroll and S. Rucinski, "Arc-Minute Nanosatellite Attitude Control: Enabling Technology for the BRITE Stellar Photometry Mission," in *18th Annual AIAA/USU Conference on Small Satellites*, 2004.

Stellenbosch University https://scholar.sun.ac.za

[9] "BRITE (BRIght-star Target Explorer) Constellation / BRITE Canada," 2015. [Online]. Available: https://directory.eoportal.org/web/eoportal/satellite-missions/b/brite-canada. [Accessed 09 09 2015].

[10] "CanX-4&5 Formation Flying Mission Accomplished," UTIAS/SFL, 5 November 2014. [Online]. Available: http://utias-sfl.net/?p=2191. [Accessed 09 09 2015].

[11] C. R. Boshuizen and J. Mason, "Results from the planet lab flock constellation," in *28th Annual AIAA/USU Conference on Small Satellites*, 2014.

[12] "Gunter's space page," [Online]. Available: http://space.skyrocket.de/doc_sdat/flock-1.htm. [Accessed 09 09 2015].

[13] "Dove 1 Satellite Technical Description," Cosmogia Inc., [Online]. Available: https://apps.fcc.gov/els/GetAtt.html?id=121393&x=.. [Accessed 09 09 2015].

[14] W. Marshall and C. Boshuizen, "Planet Labs' Remote Sensing Satellite System," CubeSat Developers Workshop Logan,Utah," 30 August 2013. [Online]. Available: http://digitalcommons.usu.edu/smallsat/2013/all2013/7/. [Accessed 09 09 2015].

[15] "Successful Launch of University of Tokyo's Nano-satellite "PRISM" and Its First Voice from Kiruna Ground Station," 23 January 2009. [Online]. Available: http://www.spacemaster.eu/attach/Current/2009_03_20_PRISM_press_release.pdf. [Accessed 09 09 2015].

[16] T. Inamori and K. Shimizu, "Attitude Stabilization for the Nano Remote Sensing Satellite PRISM." *JOURNAL OF AEROSPACE ENGINEERING © ASCE*, JULY 2013.

[17] Yuya Nakamura and R. Funase, "Extensible Boom-Based Optical System for Nano-Scale Remote Sensing Satellite "PRISM"," in *19th Annual AIAA/USU Conference on Small Satellites*, 2005.

[18] S. Arnold and J. Armstrong, "QbX-The CubeSat Experiment," in *26th Annual AIAA/USU Conference on Small Satellites*, Logan-USA, 2012.

Stellenbosch University https://scholar.sun.ac.za

[19] J. Armstrong and C. Casey, "Pointing Control of Low Altitude Triple CubeSat Space Darts," in *23rd Annual AIAA/USU Conference on Small Satellites*, Logan-USA, 2009.

[20] J. L. Schwartz, M. A. Peck and D. C. Hall, "Historical Review of Air-Bearing Spacecraft Simulators," *Journal of Guidance,Control, and Dynamics*, Vols. 26, No. 4, July–August 2003.

[21] M. Poppenk and R. Amini, "Design and Application of a Helmholtz Cage for Testing Nano-Satellites, Esa-Estec," in *6th International Symposium on Environmental Testing for Space Programmes*, 2007.

[22] S. Wassom and Q. Young, "Integrated Test Facility for Nanosat Assessment and Verification," in *10th Annual CubeSat Developers Workshop, American Institute of Aeronautics and Astronautics*, 2013.

[23] M. K. Prinkey and D. W. Miller, "Merritt 4-Coil per Axis Helmholtz Cage and Spherical Air Bearing," in *AIAA Guidance, Navigation, and Control Conference. In: CubeSat Attitude Control Testbed Design: . American Institute of Aeronautics and Astronautics.* 2013.

[24] M. K. Quadrino, "Testing the Attitude Determination and Control of CubeSat with Hardware-in-the-Loop," Master's Thesis, MIT, 2014.

[25] G. Janse van Vuuren, "The Design of a Helmholtz Cage Geomagnetic Field Emulator for CubeSat Application," Project Report submitted to Stellenbosch University, November 2012.

[26] C. Simone and O. Perez, "A Dynamic, Hardware-in-the-Loop, Three-Axis Simulator of Spacecraft Attitude Maneuvering With Nanosatellite Dimensions." *Journal of Small Satellites*, Vol. 4 , No.1, p.315..

[27] J. Wertz, *Spacecraft Attitude Determination and Control*, Kluwer Academic Publishers, 1991.

Stellenbosch University https://scholar.sun.ac.za

[28] W. Bong, *Space Vehicle Dynamics and Control*, AIAA, Second Edition-2008.

[29] W. H. Steyn, *Lecture Slides:Satellite Systems Course*, Stellenbosch University, 2014.

[30] G. Janse van Vuuren, "The Design and Simulation Analysis of an Attitude Determination and Control System for a Small Earth Observation Satellite," Master's thesis at Stellenbosch University, March 2015.

[31] J. Engelbrecht, " Hardware-in the Loop Simulation Facility for the Attitude Determination and Control System of SUNSAT," Master's thesis at Stellenbosch University, December 1999.

[32] J. Wertz, *Space Mission Engineering, The New SMAD*, Space Technology Library, 2011.

[33] B. Udrea and M. Nayak , "Analysis of the Pointing Accuracy of a 6U CubeSat Mission for Proximity Operations and Resident Space Object Imaging," in *5th International Conference on Spacecraft Formation Flying Missions and Technologies*,2013.

[34] C. D. Hall, "AOE 4140 : Spacecraft Dynamics and Control," 2003. [Online]. Available: http://www.dept.aoe.vt.edu/~cdhall/courses/aoe4140/attde.pdf.

[35] "User Manual: RM3000-f Evaluation Board, 3-Axis Geomagnetic Sensor Module," [Online].Available: http://www.willow.co.uk/html/components/com_virtuemart/shop_image/product/Heading/pdfs/MSHEP0007.pdf. [Accessed 07 09 2015].

[36] W. H. Steyn, "Attitude control Actuators, Sensors and Algorithms for a Solar Sail CubeSat," in *62th International Astronautical Congress*, Cape Town , 2011.

[37] "CubeSense: Fine Sun and Nadir Sensor, specification sheet," CUBE Space®, [Online]. Available: http://www.isispace.nl/brochures/CubeSense_Brochure%20CubeSpace.pdf. [Accessed 09 09 2015].

Stellenbosch University https://scholar.sun.ac.za

[38] “CubeStar: Nano Star Tracker, specification sheet,” CubeSpace, [Online]. Available: info@cubespace.co.za.

[39] “STIM IMU datasheet,” sensoror® Corp., [Online]. Available: www.sensonor.com/media/91313/ts1524.r8%20datasheet%20stim300.pdf. [Accessed 07 09 2015].

[40] “CubeComputer specification sheet,” CUBE Space®, [Online]. Available: http://www.isispace.nl/brochures/CubeComputerV3_Brochure%20CubeSpace.pdf. [Accessed 09 09 2015].

[41] “Atmel: Technologies, Low Power,” Atmel Corporation, [Online]. Available: http://www.atmel.com/technologies/lowpower/. [Accessed 09 09 2015].

[42] “CubeWheel:, specification sheet,” CUBE Space®, [Online]. Available: http://www.isispace.nl/brochures/CubeWheel_Brochure%20CubeSpace.pdf.

[43] “LV8827LFQA Datasheet , ON Semiconductor,” [Online]. Available: http://www.onsemi.com/pub_link/Collateral/ENA2058-D.PDF. [Accessed 09 09 2015].

[44] “FAULHABER Brushless DC-Micromotors,” [Online]. Available: https://fmcc.faulhaber.com/resources/img/EN_2610_B_DFF.PDF. [Accessed 09 09 2015].

[45] J. Gerber, “Nano-Reaction wheel for CubeSat applications,” Project Report submitted to Stellenbosch University, December 2010.

[46] W. H. Steyn, *Class Notes for Control Systems-414,* Stellenbosch University, 2014.

[47] “AS5505 Low Power 12-Bit Magnetic Rotary Encoder, Datasheet,” [Online]. Available: http://ams.com/ger/content/download/383163/1241077/.../AS5055.../320895. [Accessed 09 09 2015].

[48] W. H. Steyn, *Course Material: ”Advanced ADCS Course,* Stellenbosch University,

Stellenbosch University https://scholar.sun.ac.za

2014.

[49] H. Black, "A Passive System for Determining the Attitude of a Satellite." *AIAA Journal*, vol. 2, no. 7, pp. 1350 – 1351, 1964..

[50] I. Bar-Itzhack, "Optimized TRIAD Algorithm for Attitude Determination." *Journal of Guidance, Control and Dynamics*, vol. 20, no. 1, pp. 208 – 211, 1997.

[51] R. Kalman, "A New Approach to Linear Filtering and Prediction Problems." *Journal of Fluids Engineering*, vol. 82, pp. 35 – 45, March 1960.

[52] R. Kalman and R. S. Bucy, "New Results in Linear Filtering and Prediction Theory." *Journal of Fluids Engineering*, vol. 83, pp. 95 – 108, March 1961.

[53] F. Martel, P. K. Pal and M. Psiaki, "Active Magnetic Control System for Gravity Gradient for Gravity Gradient Stablized Spacecraft," in *2nd Anuual AIAA/USU Conference on small satellites*, September,1988.

[54] W. T. Thomson, "Spin Stabilization of Attitude against Gravity Torque." *Journal of Astronautical Science*, No. 9, pp.31-33, 1962.

[55] W. H. Steyn, "A Multi-Mode Attitude Determination and Control System for Small Satellites," PhD Dissertation, Stellenbosch University, 1995.

[56] B. Wie, H. Weiss and A. Arapostathis, "Quaternion Feedback Regulator for Spacecraft Eigenaxis Rotations." *Journal of Guidance, Control, and Dynamics*, vol. 12, no. 3, May – June.

[57] J. Auret, "Design of an Aerodynamic Attitude Control System for a CubeSat," Master's thesis, Stellenbosch University, March 2012.

[58] C. Finlay. (2011, Nov.) International Geomagnetic Reference Field. International Assosiation of Geomagnetism and Aeronomy, [Online]. Available: http://www.ngdc.noaa.gov/IAGA/vmod/igrf.html.

Stellenbosch University https://scholar.sun.ac.za

[59] X. Chen, W. H. Steyn and Y. Hashida, “Ground-Target Tracking Control of Earth-Pointing Satellites,” in *Proceedings AIAA-2000-4547, Guidance, Navigation, and Control Conference and Exhibit*, pp. 1–11. AIAA, 2000.

Stellenbosch University https://scholar.sun.ac.za

Appendix A. The Extended Kalman filter Derivations

The mathematical derivations for the system state perturbation matrix $\mathbf{F}_t$ of the Extended Kalman Filter are presented in this section [30, 57].

i- State Perturbation Matrix

As mentioned in Section 4.1.3, the state vector in the EKF comprises of the inertial angular rates vector and the attitude quaternions vector

$$\mathbf{x}_t = \begin{bmatrix} \boldsymbol{\omega}_{BI} \\ \mathbf{q}_t \end{bmatrix} \tag{A.1}$$

The state perturbation matrix as defined under Equation (4.28) is

$$\mathbf{F_t} = \mathbf{F}\{\hat{\mathbf{x}}_t, t\} = \left[\frac{\partial \mathbf{f}}{\partial \mathbf{x}}\right]_{\mathbf{x_t}=\hat{\mathbf{x}}_t} \tag{A.2}$$

where,

$$\mathbf{f}\{\mathbf{x_t}, t\} \approx \dot{\mathbf{x}}_t \tag{A.3}$$

$$\mathbf{f}\{\mathbf{x_t}, t\} \approx \begin{bmatrix} \dot{\boldsymbol{\omega}}_{BI} \\ \dot{\mathbf{q}}_t \end{bmatrix} \tag{A.4}$$

The angular acceleration in Equation (A.4) can be determined by the Euler dynamic equation.

$$\dot{\omega}_{xi} = I_{xx}^{-1}\left(N_x + GG\left(I_{zz} - I_{yy}\right)A_{33}A_{23} + \left(I_{yy} - I_{zz}\right)\omega_{yi}\omega_{zi} - \omega_{yi}h_{wz} + \omega_{zi}h_{wy}\right) \tag{A.5}$$

$$\dot{\omega}_{yi} = I_{yy}^{-1}\left(N_y + GG(I_{xx} - I_{zz})A_{33}A_{13} + (I_{zz} - I_{xx})\omega_{xi}\omega_{zi} - \omega_{zi}h_{wx} + \omega_{xi}h_{wz}\right) \tag{A.6}$$

$$\dot{\omega}_{zi} = I_{zz}^{-1}\left(N_z + GG\left(I_{yy} - I_{xx}\right)A_{13}A_{23} + \left(I_{xx} - I_{yy}\right)\omega_{xi}\omega_{yi} - \omega_{xi}h_{wy} + \omega_{yi}h_{wx}\right) \tag{A.7}$$

where, '*GG*' denotes the constant term in the gravity gradient expression given by Equation (2.20). I_{xx}, I_{yy} and I_{zz} represent the MOI around X-, Y- and Z-axis respectively. The torques represented by $\mathrm{N_x}, \mathrm{N_y}$ and $\mathrm{N_z}$, are the cumulative control and the disturbance torques along the respective axis, excluding the gravity gradient torques.

Stellenbosch University https://scholar.sun.ac.za

The kinematics model was described by the Equation (2.16) and the quaternion rates in Equation (A.4) can be written as

$$\begin{bmatrix} \dot{q}_1 \\ \dot{q}_2 \\ \dot{q}_3 \\ \dot{q}_4 \end{bmatrix} = 0.5 \begin{bmatrix} q_4 & -q_3 & q_2 \\ q_3 & q_4 & -q_1 \\ -q_2 & q_1 & q_4 \\ -q_1 & -q_2 & -q_3 \end{bmatrix} \begin{bmatrix} \omega_{xi} + A_{12}\omega_o \\ \omega_{yi} + A_{22}\omega_o \\ \omega_{zi} + A_{32}\omega_o \end{bmatrix} \tag{A.8}$$

The state perturbation matrix $\mathbf{F_t}$ can be derived by partially differentiating the system matrix of Equation (A.4) with respect to the state vector given by Equation (A.1)

$$\mathbf{F_t} = \mathbf{F}\{\hat{\mathbf{x}}_t, t\} = \left[\frac{\partial \mathbf{f}}{\partial \mathbf{x}}\right]_{\mathbf{x_t}=\hat{\mathbf{x}}_t}$$

$$= \begin{bmatrix} \mathbf{F}_{11} & \mathbf{F}_{12} \\ \mathbf{F}_{21} & \mathbf{F}_{22} \end{bmatrix} \tag{A.9}$$

with,

$$\mathbf{F_{11}} = \left[\frac{\partial \dot{\boldsymbol{\omega}}_{BI}}{\partial \boldsymbol{\omega}_{BI}}\right]_{\mathbf{x_t}=\hat{\mathbf{x}}_t}$$

$$= \begin{bmatrix} 0 & \dfrac{\left((I_{yy} - I_{zz})\hat{\omega}_{zi} - h_{wz}\right)}{I_{xx}} & \dfrac{\left((I_{yy} - I_{zz})\hat{\omega}_{yi} + h_{wy}\right)}{I_{xx}} \\ \dfrac{\left((I_{zz} - I_{xx})\hat{\omega}_{zi} + h_{wz}\right)}{I_{yy}} & 0 & \dfrac{\left((I_{zz} - I_{xx})\hat{\omega}_{xi} - h_{wx}\right)}{I_{yy}} \\ \dfrac{\left((I_{xx} - I_{yy})\hat{\omega}_{yi} - h_{wy}\right)}{I_{zz}} & \dfrac{\left((I_{xx} - I_{yy})\hat{\omega}_{xi} + h_{wx}\right)}{I_{zz}} & 0 \end{bmatrix} \tag{A.10}$$

and

$$\mathbf{F_{12}} = \left[\frac{\partial \dot{\boldsymbol{\omega}}_{BI}}{\partial \mathbf{q}}\right]_{\mathbf{x_t}=\hat{\mathbf{x}}_t} \tag{A.11}$$

Stellenbosch University https://scholar.sun.ac.za

$$\mathbf{F}_{12} = \begin{bmatrix} 6\omega_o^2\alpha & 0 & 0 \\ 0 & 6\omega_o^2\beta & 0 \\ 0 & 0 & 6\omega_o^2\gamma \end{bmatrix} [\mathbf{d}_1 \quad \mathbf{d}_2 \quad \mathbf{d}_3 \quad \mathbf{d}_4] \tag{A.12}$$

with,

$$\mathbf{d}_1 = [-\hat{q}_1 A_{23} + \hat{q}_4 A_{33} \qquad -\hat{q}_1 A_{13} + \hat{q}_3 A_{33} \qquad \hat{q}_3 A_{23} + \hat{q}_4 A_{13}]^T$$

$$\mathbf{d}_2 = [-\hat{q}_2 A_{23} + \hat{q}_3 A_{33} \qquad -\hat{q}_2 A_{13} - \hat{q}_4 A_{33} \qquad -\hat{q}_4 A_{23} + \hat{q}_3 A_{13}]^T$$

$$\mathbf{d}_3 = [\hat{q}_3 A_{23} + \hat{q}_2 A_{33} \qquad \hat{q}_3 A_{13} + \hat{q}_1 A_{33} \qquad \hat{q}_1 A_{23} + \hat{q}_2 A_{13}]^T$$

$$\mathbf{d}_4 = [\hat{q}_4 A_{23} + \hat{q}_1 A_{33} \qquad \hat{q}_4 A_{13} - \hat{q}_2 A_{33} \qquad -\hat{q}_2 A_{23} + \hat{q}_1 A_{13}]^T$$

$$\alpha = \frac{I_{zz} - I_{yy}}{I_{xx}}, \qquad \beta = \frac{I_{xx} - I_{zz}}{I_{yy}}, \qquad \gamma = \frac{I_{yy} - I_{xx}}{I_{zz}}$$

Similarly,

$$\mathbf{F}_{21} = \left[\frac{\partial \dot{\mathbf{q}}_{BI}}{\partial \boldsymbol{\omega}}\right]_{\mathbf{x}_t = \hat{\mathbf{x}}_t} \tag{A.13}$$

$$= 0.5 \begin{bmatrix} \hat{q}_4 & -\hat{q}_3 & \hat{q}_2 \\ \hat{q}_3 & \hat{q}_4 & -\hat{q}_1 \\ -\hat{q}_2 & \hat{q}_1 & \hat{q}_4 \\ -\hat{q}_1 & -\hat{q}_2 & -\hat{q}_3 \end{bmatrix} \tag{A.14}$$

and,

$$\mathbf{F}_{22} = \left[\frac{\partial \dot{\mathbf{q}}_{BI}}{\partial \mathbf{q}}\right]_{\mathbf{x}_t = \hat{\mathbf{x}}_t} \tag{A.15}$$

$$= 0.5\boldsymbol{\Omega} + \omega_o \begin{bmatrix} \hat{q}_1\hat{q}_3 & \hat{q}_1\hat{q}_4 & (1 - \hat{q}_1{}^2) & -\hat{q}_1\hat{q}_2 \\ \hat{q}_2\hat{q}_3 & \hat{q}_2\hat{q}_4 & -\hat{q}_1\hat{q}_2 & (1 - \hat{q}_2{}^2) \\ (\hat{q}_3{}^2 - 1) & \hat{q}_3\hat{q}_4 & -\hat{q}_1\hat{q}_3 & -\hat{q}_2\hat{q}_3 \\ \hat{q}_3\hat{q}_4 & (\hat{q}_4{}^2 - 1) & -\hat{q}_1\hat{q}_4 & -\hat{q}_2\hat{q}_4 \end{bmatrix} \tag{A.16}$$

where, $\boldsymbol{\Omega}$ matrix is given in Equation (2.17). The computation of the state perturbation matrix is concluded here [30, 57].

Stellenbosch University https://scholar.sun.ac.za

Appendix B. The Magnetometer Calibrations

i- Scheme-I

In the first scheme, the RM3000 magnetometer was calibrated by applying a constant magnetic field vector inside the Helmholtz Cage. The offset vector and the sensitivity matrix were determined by following the steps mentioned as below

$$Calibrated\ Magnetic\ Field_{\mu T} = Scale\ factor \times RM3000\ Readout\ Counts\ \pm Offsets$$

1. Set the magnetic field inside Helmholtz cage to [0 0 0] and acquire the 3-axis readouts of the RM3000 magnetometer. These outputs correspond to the offset values along each axis
2. Compensate the offset values for the RM3000 magnetometer readouts.

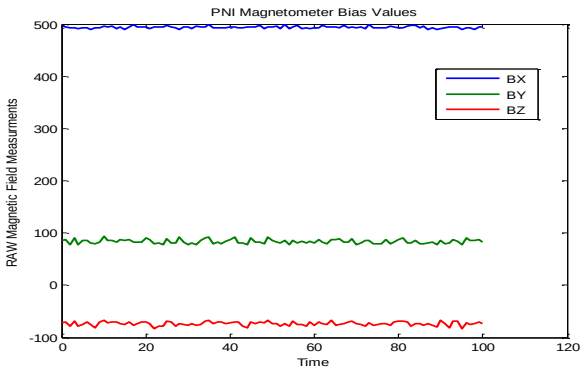

Figure A-7-1: RM3000 bias values

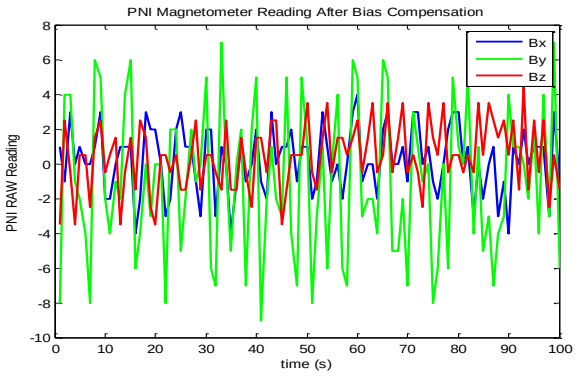

Figure A-7-2: After bias compensation

3. Set the magnetic field inside Helmholtz cage $[Bx\ By\ Bz] = [40\ 0\ 0]$ µT and adjust the RM3000 magnetometer over the fluxgate magnetometer such that the Y- and the Z-axis read out are less than 100 counts. Hereafter, divide the RM3000 X-axis read out with 40 to get the scale factor along the X-axis.
4. Set the magnetic field inside Helmholtz cage $[Bx\ By\ Bz] = [0\ 40\ 0]$ µT and adjust the RM3000 magnetometer over the fluxgate magnetometer such that the X- and the Z-axis read out are less than 100 counts. Hereafter, divide the RM3000 Y-axis read-out with 40 to get the scale factor along the Y-axis.
5. Set the magnetic field inside Helmholtz cage $[Bx\ By\ Bz] = [0\ 0\ 40]$ µT and adjust the RM3000 magnetometer over the fluxgate magnetometer such that the X- and the

Stellenbosch University https://scholar.sun.ac.za

Y-axis read out are less than 100 counts. Hereafter, divide the RM3000 Z-axis read out with 40 to get the scale factor along the Z-axis.

The Calibration model obtained through scheme-I is given as follows

$$Calibrated\ Magnetic\ Field_{\mu T} = \begin{bmatrix} 0.02 & 0 & 0 \\ 0 & 0.02 & 0 \\ 0 & 0 & 0.0185 \end{bmatrix} + \begin{bmatrix} -9.8675 \\ -1.6769 \\ 1.3642 \end{bmatrix}$$

ii- Scheme-2

The RM3000 magnetometer was placed on the top of the fluxgate Magnetometer in the uniform magnetic field environment of the Helmholtz Cage such that the axes of both magnetometers are aligned to each other. The magnetic field inside the Helmholtz cage was varied following an IGRF magnetic field model for the LEO satellite orbit. The data readout from the fluxgate magnetometer in micro-Tesla and the raw data from the RM3000 magnetometer, in the form of integer counts, were saved to a data file. Subsequently, the Recursive Least Square (RLS) algorithm described by Steyn [55] was applied on the experimental data to estimate the complete sensitivity matrix and the offset vector.

The calibration model used for the RLS algorithm is described by Equation (A.17)

$$\mathbf{B}_{cal} = \mathbf{S}\,\mathbf{B}_{meas}(t) + \mathbf{O} = \mathbf{A}(t)\mathbf{B}_{model} \tag{A.17}$$

where,

$\mathbf{A}(t) =$ Dirction Cosine Matrix(DCM)

$\mathbf{O} =$ offset vector

$\mathbf{B}_{model} =$ Fluxgate magnetometer output

$\mathbf{B}_{meas} =$ RM3000 magntometer raw output

The DCM in that case was an identity matrix of size 3x3. The RLS algorithm was executed to minimize the error between the modelled and the measured vector.

$$\mathbf{e}(k) = \mathbf{y}_{model}(k) - \mathbf{y}_{calib}(k) \tag{A.18}$$

$$= \mathbf{B}_{Fluxgate} - [\mathbf{S}(k)\mathbf{B}_{RM3000} + \mathbf{O}(k)]$$

Stellenbosch University https://scholar.sun.ac.za

with,

$$\mathbf{B}_{Fluxgate} = \text{Reference magnetic field value in micro} - \text{Tesla}$$

$$\mathbf{B}_{RM3000} = \text{uncalibrated RM3000 readouts}$$

The sensitivity matrix is a square matrix of size 3×3 that contains scale factors in its diagonal elements and the off-diagonal elements are the non-orthogonality factors.

$$\mathbf{S}(k) = \begin{bmatrix} S_{11}(k) & S_{12}(k) & S_{13}(k) \\ S_{21}(k) & S_{22}(k) & S_{23}(k) \\ S_{31}(k) & S_{32}(k) & S_{33}(k) \end{bmatrix}$$

and,

$$\mathbf{O}(k) = [O_x(k) \;\; O_y(k) \;\; O_z(k)]$$

The estimation of the gain and the offset parameters for each axis were written as a standard least square problem,

$$e_i(k) = y_i(k) - \boldsymbol{\varphi}^T(k)\boldsymbol{\theta}_i(k) \qquad i = 1,2,3 \tag{A.19}$$

$$\mathrm{y}_1(\mathrm{k}) = B_{xFluxgate}$$
$$\mathrm{y}_2(\mathrm{k}) = B_{yFluxgate}$$
$$\mathrm{y}_3(\mathrm{k}) = B_{zFluxgate}$$

The regression vector in that case was defined as,

$$\boldsymbol{\varphi}^T(k) = [Bx_{RM3000}(k) \;\; By_{RM3000}(k) \;\; Bz_{RM3000}(k) \;\; 1] \tag{A.20}$$

The parameter vectors that had to be estimated are,

$$\begin{aligned} \boldsymbol{\theta}_1^T(k) &= [S_{11}(k) \;\; S_{12}(k) \;\; S_{13}(k) \;\; O_x(k)] \\ \boldsymbol{\theta}_2^T(k) &= [S_{21}(k) \;\; S_{22}(k) \;\; S_{23}(k) \;\; O_y(k)] \\ \boldsymbol{\theta}_3^T(k) &= [S_{31}(k) \;\; S_{32}(k) \;\; S_{33}(k) \;\; O_z(k)] \end{aligned} \tag{A.21}$$

Stellenbosch University https://scholar.sun.ac.za

The RLS Algorithm

The RLS Algorithm was implemented as a Matlab script by following the steps mentioned as below:

1. The Regression vector $\boldsymbol{\varphi}^T(k)$ and the residual *e(k)* were calculated from the fluxgate and the RM3000 magnetometer data by using Equation (A.20) and (A.19). Taking a forgetting factor λ of 1, the update gain **K** was evaluated using following relation,

$$\mathbf{K}(k) = \mathbf{P}(k-1)\boldsymbol{\varphi}(k)[\lambda + \boldsymbol{\varphi}^T(k)\mathbf{P}(k-1)\boldsymbol{\varphi}(k)]^{-1} \quad \text{(A.22)}$$

   where, P is the covariance matrix of the regression vector

2. The parameter vector was updated using the updated value of gain

$$\boldsymbol{\theta}(k) = \boldsymbol{\theta}(k-1) + \mathbf{K}(k)e(k) \quad \text{(A.23)}$$

3. The covariance matrix was updated as follows,

$$\mathbf{P}(k) = [\mathbf{I}_{4\times4} - \mathbf{K}(k)\boldsymbol{\varphi}^T(k)]\mathbf{P}(k-1)/\lambda \quad \text{(A.24)}$$

4. Steps 1-4 were repeated every second in a loop [55]

The covariance matrix was initialized with $\mathbf{P}(0) = diag[10\ 10\ 10\ 10]$. The modelled and the calibrated magnetic field are depicted in the plots of Figure 6-13. The calibration model from scheme-II is given as follows

$$Calibrated\ Magnetic\ Field_{\mu T} = \begin{bmatrix} 0.0199 & 0.0001 & -0.0002 \\ -0.0005 & 0.0200 & 0.0001 \\ 0.0006 & 0.0010 & 0.0182 \end{bmatrix} \begin{bmatrix} Bx_{RM} \\ By_{RM} \\ Bz_{RM} \end{bmatrix} + \begin{bmatrix} -9.6918 \\ -1.3871 \\ 0.9583 \end{bmatrix}$$

Stellenbosch University https://scholar.sun.ac.za

Appendix C. DATASHEETS

i- Magnetometer

Stellenbosch University https://scholar.sun.ac.za

Reference Magnetic Sensor Suites

RM3000 & RM2000

THE HIGHEST ACCURACY SENSORS in their class, PNI's patented Reference Magnetic Sensor Suites deliver high performance resolution and repeatability with extremely low noise. The Reference Magnetic Sensor Suites have a wide field measurement range, superior noise immunity, no hysteresis, and are extremely stable over temperature. All this comes with the lowest power consumption in the industry.

Unlike magneto-resistive sensors, PNI's Reference Magnetic Sensor Suites do not require temperature calibration nor high current set and reset pauses before each measurement. Hence, they are simple to design in, and peak current requirement is dramatically less. It isn't surprising that this patented technology has been proven across a wide spectrum of applications, including motion tracking, compassing, robotics and targeting.

PNI
SENSOR CORPORATION

Stellenbosch University https://scholar.sun.ac.za

Reference Magnetic Sensor Suites

are designed to enable 3D (RM3000) and 2D (RM2000) applications and are optimized for use in game controllers, solid-state navigation devices, and handheld devices with integrated compassing functions. The Suites consist of 2 or 3 Reference Magnetic sensors driven by PNI's 3D MagIC ASIC. The interface to the 3D MagIC ASIC is through an SPI bus; eliminating the need for signal conditioning or an analog/digital converter.

Sen-XY (horizontal mount)
Sen-Z (vertical mount)

An all-digital demo board is available for design and prototyping for high-volume applications, as well as use in research, education and hobby use. The RM3000 demo board integrates PNI's Reference Magnetic Sensors and 3D MagIC ASIC onto a single PCB.

LOW POWER

HIGH RESOLUTION

Available suites:

RM3000 enables unparalleled performance in 3D applications. It contains two Sen-XY sensors, one Sen-Z sensor plus the new 3D MagIC ASIC controller.

RM2000 enables 2D applications and contains two Sen-XY sensors plus the new 3D MagIC ASIC controller.

RM3000 demo board incorporates the 3-axis sensor suite with PNI's 3DMagIC ASIC controller on a single PCB, and is ideal for prototyping applications such as video game controllers and TV remote controller devices that require high refresh rates and high magnetic sensor resolution. The SPI interface allows direct interface to a microprocessor, eliminating the need for additional signal processing. For 2D applications the third axis can simply be turned off.

Sensor Suite Specifications

Parameter		Min.	Typical	Max.
Field Measurement Range		-11 Gauss		+11 Gauss
Noise at 200 cycle counts			35 nT	
Gain at 200 cycle counts			45 counts µT	
Linearity over ±200 µT			0.6%	
Single Axis Data Rate at 200 cycle counts			450 Hz	
DC Supply Voltage		1.6 V	3.3 V	3.6V
Average Current (35 Hz single axis at 200 cycle counts)			0.3 mA	
Temperature Range	Operation	−40°C		85°C
	Storage	−40°C		85°C
Size	Sen-XY (l x w x h)		6.0 x 2.1 x 2.2 mm	
	Sen-Z (l x w x h)		3.0 x 3.0 x 5.75 mm	
	3DMagIC (l x w x h)		5.0 x 5.0 x 0.9 mm	

PNI SENSOR CORPORATION is America's leader in the exacting science of turning information from the Earth's magnetic field into usable orientation data. Building on decades of patented knowledge of magnetic fields and their anomalies, PNI offers today's most reliable magnetic sensors, including both 2 and 3 axis compasses and other advanced sensor systems. Highly sensitive and finely tuned, PNI offers a range of sensors to meet varying price, accuracy and footprint size needs.

Serving a demanding, wide-ranging list of industries and applications, PNI's U.S. based team of physicists, engineers, researchers and quality control experts can help speed your time to market and ensure marketplace success. Nimble and responsive, PNI offers a multitude of sensors to meet today's growing technology needs.

For detailed ordering information and most current specifications, please visit www.pnicorp.com

PNI Sensor Corporation 133 Aviation Blvd, Suite 101, Santa Rosa, CA 95403-1084 USA
Phone: 707-566-2260 Fax: 707-566-2261

08/11

PNI SENSOR CORPORATION

Stellenbosch University https://scholar.sun.ac.za

ii- CubeSense

Stellenbosch University https://scholar.sun.ac.za

ESL

Electronic Systems Laboratory

CubeSense

Fine Sun and Nadir Sensor

Description

The CubeSense system is an integrated sun and nadir sensor for attitude sensing. It makes use of two CMOS cameras – one dedicated to sun sensing and another for horizon detection. The sun sensor has a neutral density filter included in the optics. Both cameras have wide field-of-view optics. The primary outputs of the sensor are two angles that can be used to calculate the sun and nadir vectors relative to the CubeSense boresight.

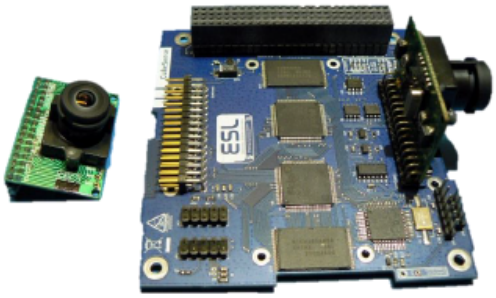

Feature List

Cameras:

- 640 x 480 pixel CMOS camera
- 190 deg FOV fisheye lens
- Nadir & Sun sensor modules
- Configurable placement options for each camera (side view or top view)

Onboard:

- Processing of nadir & sun centroids done onboard.
- Dual FPGA/SRAM system for redundancy
- Measurement updates @ 2 Hz both heads
- I2C and UART interface available

Accuracy (3σ):

- Nadir: < 0.3° with full earth in FOV
- Sun: < 0.3° over ±40° FOV
  < 0.5° over ±60° FOV
  < 1.0° over ±90° FOV

Application

- PC/104 form factor, compatible with CubeSat standard

Testing & Heritage

- Successful vibration & heated vacuum tests
- Radiation test (TID)
- Used on the QB50 precursor satellites.

Specifications

Operating Voltage	5 V
Power Consumption	360mW max, <100 mW avg
I2C Bus Voltage	3.3 V / 5 V
Operating Temperature	-10 °C – 70 °C
Mass	87 g (including cameras)
Dimensions*	90 x 96 x 10 mm (PCB) 28 x 41 x 31 mm (camera module)

***Depends on configuration options**

Electronics Systems Laboratory
Engineering Faculty
University of Stellenbosch
Private Bag X1 Matieland 7602
South Africa

Contact Us:
Phone: +27-21-808-4926
Fax: +27-21-808-4981
Email: whsteyn@sun.ac.za
URL: http://www.esl.sun.ac.za

UNIVERSITEIT STELLENBOSCH UNIVERSITY

Stellenbosch University https://scholar.sun.ac.za

iii- CubeStar

Stellenbosch University https://scholar.sun.ac.za

ESL

Electronic Systems Laboratory

CubeStar

Nano Star Tracker

Description

CubeStar is a CubeSat compatible nano star tracker. CubeStar can operate in full autonomous mode, outputting attitude estimates in inertial quaternions at a rate of 1Hz.

CubeStar builds largely on the proven hardware designs of CubeSense and CubeComputer.

Features

- Output attitude quaternions or raw images.
- Onboard current monitors and power switches safeguard against radiation induced latchups.

Specifications (without Baffle)

Weight (g)	56g
Dimensions (mm)	50.1 x 35.2 x 64
Power (mW)	320 nominal 500 peak
Operating Voltage (V)	3.3
Data Interface	I^2C / UART
Field of View (deg)	52 x 27
Star Catalogue Size	415

Performance

Sensitivity Range (Star Mag)	< 4.0
Number of Stars Tracked	15
Accuracy (deg, 1σ)	0.01 (cross bore) 0.03 (roll)
Update Rate (Hz)	1
Max Tracking Rate (deg/s)	0.3
Max Acquisition Time (ms)	1000

- CubeStar has been tested in a lab environment and under the night sky.
- Vacuum, thermal and vibration testing to be completed.

Electronics Systems Laboratory
Engineering Faculty
University of Stellenbosch
Private Bag X1 Matieland 7602
South Africa

Contact Us:
Phone: +27-21-808-4926
Fax: +27-21-808-4981
Email: whsteyn@sun.ac.za
URL: http//www.esl.sun.ac.za

UNIVERSITEIT STELLENBOSCH UNIVERSITY

Stellenbosch University https://scholar.sun.ac.za

iv- CubeComputer

Stellenbosch University https://scholar.sun.ac.za

ESL

Electronic Systems Laboratory

CubeComputer

General Purpose Onboard Computer

Feature List

Microcontroller :

- High performance, low power 32-bit ARM Cortex-M3 based MCU
- 4-48MHz @ 1.25 DMIPS/MHz
- Internal & external watchdog for added reliability

Memory & Storage :

- 256 KB of EEPROM
- 4 MB of Flash for Code Storage
- 2 x 1 MB of external SRAM for Data Storage
  - SEU protection by means of an FPGA based flow-through EDAC
  - SEL protection by detecting and isolating latchup currents
- MicroSD socket for storage up to 2GB

Communication :

- 2 x I2C interface with multi-master capabilities
- 1 x Debug UART interface on external header
- 1 x CAN interface up to 1Mbps

PiggyBack Header :

- Design a mission specific piggyback board which can be interfaced directly with CubeComputer.
- Includes pin outs for: 3.3V, 5V, Battery Supply, 4 x PWM, 4 x ADC, UART, SPI, I2C and more.

Software :

- Full compilation of drivers for OBC
- Robust bootloader with the ability to store and load multiple programs in-flight
- Compatible with variety of commercial Real-Time Operating Systems

Application

- Onboard Computer suitable for nano-satellite C&DH, TT&C, mass storage and ADCS
- PC/104 form factor, compatible with CubeSat standard

Testing & Heritage

- Successful vibration & heated vacuum tests
- Radiation tests (TID @ 20 krad, & SEE @ 60 MeV)
- ADCS OBC on QB50 precursor satellites

Specifications

Operating Voltage	3.3 V
Power Consumption	< 200 mW
I2C Bus Voltage	3.3 V / 5 V
Operating Temperature	-10 °C – 70 °C
Mass*	50 g – 70 g
Dimensions*	90 x 96 x 10 mm

***Depends on configuration options**

Electronics Systems Laboratory
Engineering Faculty
University of Stellenbosch
Private Bag X1 Matieland 7602
South Africa

Contact Us:
Phone: +27-21-808-4926
Fax: +27-21-808-4981
Email: whsteyn@sun.ac.za
URL: http://www.esl.sun.ac.za

UNIVERSITEIT STELLENBOSCH UNIVERSITY

Stellenbosch University https://scholar.sun.ac.za

v- Microcontroller

Stellenbosch University https://scholar.sun.ac.za

Features

- High Performance, Low Power AVR® 8-Bit Microcontroller
- Advanced RISC Architecture
  - 131 Powerful Instructions – Most Single Clock Cycle Execution
  - 32 x 8 General Purpose Working Registers
  - Fully Static Operation
  - Up to 20 MIPS Throughput at 20 MHz
  - On-chip 2-cycle Multiplier
- High Endurance Non-volatile Memory Segments
  - 4/8/16/32K Bytes of In-System Self-Programmable Flash progam memory (ATmega48PA/88PA/168PA/328P)
  - 256/512/512/1K Bytes EEPROM (ATmega48PA/88PA/168PA/328P)
  - 512/1K/1K/2K Bytes Internal SRAM (ATmega48PA/88PA/168PA/328P)
  - Write/Erase Cycles: 10,000 Flash/100,000 EEPROM
  - Data retention: 20 years at 85°C/100 years at 25°C(1)
  - Optional Boot Code Section with Independent Lock Bits
    - In-System Programming by On-chip Boot Program
    - True Read-While-Write Operation
  - Programming Lock for Software Security
- Peripheral Features
  - Two 8-bit Timer/Counters with Separate Prescaler and Compare Mode
  - One 16-bit Timer/Counter with Separate Prescaler, Compare Mode, and Capture Mode
  - Real Time Counter with Separate Oscillator
  - Six PWM Channels
  - 8-channel 10-bit ADC in TQFP and QFN/MLF package
    - Temperature Measurement
  - 6-channel 10-bit ADC in PDIP Package
    - Temperature Measurement
  - Programmable Serial USART
  - Master/Slave SPI Serial Interface
  - Byte-oriented 2-wire Serial Interface (Philips I^2C compatible)
  - Programmable Watchdog Timer with Separate On-chip Oscillator
  - On-chip Analog Comparator
  - Interrupt and Wake-up on Pin Change
- Special Microcontroller Features
  - Power-on Reset and Programmable Brown-out Detection
  - Internal Calibrated Oscillator
  - External and Internal Interrupt Sources
  - Six Sleep Modes: Idle, ADC Noise Reduction, Power-save, Power-down, Standby, and Extended Standby
- I/O and Packages
  - 23 Programmable I/O Lines
  - 28-pin PDIP, 32-lead TQFP, 28-pad QFN/MLF and 32-pad QFN/MLF
- Operating Voltage:
  - 1.8 - 5.5V for ATmega48PA/88PA/168PA/328P
- Temperature Range:
  - -40°C to 85°C
- Speed Grade:
  - 0 - 20 MHz @ 1.8 - 5.5V
- Low Power Consumption at 1 MHz, 1.8V, 25°C for ATmega48PA/88PA/168PA/328P:
  - Active Mode: 0.2 mA
  - Power-down Mode: 0.1 µA
  - Power-save Mode: 0.75 µA (Including 32 kHz RTC)

8-bit AVR® Microcontroller with 4/8/16/32K Bytes In-System Programmable Flash

ATmega48PA
ATmega88PA
ATmega168PA
ATmega328P

Rev. 8161D–AVR–10/09

Stellenbosch University https://scholar.sun.ac.za

vi- BLDC Motor Driver

Stellenbosch University https://scholar.sun.ac.za

Ordering number : ENA2058

LV8827LFQA

Bi-CMOS IC

For Brushless Motor Drive
PWM Driver IC

ON Semiconductor®

http://onsemi.com

Overview

The LV8827LFQA is a PWM-type driver IC designed for 3-phase brushless motors. The rotational speed can be controlled by inputting the PWM pulse from the outside, and changing Duty. The IC incorporates a latch-type constraint protection circuit.

Features

- I_O max = 1.5A (built-in output Tr)
- Speed control and synchronous rectification using direct PWM input (supports 3.3V inputs)
- 1-Hall FG output
- Latch type constraint protection circuit (the latch is released by S/S and F/R.)
- Forward/reverse switching circuit, Hall bias pin
- Power save circuit (Power save in stop mode)
- Current limiter circuit, Low-voltage protection circuit, Overheat protection circuit
- Charge pump circuit, 5V regulator output.
- Start/stop circuit (short brake when motor is to be stopped)

Specifications

Absolute Maximum Ratings at Ta = 25°C

Parameter	Symbol	Conditions	Ratings	Unit
Supply voltage	V_{CC} max	V_{CC} pin	36	V
	V_G max	V_G pin	42	V
Output current	I_O max	t ≤ 500ms *1	1.5	A
Allowable power dissipation	Pd max2	Mounted on a circuit board.*2	1.35	W
Junction temperature	Tj max		150	°C
Operating temperature	Topr		-40 to +80	°C
Storage temperature	Tstg		-55 to +150	°C

*1 : Tj cannot exceed Tj max = 150°C
*2 : Specified circuit board : 40mm × 50mm × 0.8mm, glass epoxy (four-layer board)
Caution 1) Absolute maximum ratings represent the value which cannot be exceeded for any length of time.
Caution 2) Even when the device is used within the range of absolute maximum ratings, as a result of continuous usage under high temperature, high current, high voltage, or drastic temperature change, the reliability of the IC may be degraded. Please contact us for the further details.

Stresses exceeding Maximum Ratings may damage the device. Maximum Ratings are stress ratings only. Functional operation above the Recommended Operating Conditions is not implied. Extended exposure to stresses above the Recommended Operating Conditions may affect device reliability.

Semiconductor Components Industries, LLC, 2013
May, 2013

53012 SY 20120507-S00003 No.A2058-1/13

Stellenbosch University https://scholar.sun.ac.za

vii- H-bridge Driver for Magnetorquers

Stellenbosch University https://scholar.sun.ac.za

Ordering number : ENA1250A

LV8411GR

Bi-CMOS LSI

For DSC, and Cell Phone Camera Modules
4-channel Single-chip Motor Driver IC

ON Semiconductor®

http://onsemi.com

Overview

The LV8411GR is an H bridge motor driver IC and is able to control 4 modes of forward, reverse, brake, and standby. This IC housed in a miniature package is optimum for use in a stepping motor driving system for DSC or a camera module of cell phones.

Features

- Saturation drive H bridge: 4 channels
- Built-in thermal protection circuit
- Built-in low voltage malfunction prevention circuit
- Incorporates a transistor for driving photosensors

Specifications

Absolute Maximum Ratings at Ta = 25°C

Parameter	Symbol	Conditions	Ratings	Unit
Power supply voltage 1	V_M max		6.0	V
Power supply voltage 2	V_{CC} max		6.0	V
Output peak current	I_O peak	Channels 1 to 4, t ≤ 10msec, ON-duty ≤ 20%	600	mA
Output continuous current 1	I_O max1	Channels 1 to 4	400	mA
Output continuous current 2	I_O max2	PI1	30	mA
Allowable power dissipation	Pd max	Mounted on a circuit board*	1.05	W
Operating temperature	Topr		-40 to +85	°C
Storage temperature	Tstg		-55 to +150	°C

* Specified circuit board : 40mm×50mm×0.8mm : glass epoxy four-layer board

Caution 1) Absolute maximum ratings represent the value which cannot be exceeded for any length of time.

Caution 2) Even when the device is used within the range of absolute maximum ratings, as a result of continuous usage under high temperature, high current, high voltage, or drastic temperature change, the reliability of the IC may be degraded. Please contact us for the further details.

Stresses exceeding Maximum Ratings may damage the device. Maximum Ratings are stress ratings only. Functional operation above the Recommended Operating Conditions is not implied. Extended exposure to stresses above the Recommended Operating Conditions may affect device reliability.

Semiconductor Components Industries, LLC, 2013
June, 2013

62012 SY 20120604-S00001/70908 MS PC 20080703-S00001 No.A1250-1/7